Development of cost-effective Alternatives to Conventionally-Manufactured Metal Foam for Industrial Turbine Combustors

par

Julien SIROIS

MÉMOIRE PAR ARTICLES PRÉSENTÉ À L'ÉCOLE DE TECHNOLOGIE
SUPÉRIEURE COMME EXIGENCE PARTIELLEÀ L'OBTENTION DE LA
MAÎTRISE AVEC MÉMOIRE EN GÉNIE MÉCANIQUE
M. Sc. A

MONTRÉAL, LE 12 AVRIL 2024

ÉCOLE DE TECHNOLOGIE SUPÉRIEURE
UNIVERSITÉ DU QUÉBEC

PRÉSENTATION DU JURY

CE MÉMOIRE A ÉTÉ ÉVALUÉ

PAR UN JURY COMPOSÉ DE :

M. Brailovski, directeur de mémoire
Département de génie mécanique à l'École de technologie supérieure

Mme. Sanjosé, codirectrice de mémoire
Département de génie aérospatial à l'École de technologie supérieure

M. Sébastien Lalonde, président du jury
Département de génie mécanique à l'École de technologie supérieure

M. Patrick Germain, membre du jury
Département de génie aérospatial à l'École de technologie supérieure

M. Marc Füri, membre du jury
Siemens Energy Canada

M. François Morency, membre suppléant du jury
Département de génie aérospatial à l'École de technologie supérieure

IL A FAIT L'OBJET D'UNE SOUTENANCE DEVANT JURY ET PUBLIC

LE 4 AVRIL 2024

À L'ÉCOLE DE TECHNOLOGIE SUPÉRIEURE

REMERCIEMENTS

Le travail accompli au cours des dernières années a été rendu possible grâce à l'apport de nombreuses personnes.

D'abord, j'aimerais remercier mon directeur de mémoire, Prof. Vladimir Brailovski ainsi que ma co-directrice, Prof. Marlène Sanjosé pour leur appui, leurs précieux conseils, et surtout, pour m'avoir aidé à trouver un équilibre entre ma curiosité et l'obtention des résultats importants. J'aimerais aussi remercier les employés de soutien de l'ÉTS, dont Michel Drouin pour sa précieuse aide avec l'instrumentation et l'asservissement du banc d'essai. Je remercie également mes collègues du LAMSI avec qui j'ai pu échanger fous rires et discussions plus sérieuses.

Je tiens également à souligner la contribution de plusieurs collègues chez Siemens Energy, dont Pierre Gauthier, Sandeep Jella et Marc Füri, qui m'ont aidé à bien comprendre les tenants et aboutissants de la problématique ainsi que la dynamique des écoulements propre à une chambre de combustion. En outre, ce projet n'aurait été possible sans Fabian Sanchez et Gianni Panfili qui m'ont permis d'entreprendre ce projet en m'allouant du temps ainsi qu'en assurant le financement.

Finalement, je voue une gratitude infinie à mes parents qui m'ont transmis leur amour pour les études et qui m'ont inculqué la persévérance et la rigueur. Merci également à ma conjointe pour m'avoir épaulé durant ce long parcours.

Développement d’alternatives imprimées en 3D à la mousse métallique fabriquée de manière conventionnelle pour les chambres de combustion des turbines Industrielles

Julien SIROIS

RÉSUMÉ

Le travail présenté ici vise à fournir des lignes directrices pour la conception de structures d'amortissement des tourbillons. Un plan d'expérience a été mis au point pour étudier les effets individuels et combinés des propriétés géométriques des structures planes à grille régulière, c'est-à-dire le diamètre du fil, la porosité et l'espacement entre les grilles, sur leurs performances en matière d'amortissement des tourbillons. Les simulations ont été effectuées à l'aide d'un solveur RANS instable commercial. Le modèle s'appuie sur l’allée de Von Karman pour générer des tourbillons dans un tuyau qui sont convectés en aval, où ils interagissent avec un réseau de grilles. L'efficacité de la décomposition des tourbillons est caractérisée par la perte de charge, l'énergie cinétique turbulente résiduelle, l'homogénéité de l'écoulement et la taille des tourbillons transmis. Le diamètre du fil s'avère être un levier de conception important car il affecte le niveau de distorsion des tourbillons transmis. L'augmentation du nombre de grilles accroît la perte de pression, mais leur contribution à la rupture des tourbillons est par ailleurs limitée lorsque le diamètre du fil est faible. L'influence de l'espacement des grilles dépend fortement du diamètre du fil et de l'alignement des grilles. Par exemple, la minimisation de cet écart réduit la perte de charge pour les configurations en ligne, mais augmente la perte de charge pour les configurations décalées.

Le design optimal devrait être une structure graduelle, commençant par une grille très poreuse fabriquée à partir d'un fil de grand diamètre pour briser les tourbillons entrants. Les grilles supplémentaires devraient être décalées pour augmenter la tortuosité et maximiser l'homogénéité de l’écoulement. Le diamètre des grilles subséquentes devrait diminuer progressivement pour réduire l’énergie turbulente cinétique.

Mots-clés: Suppression des tourbillons, interaction avec des grilles, RANS, écoulement confiné, allée de Von Karman.

Development of 3D-printed alternatives to conventionally-manufactured metal foam for industrial turbine combustors

Julien SIROIS

ABSTRACT

The work presented here aims to provide design guidelines to create vortex-damping structures. A design of experiment was developed to investigate the individual and combined effects of the geometrical properties of planar regular grid structures, i.e., the wire diameter, the porosity, and the inter-grid spacing, on their vortex-breakdown performance. The simulations were carried out using a commercial unsteady RANS solver. The model relies on the Von Karman street effect to generate vortices in a pipe which are convected downstream, where they interact with an array of grids. The vortex-breakdown efficiency is characterized by the pressure drop, the residual turbulent kinetic energy, the flow homogeneity, and the size of the transmitted vortices. The wire diameter is shown to be an important design lever as it affects the level of distortion of the transmitted vortices. Increasing the number of grids augments the pressure loss, but their contribution to vortex breakdown is otherwise limited when the wire diameter is small. The influence of grid spacing strongly depends on the wire diameter and grid alignment. For instance, minimizing this gap reduces the pressure drop for the inline configurations, but increases the pressure drop for the offset configurations.

Ultimately, the optimal design should be a graded structure, starting with a very porous grid made from a large wire diameter to breakdown the incoming vortices. Additional grids should be rotated and offset to increase the tortuosity, as it improves the velocity homogeneity. The wire diameter of the subsequent grids should be progressively smaller to reduce the TKE. The spacing between the grids should be as large as possible and their numbers must be kept to a minimum to avoid excessive pressure losses. The porosity should only be reduced when the desired velocity uniformity cannot be obtained by other means.

Keywords: Vortex breakdown, grid interaction, RANS, confined flow, Von Karman Street

TABLE OF CONTENTS

LIST OF TABLES

Page

LIST OF FIGURES

Page

LIST OF ABBREVIATIONS AND ACRONYMS

CAD	Computer-aided design
CFD	Computational Fluid Dynamics
CT	Computerized Tomography
CVA	Constant-voltage anemometry
DLE	Dry-Low Emission
DoE	Design of Experiment
HWA	Hot-wire anemometer
KPI	Key performance indicator
MTV	Molecular Tagging Velocimetry
NOx	Nitrous Oxides
PIV	Particle image velocimetry
PLIF	Planar Laser Induced Fluorescence
RANS	Reynolds-Averaged Navier-Stokes
VIV	Vortex-induced vibration

LIST OF SYMBOLS AND UNITS OF MEASUREMENTS

TKE	Turbulent Kinetic Energy	J/kg
ΔP	Pressure drop	Pa
θ	Velocity Field Uniformity	%
TVS	Transmitted Vortex Size	mm
D	Diameter of the tunnel	mm
d	Diameter of the bluff body	mm
d_w	Diameter of the grid wires	mm
ε	Intergrid spacing (gap between two grids)	mm
φ	Grid porosity	%
ρ	Density	kg/m^3
μ	Dynamic Viscosity	Pa*s
K	Permeability	m^2
U	Velocity	m/s
F_D	Drag Force	N
$A_{Frontal}$	Frontal Area	m^2
Re_{BB}	Reynolds number based on bluff body diameter	-
Re_{Pipe}	Reynolds number based on tunnel diameter	-
St	Strouhal Number	-

INTRODUCTION

Industrial gas turbines are a key component in power generation. To maintain their competitiveness, operators strive to reduce their operating cost and manufacturers continuously work to improve efficiency of their engine. One avenue to improve efficiency is in the optimization of air management in the combustion system by reducing the pressure losses upstream of the combustors.

A particularity of Dry Low Emission (DLE) combustion systems is that the air and fuel are thoroughly mixed upstream of the combustion chamber. This ensures a very clean and uniform combustion, allowing these engines to achieve very low NOx levels without the use of water injection to lower the flame temperature. However, it is primordial for the highly turbulent flow field coming from the compressor stage to be conditioned before it can enter the combustion system. This is because large vortices, caused by the successive blade cascade wakes, can lead to the formation of lean air pockets which are detrimental to combustion uniformity and can result in excessive NOx levels and harmful combustion dynamics [1]. Stochastic structures like metal foams are highly effective at damping vorticity and homogenizing the flow, and have been used successfully for many years, as shown in Figure 0-1. However, metal foams incur a considerable pressure loss, impacting the overall efficiency of the engine.

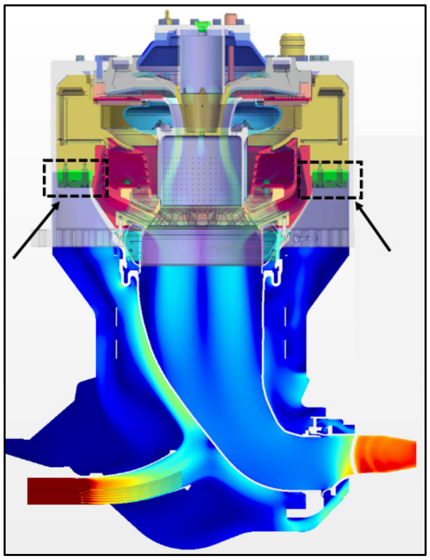

Figure 0-1 Cut section showing the position of the foam inside the combustor (black arrows)

Considering the capabilities of modern additive manufacturing techniques, the idea of developing a substitute lattice structure germinated, with a focus on reducing the pressure loss while retaining the homogenizing power.

To achieve this goal, the first step is to characterize the current foam which will serve as the baseline. Samples of the foam were CT-scanned to measure their geometrical properties and extract key flow properties. The permeability of the foam was also measured using a small-scale water tunnel.

A series of lattices structures were then iteratively created. Using the foam's dimensions as a starting point, seven different structures were generated and analyzed. The geometry of the lattices were then adjusted until the flow properties of the replacement structures matched those of the foam. This approach proved to be inefficient and impractical, as minute changes could sometimes have significant effects of the flow, and the trends varied from one lattice type to another.

This prompted the focus of the project to pivot toward a more fundamental understanding of how the basic lattice properties, i.e., the strut diameter, the porosity and the overall arrangement influenced the flow characteristics of the structures. To this end, a design of experiment was developed using simple grid stacks. These simplified geometries were tested numerically using CFD and experimentally using a custom small-scale wind tunnel. The principal objective of the project remains the same however: develop a model to guide decision-making for the design of a replacement structure.

This thesis is divided into five chapters. It begins with a review of the literature of the different permeability models for porous structures and the current state of the art on interaction between grids and vortical structures. The second chapter covers the foam characterization process and the development of alternative lattice structures. The third chapter describes the numerical method and the results of the study on vortex-grid interactions. The fourth chapter presents the custom wind tunnel rig, the instrumentation techniques employed and the experimental results. The final chapter discusses the numerical and experimental results, and tackles the reasons behind the discrepancies.

CHAPITRE 1

LITERATURE REVIEW

The following chapter begins with a brief overview of what constitutes a porous structure, their manufacturing processes, and the common models used to predict their pressure drop. The fundamental notions of turbulence and vorticity are then covered, along with the key performance indicators used in this study to measure the efficiency of the proposed solutions. The penultimate section discusses the current state of the art of vortex breakdown with grid structures and the techniques used by previous authors. This chapter concludes on the objectives of this thesis.

1.1 Porous Materials

As the name implies, porous materials are a class of material that contains a certain amount of porosity i.e. voids, within a solid matrix. These voids are referred to as cells. Porous materials come in many shapes and size, but fundamentally fall within four categories (see Figure 1-1), based on whether the cells are opened or closed, and whether the cells are arranged periodically (lattice structures, honeycombs) or randomly (foams, sponges, soil).

Opened-cell materials are characterized by having open pores which allow a fluid to pass through and are typically used in filtration and in heat-transfer applications. The pores can be interconnected e.g., a sponge, or independent e.g., the fins of a radiator.

With closed-cell materials, the pores are sealed, preventing the passage of a fluid. They are commonly used for their insulating properties (polyurethane foam in walls) and in energy-absorption applications.

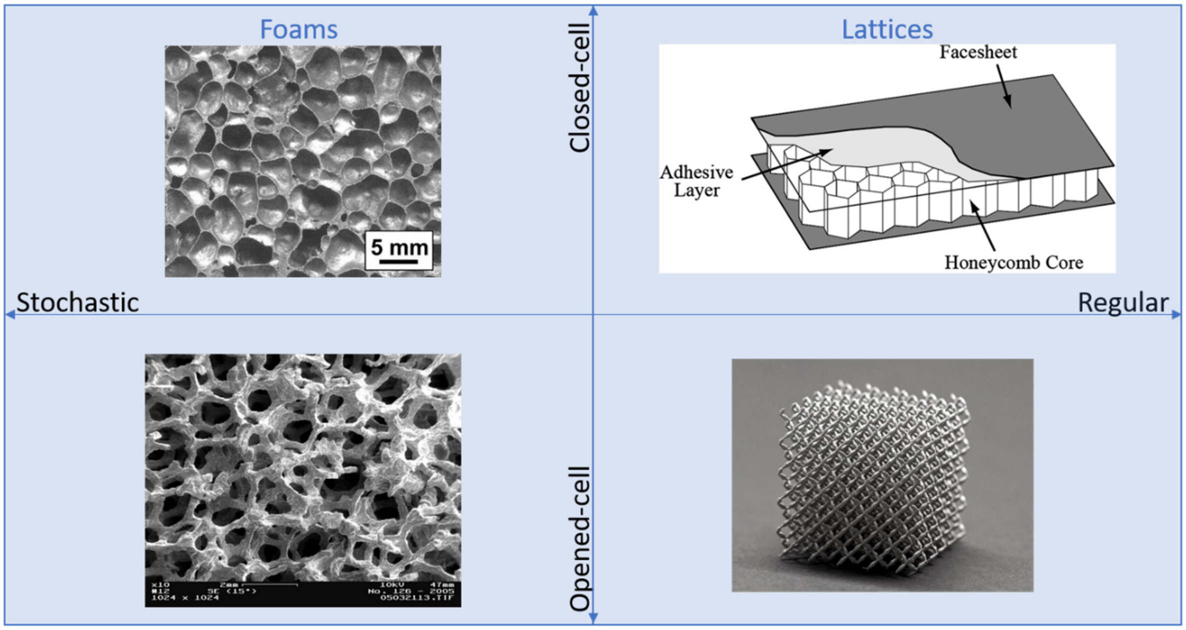

Figure 1-1 Different types of porous structures

In practice, the geometries most commonly encountered in the context of fluid dynamics are packed bed of granulates (soil seepage, filtration), porous rocks (shale extraction), tubes (heat exchanger) and foams (filtration).

The production of metallic foams first got traction in academia in the 1960s and 1970s, with most of the research focused on aluminium, magnesium, zinc, and their alloys [2]. Despite the quality of the materials produced, the industrial interest didn't materialize until the early 2000s. Since then, a plethora of techniques have emerged and with them, new alloys and better control of the properties, further expanding the scope of possibilities. Since covering all these would be fastidious, this section will solely cover the processes used to produce nickel-based foams, which is the material of choice for high-temperature applications.

Banhart's extensive review of the state-of-the-art techniques to produce metallic foams describes three processes to manufacture open-cell nickel foam: gasars, electro-deposition and vapour deposition. The foams currently in use are produced by Meggitt Aerospace under the commercial name Retimet. As described by Torrents *et al*. [3] the material is obtained by the electro-deposition technique where a sacrificial foamed polymer, first coated in a conductive layer, is electroplated in alternating layers of nickel and chrome. A subsequent heat treatment promotes the interdiffusion of the metals which combine to form the alloy. Under the heat, the polymer foam is burnt away, leaving a hollow structure with very thin walls.

More recently, Xiong *et al*. [4] replaced the foamed polymer by a microlattices structure obtained via self-propagating photopolymer waveguide prototyping, a process similar in function to stereolithography. The sacrificial template was then electroplated and removed by chemical etching. Though indirectly, this is one of the first examples of a nickel-based microlattices material obtained using additive manufacturing.

1.2 Pressure drop in a porous media.

When porous structures are introduced in a flow, they create a blockage preventing the fluid from moving freely, which results in a pressure loss. This pressure drop is typically measured between the inlet and outlet surfaces of the structure. In most design projects, knowing this pressure drop is an essential variable. Although the existing pressure-gradient models presented in the following sections are highly accurate, they require experimentally-fitted coefficients, making them structure-specific. These models are divided into three categories, based on the variables they rely on i.e., permeability, tortuosity, and geometrical parameters.

1.2.1 Permeability

Permeability describes how restrictive a medium is to the passage of a fluid. The more permeable a membrane is, the less restrictive it is.

With his pioneering work on water seepage in 1856, Darcy demonstrated that the pressure gradient caused by the viscous forces was a function of three variables: the fluid's dynamic viscosity, the fluid's velocity (V), and the medium's permeability (K) [5]. He gave us this first equation.

$$\nabla P = \frac{\mu}{K} \cdot V \tag{1-1}$$

The second variable is the fluid's dynamic viscosity μ, which describes its resistance to deformation for a given rate. A very viscous fluid such as honey requires a lot more force to squirt it from a bottle compared to water. The final variable is the velocity V of the fluid itself. Note that this equation only holds for near-stagnant flows (Reynolds ≤ 1) [5].

As the velocity of the fluid increases, a particle moving through a porous media can no longer follow the path of least resistance (natural seepage) and will eventually be blocked by the solid matrix. This impediment causes a change of momentum and was first described by Dupuit (1863) and Forchheimer (1901) and led to the addition of the inertial term to Darcy's equation [5]. β is known as the Forchheimer coefficient and is found experimentally.

$$\nabla P = \frac{\mu}{K_{fh}} \cdot V + \beta \rho V^2 \tag{1-2}$$

Many hypotheses have been proposed to explain why the speed is squared, but none are really accurate [5, 6].

A modification to the classic Forchheimer equation was proposed by Jospeh et al in 1982 [5]. This model introduced the dependence of the form drag, first discovered by Ward in 1964 [5]. This is the most widely used form of the Darcy-Forchheimer equation [5].

$$\nabla P = \frac{\mu}{K} \cdot V - C_f K^{-1/2} \rho |V| V \tag{1-3}$$

Where C_f is the form-friction coefficient (dimensionless) and ρ is the fluid's density.

In 1973, Beavers *et al.* [5] showed this coefficient was a function of the bonding walls and proposed this equation, where D_e is the equivalent bed diameter (*h* and *w* being the length and width) and *d* is the pore diameter.

$$C_f = 0.55\left(1 - 5.5\frac{d}{D_e}\right), \text{where } D_e = \frac{2wh}{w+h} \tag{1-4}$$

Many solutions have been brought forward to evaluate C_f analytically, but none appear to be universal. This can be explained by the fact the form drag coefficient depends primarily on the form of the medium. One can see how a formula idealizing a series of tube to model a heat exchanger may not be accurate to describe the pressure drop in a packed bed of sphere. It is worth noting however that a foam is essentially the negative image of a packed bed of spheres.

1.2.2 Tortuosity

When air enters the foam, it navigates a labyrinth laden with various obstacles preventing the molecules from moving directly to the exit in a straight line, which effectively extends the length of the travelled path. Tortuosity quantifies how sinuous the path of a particle is between two points and is defined as the ratio between the travelled length and the smallest distance between these points, as shown in Figure 1-2. As pointed out by Guo [7], tortuosity is a material-dependant variable and primarily depends on the pore geometry (size and shape) and the porosity. It is also intrinsically directional.

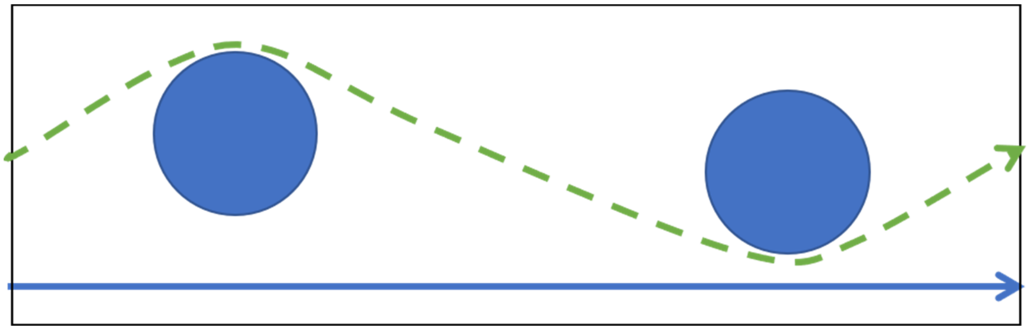

Figure 1-2 Schematic representation of tortuosity

Bazarin *et al.* [8] proposed a model where the permeability is function of the porosity (φ), tortuosity (T) and specific surface area (M). C_{KC} is the Carman-Kozeny constant.

$$K = C_{KC}\frac{\varphi^3}{T^2M^2} \tag{1-5}$$

Much effort was invested trying to establish a relation between said parameters and the resulting tortuosity, but most models rely on fitted coefficients. Prior to CT-scanning becoming a more ubiquitous analysis technique, tortuosity was a dependant variable most frequently introduced to account for discrepancies in the predicted permeability of a porous media vs. the experimental results [5]. In the context of designing new structures, those models are not very useful.

Similarly, some models were developed for geometries that are drastically different from what we are attempting to reproduce. Several investigators have demonstrated that the pore geometry greatly influences the tortuosity of the media [9].

Most of the academic interest regarding tortuosity comes from the field of geology, with a keen interest in understanding how tortuosity impacts the extraction of fossil fuels from shale formations.

1.2.3 Geometrical parameters

A key issue with the models based on permeability and tortuosity is that these properties are inherently dependent on the geometry of the structures and are difficult to measure without a CT-scan. With this in mind, some authors looked at developing models based on easily quantifiable properties.

In 1952, Ergun proposed a model based on the porosity (φ) of the structures [5]. The Ergun coefficients (ERG_A & ERG_B) must be fitted to experimental data but are often reported in the literature as $ERG_A=150$ and $ERG_B=1.75$.

$$\frac{\Delta P}{L} = \frac{ERG_A \cdot \mu(1-\varphi)^2 V}{\varphi^3 D_p^2} + \frac{ERG_B \cdot \rho(1-\varphi) V^2}{\varphi^3 D_p} \tag{1-6}$$

A more recent model was proposed by Azzi *et al.*[10] based on Ashby, and was developed specifically for foams:

$$\frac{\Delta P}{L} = \zeta \frac{1}{a}\left[\frac{v_a^m \rho_a}{(1-\alpha)^{2-m}}\right] V_f^{2-m} d^{-m}, \text{where } v_a^m = \frac{\mu}{\rho} \tag{1-7}$$

$$a = 1.24d\sqrt{\frac{3\pi}{\rho_{rel}}} \tag{1-8}$$

Where V_f is the free stream velocity, α is the fluid thermal diffusivity, υ_a is the kinetic viscosity, d is the ligament diameter (strut diameter), ρ_a is the fluid density. The coefficients ζ and m are determined experimentally.

1.3 Vortex Formation and Breakdown

Vortices are a complex subset of turbulence and appear under many different forms. The following section distills the physical phenomenon massively, focusing on the specific aspects which are crucial to the project's understanding.

At its core, a vortex is a body of fluid which revolves around an axis. They are coherent structures and can be transported by a fluid. In the absence of an external force, a vortex will generally be irrotational, which essentially means that the angular momentum is constant. This implies that the particle's velocity magnitude u is inversely proportional to the distance r from the axis. In other words, the closer a particle is to the axis, the faster it will move. However, the velocity of that particle cannot be infinite, and it eventually reaches zero at the axis. This very thin region is known as the vortex core. Within its core, the vortex is no longer irrotational and the difference in velocity results in a viscous stress, leading to dissipation of the turbulent kinetic energy. This phenomenon happens on a very small scale known as the Kolmogorov scale. If left alone, this vortex core will expand until all the energy is dissipated.

When a vortex intersects an object, it is forced to divide into substructures. Therefore, since the vortices are smaller after the obstacle, their energy will dissipate into heat faster due to Kolmogorov's energy cascade.

Vortex breakdown is equally complex. In their review of the state of the art, Lucca-Negro & O'Doherty [11] noted there are seven different types of vortex breakdown. Of interest to us is bubble breakdown (type 0), which is the dominant breakdown mode for the vortices being investigated.

1.3.1 Von Kármán Street Effect

For the entrance conditions, we need to generate a turbulent flow with vortices. This is achieved by introducing a bluff body upstream of the porous region. The flow over a bluff body has been extensively studied because it is a very common phenomenon with sometime dramatic consequences.

Under certain conditions, the passage of a fluid over a bluff body will cause vortices to form downstream of a blunt object. This phenomenon, known as vortex shedding, will see these vortices periodically detach from either side of the body, creating a Von Karman vortex street. Figure 1-3 shows a Von Karman alley simulated in CFD. The alternating low-pressure vortices vibrate the body as it experiences a cyclical lift variation.

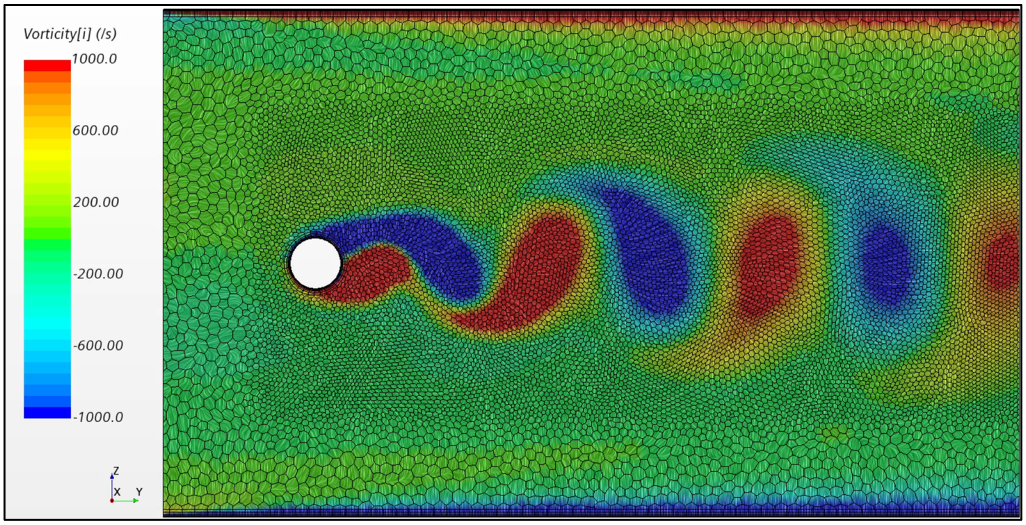

Figure 1-3 Von Karman street alley in CFD

As the vortex shedding sequence commences, it creates vortex-induced vibration (VIV) which have cause structures to fail, such as tall chimney and pipelines laying at the bottom of the sea floor. Generally speaking, this behavior is detrimental and as such, most of the research concentrates on eliminating the vortex-shedding at the source. Some of the work concentrates on understanding the phenomenon fundamentally, while others have been busy developing solutions, both passive and active, to mitigate the VIV [12]. In some cases, VIV are intentionally seeded, mostly for flow measurements.

More recently, this principle was applied to flow instrumentation, where a rod is placed inside a pipe. As the fluid passes, the vibration is monitored and converted to a flow velocity. The relationship between the velocity, bluff body diameter and shedding frequency is expressed by the Strouhal number. For a cylindrical body in the range 50 <Re<5000, the Strouhal number (*St*) is approximately 0.20 +/- 0.02 [13].

$$St = \frac{fD_{BB}}{U} \tag{1-9}$$

$$Re = \frac{\rho U D_{BB}}{\mu} \tag{1-10}$$

Where f is the frequency, D_{BB} is the bluff body diameter, U is the velocity, ρ is the density and μ is the dynamic viscosity.

1.3.2 Vortex interaction with porous grids

Vortex interaction has been investigated by a few authors. The following section focuses on the experimental and numerical methods employed by them. The review of their results is presented in section 3.4.

Hrynuk *et al.*[14, 15] focused on the visualization of a vortex ring impacting a single porous screen. The experiment was conducted with a simple gravity-driven apparatus. A screen was held in place inside a tank of stationary water above a vortex ring generator. Instead of a piston, the pulse was generated by a column of water. Varying the height of the column changed the flow velocity. Planar Laser Induced Fluorescence (PLIF) was used to visualize the flow with a mixture of fluorescein dye and water.

The experimental setup used by Naaktgeboren *et al.*[16] is slightly different to that used by Hrynuk, but also generates a vortex ring. A piston is used to create the pulse and the vortex travels horizontally towards the screen. PLIF was used to visualize the vortical structures impacting the fiberglass mesh, because the dark and opaque aspect of the fiberglass provides a contrasting background resulting in high-quality imaging of the flow. Particle Image Velocimetry (PIV) was preferred to visualize the vortical structures impacting the stainless-steel grids because it allows for a more precise measurement of the particle movements. The bright and shiny aspect of the stainless steel would not yield good results with PLIF.

The same experimental setup was used by Musta & Kruger [17, 18], who studied the effect of multiple meshes in series. The working fluid was a solution of water and glycerin, and PIV was selected for the visualization. The schematic of their experimental rig is shown in Figure 1-4

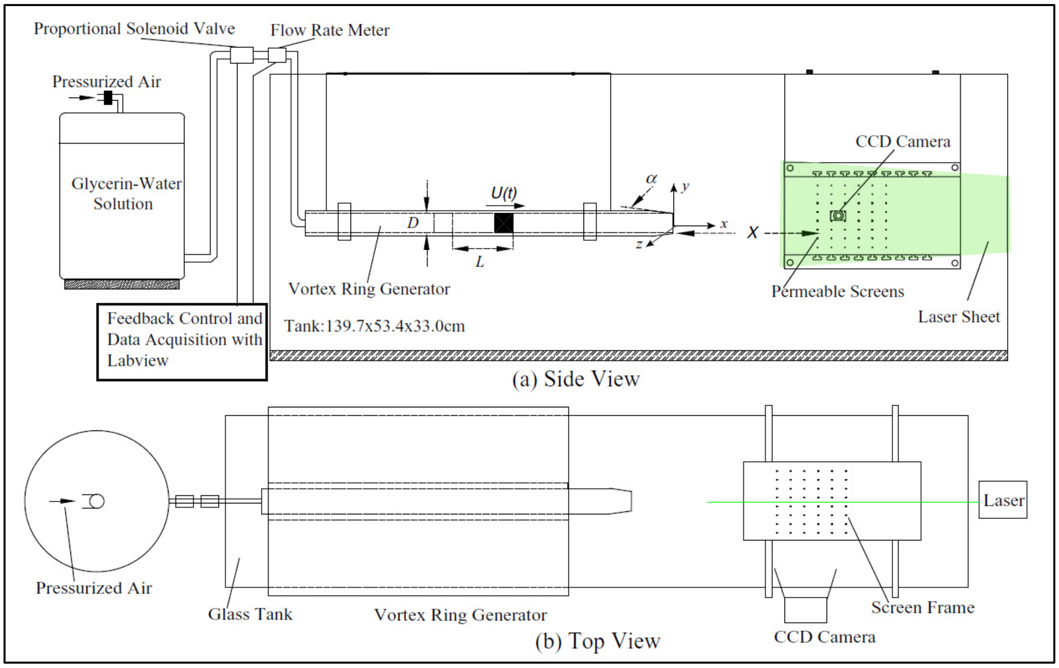

Figure 1-4 Schematic of an experimental vortex-ring generator, with the grids and imaging equipment., taken from [17], p. 3

Hrynuk et al. [14, 15] demonstrated the effect of the wire diameter to be considerable. As the size of the wire increases, the level of disturbance caused by the interaction also increases, as shown in Figure 1-5. Specifically, the reformation of the primary vortex becomes more diffuse due to the formation of secondary vortical sub-structures which disrupt the vortex core. In the case of the coarse mesh, these sub-structures were sufficiently strong to prevent the vortex from reforming past the screen. Of particular interest, it was observed that a coarser mesh caused less changes in the convection speed, but the authors did not measure the pressure drop.

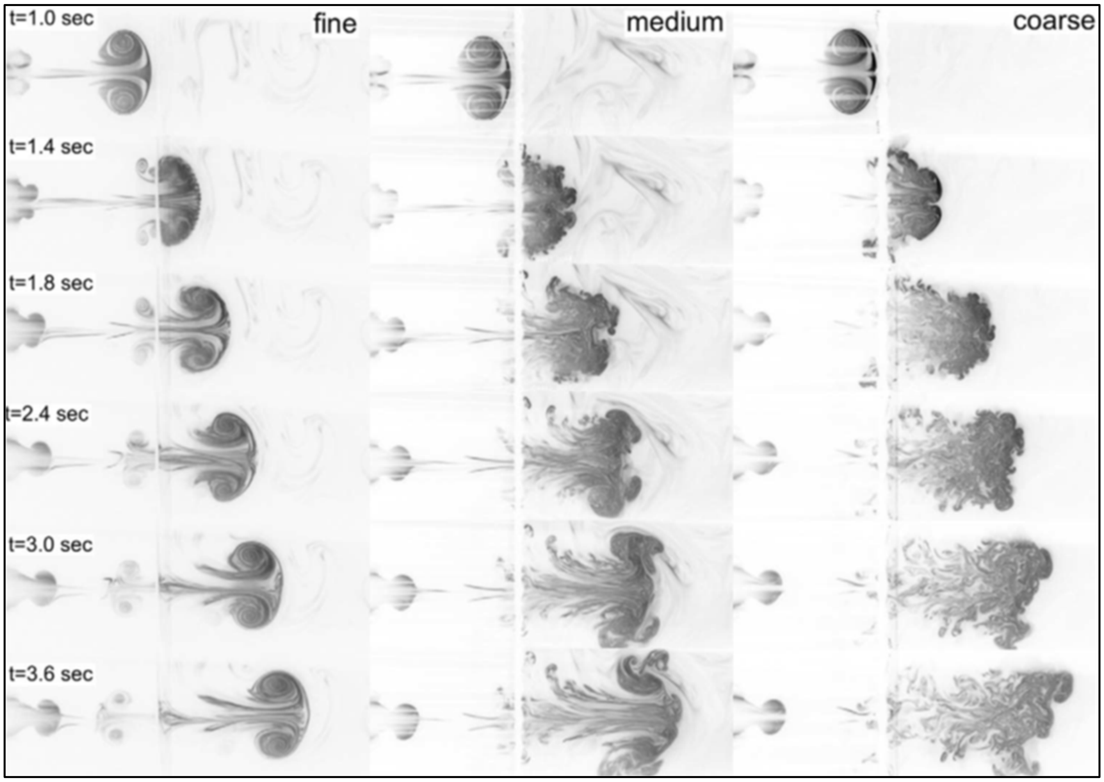

Figure 1-5 Evolution of the vortex reformation over time for different grid size, taken from [14], p. 8

Naaktgeboren *et a*l. [16] also measured the sensitivity of the kinetic energy dissipation rate to the screen porosity. The authors highlight the exponential relationship between the porosity and the dissipation rate, with the more restrictive media blocking more of the incoming energy from being transmitted downstream. That being said, even the most porous screen (79%) provided a TKE reduction of 40-60%.

Musta and Kruger [18] focused on the effect of the grid spacing and porosity, but used grids with a very large wire diameter (3.18mm). Placing multiple screens in series has a considerable effect on the evolution of the transmitted vortices. As the vortex ring penetrates the first mesh, it splits into several vortical structures. For the cases with the lowest porosity (56%), these vortical structures stretch along the channels created by the pores. Increasing the Reynolds number increases the vorticity level, but the structures remain qualitatively similar. For the cases with the highest porosity (84%), the vortical structures tend to diffuse radially between the screens and seem to be less affected by the Reynolds number. None of the vortex ring could reform past the first screen, with most of the vortical sub-structures dissipating completely beyond the third screen. The investigators noted that even a small misalignment between the nozzle centerline and the screen symmetry planes would cause the vortex ring to disintegrate past the first screen. This observation was not made by other authors, but will be investigated further in this project.

Regarding the effect of the distance between the screens, the smallest gap was the most effective at dissipating the vortex ring and prevented the formation of transmitted rings. The largest gap allowed secondary vortices to form downstream, but could not reform into a coherent vortex ring beyond the third screen.

Regarding the reformation mechanism, the author observed that as the vortex splits past the first grid, the secondary vortices start to roll-up, but can only fully develop if the incidence angle is sufficiently steep to avoid hitting the next screen.

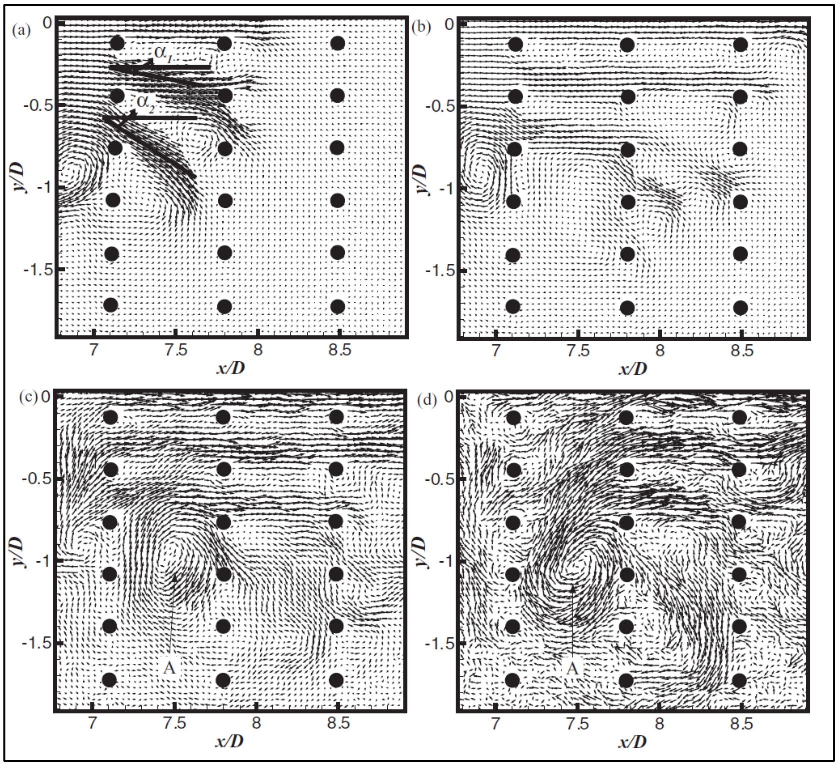

Figure 1-6 Instantaneous vector fields showing the reformation of the transmitted vortex over time. The vortex flows from left to right. Re = 3000, φ=56%. Taken from [17], p. 10

Globally, increasing the intergrid spacing allowed for the formation of larger secondary vortices between the screens. This can be partly explained by what the authors called the “critical roll-up deflection angle” which decreases as the gap between the screens increases. As the vortex moves over the rods, the flow field is deflected by some amount. If the deflection angle is sufficiently steep, the flow field will begin to curl before it reaches the next screen. Increasing the gap also provides a larger volume for the vortical structure to grow without hitting boundaries. In the case of a vortex ring, the rotation is maximum within the ring itself, but fairly low in the center. This may explain why the roll-up of secondary vortices was predominantly present further away from the center.

1.4 Discussion and definition of the objectives

The key takeaways of the previous investigations are that the porosity of the screen has a significant impact on the energy dissipation rate, with the more porous screens providing the least resistance to the passage of the flow and thus being less effective at reducing the transmission of the turbulent kinetic energy. It was shown that the size of the mesh wires is another key variable, with the larger rods being more effective at breaking up the jet vortex. The finer meshes will chop the vortex ring into jets, but do little to disrupt the transmitted vortical structure which can reattach and reform past the screen. Coarser grids, on the other hand, break the incident vortex ring into secondary vortical sub-structures as it flows over the grid. Placing multiple screens in series had a compounding effect on the energy dissipation, with most of the transmitted vortices being undetectable beyond the third grid. The effect of the interstitial gap between the grids was somewhat marginal in the available study, but this might be a result of the very large rods used in the experiment. Keeping in mind the conclusions from Hrynuk *et al.* on the influence of wire diameter, it is not obvious whether the grid spacing or the wire diameter mostly contributed to the vortex dissipation.

On the topic of a vortex impinging on a porous structure, most of the research focuses on heat transfer performance (heat exchangers, porous burners and heat sinks). The ability of a cellular structure to dissipate vortical energy and how it does so remain vastly unexplored

questions. On the one hand, this is a very niche topic with few industrial/commercial applications. On the other hand, investigating the breakdown of a vortex inside a porous structure is challenging. Experimentally, flow visualization requires the porous media to be made of a transparent material and its reflective index must match the fluid used. This greatly limits the choice of materials and therefore the types of structures than can be manufactured.
One aspect of the influence of the porosity on vortex breakdown which was not observed in other studies is the size of the transmitted jets. For a given wire diameter, increasing the porosity cuts the vortex ring into much larger sub-structures. While this is somewhat obvious, since a larger pore will allow a larger structure to pass through, it isn't immediately clear how it impacts the coherence of the transmitted jets i.e. do larger jets recombine as rapidly as smaller ones?

The main objective of this study is to provide guidelines towards the design of porous structures capable of replacing the current foam within a DLE gas-turbine combustor.
The baseline properties of the foam are obtained from CT-scan, which serve as the baseline to generate different lattice structure candidates using nTopology. These structures are analysed numerically to understand the influence of cells geometry and how tortuosity and porosity influence the permeability.
Next, a design of experiment is developed to study the influence of the fundamental lattice properties (strut diameter, pore size and grid spacing) in the context of assessing their vortex-breakdown performance. This investigation relies on stacks of individual grids to simplify the problem and is performed using the URANS solver in Star-CCM.
A custom wind tunnel, based on the numerical model, is then fabricated and the simulation conditions are reproduced to validate the model.

CHAPITRE 2

CHARACTERIZATION OF THE EXISTING FOAM AND REPLACEMENT LATTICE STRUCTURES.

The following chapter was presented as a poster during the Gas Turbines for Energy Network (GTEN) 2023 symposium in Banff, Ab, Canada on October 16th-18th 2023.

This chapter presents the characterization steps of the conventionally-made Retimet foam and the process behind the generation of the replacement lattice structures. It begins with the 3D reconstruction process using CT scanning, followed by numerical and experimental measures of the foam's flow properties, specifically its permeability and tortuosity. This chapter concludes with the generation of various design candidates and a comparison of their flow properties.

2.1 3D reconstruction

The first step in analysing the foam was to reconstruct a 3D model using CT scanning (Nikon XTH 225, resolution = 10 microns). The samples were obtained from a block of virgin foam, cut by wire-EDM. Two of samples used in flow testing were then scanned. The analysis was done in VG Studio 3.1.

Using the Foam Structure Analysis (FSA), several key properties were measured, including the size and volume of the pores, their spatial distribution, as well as the diameter of the struts. A snippet of the results is presented in Figure 2-1. The data was later processed using MATLAB. The merge threshold was set to 1% and the precision to standard.

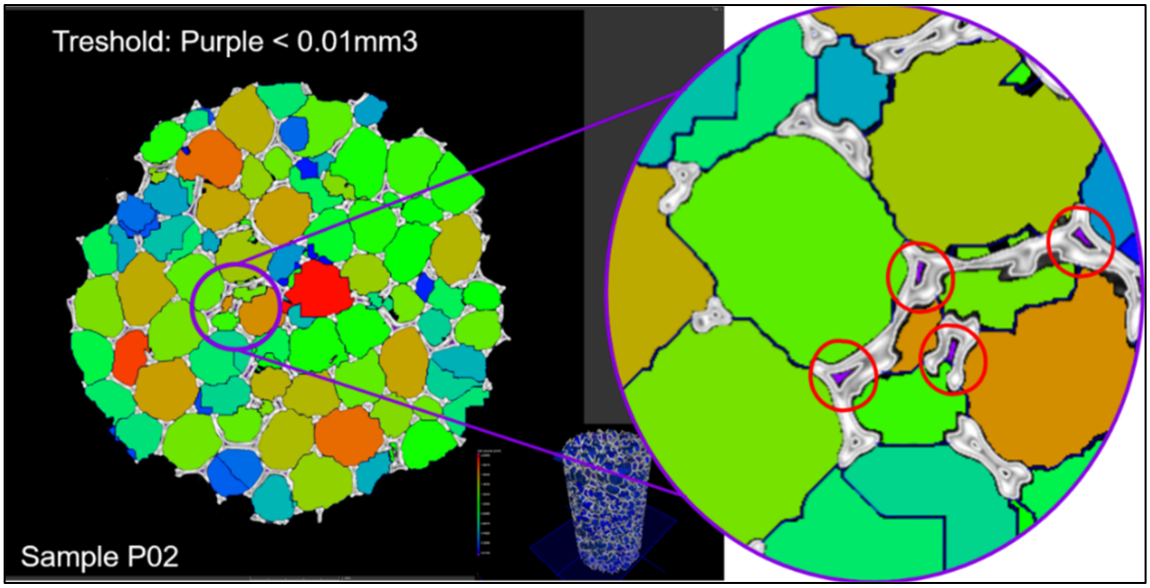

Figure 2-1 Image obtained from the CT-Scan showing the internal pores of the struts. The pores with a volume inferior to the threshold are circled in red

The vast majority of the pores detected in the foam analysis were internal pores left by the manufacturing process. Those pores are located inside the struts and are not wetted by the air. These internal pores are identified by the red circles in Figure 2-1. A pareto analysis, presented in Figure 2-2, revealed that over 80% of the counted pores had a cell volume inferior to 0.01mm^3, but their cumulative volume accounted for less than 1% of the total porosity. An exclusion threshold was set to 0.01mm^3 to remove these pores from the analysis since they do not affect the airflow characteristics of the foam and skew the pore properties.

This was validated by running a capillary pressure analysis (CPA) which simulates a quasi-static drainage experiment and can therefore detect the non-wetted surfaces. The total pore volume detected by the CPA is around 18% larger than what was detected using the foam analysis. The average cell diameter is 7% bigger, but the standard deviation for the cell diameter is 46% smaller. This discrepancy is explained by the methods employed for the determination of the cell size. The FSA calculates the volume using a number of integral geometric and topological quantities derived from the Minkowski functionals. The CPA method defines the cell volume by inscribing the largest sphere possible within the pore surface. The table below presents these results. Note that the FSA-Pareto column reports the results obtained with the FSA after applying the exclusion threshold. The different methods are well explained in the VG Studio help documentation.

Table 2.1 Average pore size and volume of the foam for different measuring techniques.

Sample B02	**FSA – Raw**	**FSA – Pareto**	**CPA**	**FSA vs CPA**
Average Cell Volume (mm^3)	0.082	0.580	0.724	25%
Average Cell Diameter (mm)	0.538	1.034	1.104	7%
Std. Dev. (Vol) (mm^3)	0.273	0.494	0.077	-84%
Std. Dev. (Dia) (mm)	0.804	0.980	0.527	-46%
Total Pore Vol. (mm^3)	1119.75	1119.75	1318.00	18%
Accessible Pore Vol. (mm^3)	-	1109.33	1318.14	19%

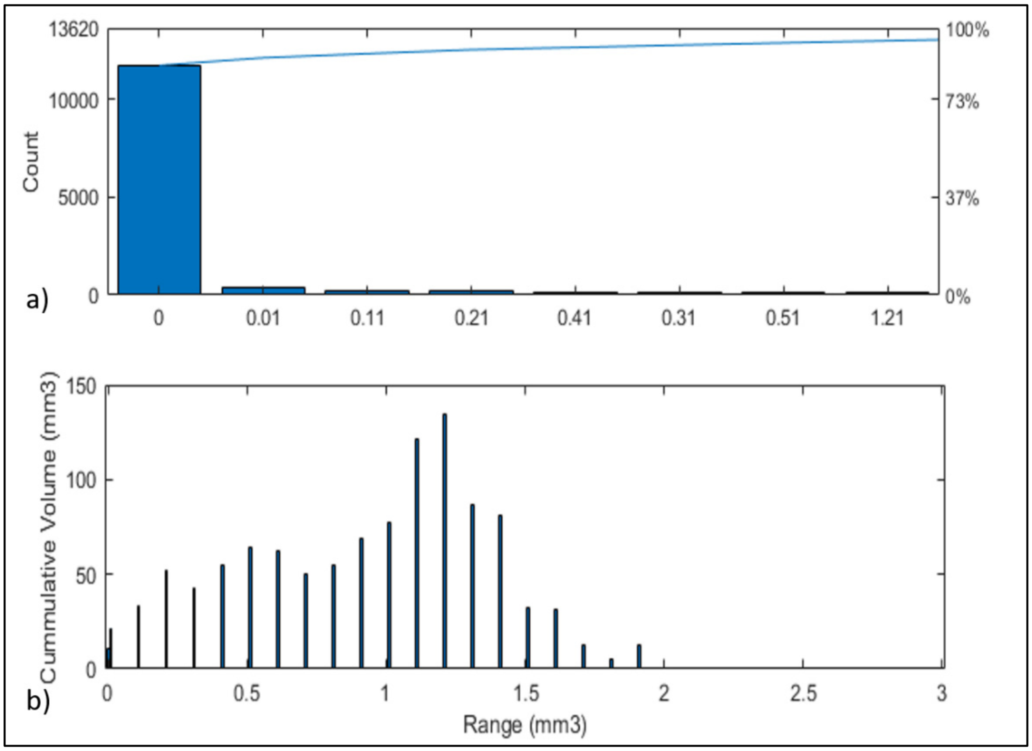

Figure 2-2 Results of the Pareto analysis. a) Number of pores for the 10 most common sizes, b) Cumulative volume of the pores by volume group

2.2 Flow properties

The permeability of the foam was first evaluated in VG Studio using the Absolute Permeability Experiment (APE) over a cylindrical region of interest (Ø5mm x 16mm). The inlet and outlet planes were located approximately 1mm inward because the extremities of the foam were a bit damaged. The simulation was done over 80% of the total volume to mitigate the wall effects. The same approach was used for the lattice structures; a region of interest was exported and reused across all the samples, ensuring boundary conditions were identical across the samples.

In addition to the numerical simulations, the permeability of the foam samples was measured using a low-velocity water tunnel designed by Timercan *et al*. [19], shown in Figure 2-3. The equipment consists of a pump, a flow meter, two pressure taps connected to a differential pressure sensor and the tunnel itself. The pressure sensor and the flow meter are connected to an acquisition card and the results are logged in using a LabView tool. The data was saved and later post-processed in MATLAB.

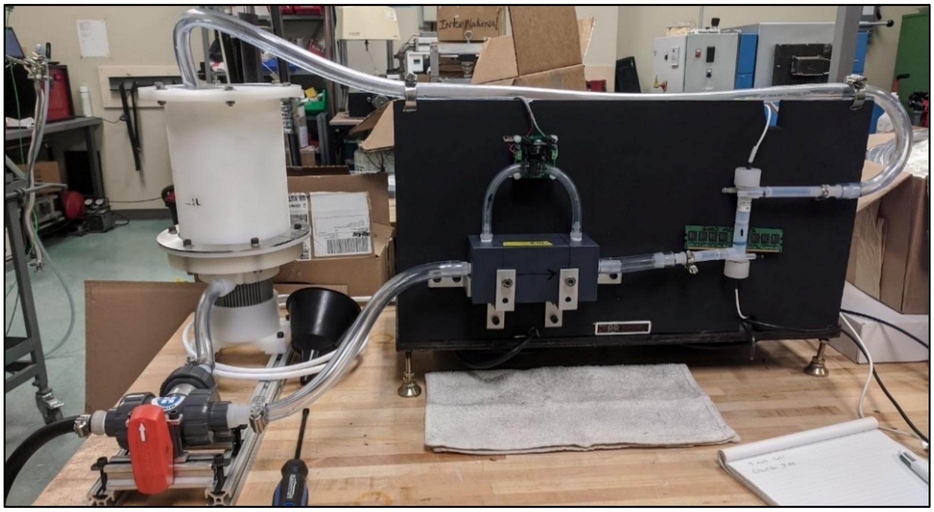

Figure 2-3 Flow rig to measure the pressure drop of the foam samples

Each test begins by wrapping the sidewall of the sample in a layer of PTFE tape to seal the walls and ensure a tight fit. The system is then primed by gradually increasing the pump speed until no bubbles were visible in the lines. The pump was then stopped, and the sensors were zeroed. The flow was progressively increased from 0.0 to around 6.0 l/min in increments of 0.1 l/min. At each step, we allow the flow to stabilize for a few seconds before starting the acquisition for 5 seconds. The upper limit of the flow rate was limited by the pressure sensor saturating. The flow was then gradually reduced, again taking measurements at every step.

A total of five samples were tested, each measuring Ø10mm x 18mm long. The samples were all cut by wire-EDM from the same block.

The results from the water-tunnel test are presented in Figure 2-4. Although each sample was cut from the same block, a slight variation in the permeability is to be expected. As the velocity increases, the effect of this variation on the pressure gradient becomes more obvious. Two runs were needed for the fifth sample due to a recording error during the first run.

The four permeability models, presented in section 1.2, were then fitted to the data. The models were fitted using the permeability, pore diameter, and porosity values from the permeability analysis in VG studio. Input values and fitted coefficients are presented in Table 2.2. The fit quality is measured using the R2 criterion, and the coefficients are summarized in Table 2.3. Three models (Ashby, Ergun and Forchheimer) are indistinguishable and exhibit high fidelity with a R2 of 0.993. The cubic model did not perform as well.

Table 2.2 Foam and water properties used to calculate the coefficients

Permeability (m^2)	**Porosity (-)**	**Density (kg/m^3)**	**Dynamic Viscosity (Pa•s)**	**Pore Diameter (m)**
1.096E-08	93.4%	1000	1.81E-03	1.1 E-03

Table 2.3 Experimentally-fitted coefficients for the permeability models

Model	**Ashby (Eq. (1-7))**		**Cubic**	**Ergun (Eq. (1-6))**		**Forchheimer (Eq. (1-3))**
R2	0.9929		0.9326	0.9928		0.9927
Coeff	**Zeta**	**m**	**Gamma**	**ErgA**	**ErgB**	**Cf**
Fitted	4.127	0.05454	0.004549	1.41E+04	42.2	0.2934
Predicted	-	-	-	150	1.75	0.2372 (Eq (1-4))

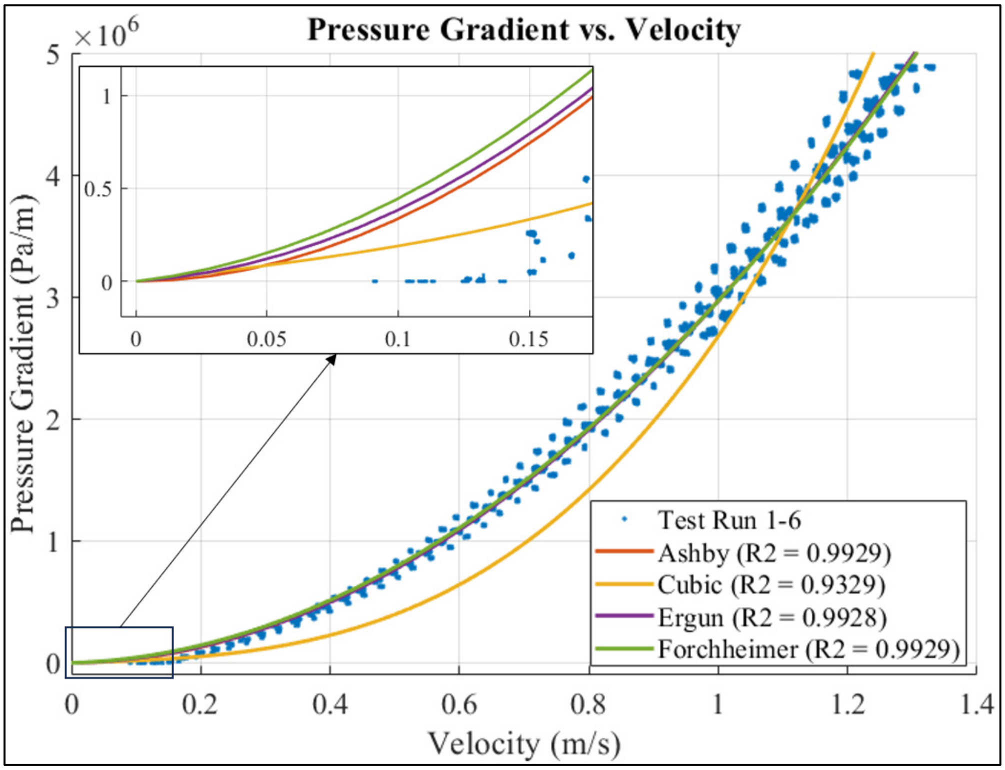

Figure 2-4 Pressure gradient vs. Velocity

2.3 Generating lattice structures

The next step is to start generating some lattice structure candidates to replace the existing foam. Using the results from the CT-scan as a baseline, the mean pore diameter should be in the range of 1.0mm, with strut size around 0.15mm. Based on past experience, fabricating features this small using laser powder bed fusion is very challenging, both in terms of feature definition and strength. For this reason, the minimum strut size was increased to 0.25mm, which is more realistic in the context of industrial production.

A series of lattice structures were developed using nTopology and were subsequently tested in VG Studio using the same parameters to estimate the flowing properties. Seven different types of lattices were trialed. To speed up the design process, the structures analysed were kept small (Ø5mm x 10mm), akin to the Representative Element Volume (REV) approach commonly used in CFD. The samples were sufficiently large to fit at least 50 pores per REV.

Since the simulation in VG assumes the flow to be linear, the effect of the stochasticity is negligeable, thus 50 pores per REV was deemed sufficient. The main concern was to avoid running into wall effects.

The body-centered cubic (BCC), diamond (DIA) and face-centered cubic (FCC) lattice structures were selected because they are relatively easy to print and allow for more liberty in how we can twist the structures to reduce the channeling effect. The hex-lave (HEX) and Kelvin (KEL) cells were selected because of their large pore diameter. To better understand the influence of the randomness on the flow, two stochastic structures, the orthofoam (ORT) and the Voronoi (VOR), were also put to the test. Figure 2-5 presents the pressure gradient of different candidates as a function of their tortuosity and porosity.

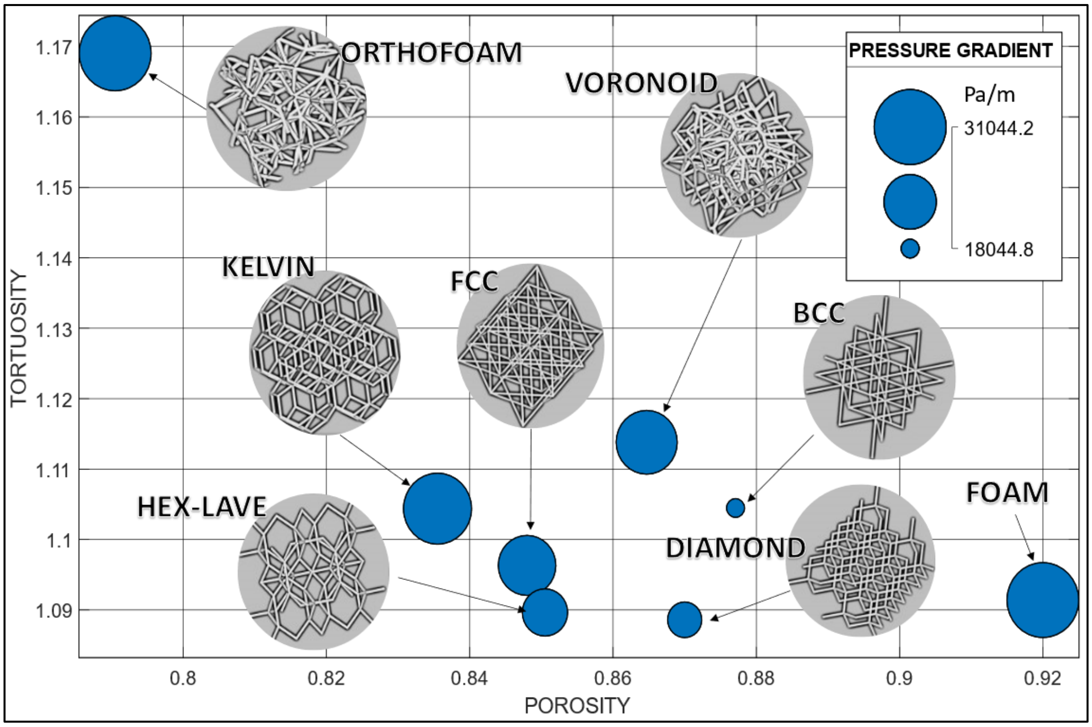

Figure 2-5 Pressure gradient of different lattice structures as a function of porosity and tortuosity

The following table presents the design parameters and the resulting porosity, pressure drop, permeability and tortuosity.

Table 2.4 Geometrical and flow properties of the foam and lattice structures

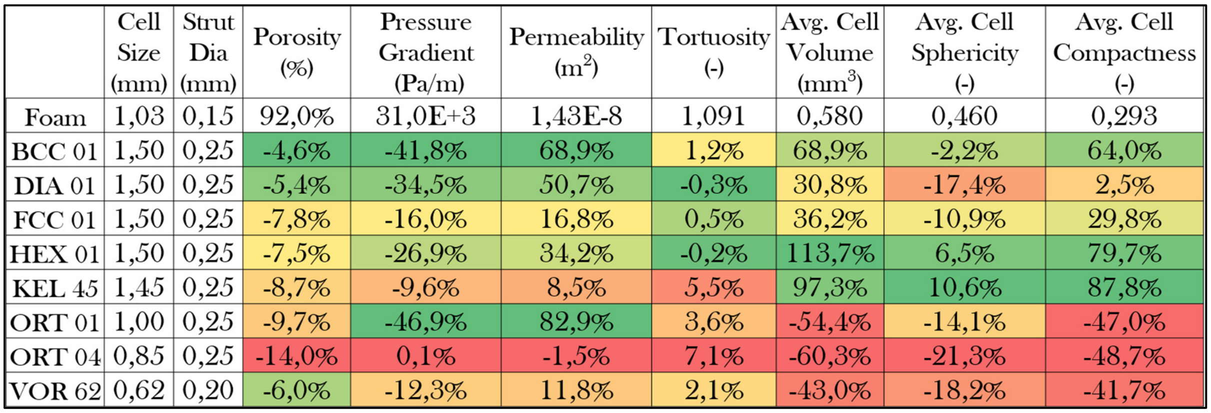

	Cell Size (mm)	Strut Dia (mm)	Porosity (%)	Pressure Gradient (Pa/m)	Permeability (m^2)	Tortuosity (-)	Avg. Cell Volume (mm^3)	Avg. Cell Sphericity (-)	Avg. Cell Compactness (-)
Foam	1,03	0,15	92,0%	31,0E+3	1,43E-8	1,091	0,580	0,460	0,293
BCC 01	1,50	0,25	-4,6%	-41,8%	68,9%	1,2%	68,9%	-2,2%	64,0%
DIA 01	1,50	0,25	-5,4%	-34,5%	50,7%	-0,3%	30,8%	-17,4%	2,5%
FCC 01	1,50	0,25	-7,8%	-16,0%	16,8%	0,5%	36,2%	-10,9%	29,8%
HEX 01	1,50	0,25	-7,5%	-26,9%	34,2%	-0,2%	113,7%	6,5%	79,7%
KEL 45	1,45	0,25	-8,7%	-9,6%	8,5%	5,5%	97,3%	10,6%	87,8%
ORT 01	1,00	0,25	-9,7%	-46,9%	82,9%	3,6%	-54,4%	-14,1%	-47,0%
ORT 04	0,85	0,25	-14,0%	0,1%	-1,5%	7,1%	-60,3%	-21,3%	-48,7%
VOR 62	0,62	0,20	-6,0%	-12,3%	11,8%	2,1%	-43,0%	-18,2%	-41,7%

As previously mentioned, designing a porous structure is particularly difficult because the shape of the pore itself plays a major role in the flow properties. From the table above, two pairs exemplify this well. FCC-001 and HEX-001 have essentially the same porosity (0.3%), and very similar tortuosity (0.7%), but their pressure gradient and permeability are very different, and the difference cannot be explained by the two properties typically used to calculate the pressure gradient i.e., the porosity and the tortuosity. Another stark example is the baseline sample and the VOR-062, which have a wide gap in terms of porosity (most porous vs. least porous structure) and tortuosity, but exhibit the same pressure gradient (+0.1%) and nearly identical permeability (+1.5%).

Considering the different permeability models, one would expect that reducing the porosity and increasing the tortuosity would lead to a greater pressure gradient, yet the least restrictive sample tested (ORT-001) is significantly less porous than the baseline (83% vs. 92%), and somewhat more tortuous (+3.6%), but has a pressure gradient nearly half that of the baseline (-47%).

By plotting the table in a radar chart, shown in Figure 2-6, we can notice the pressure gradient varies inversely to the permeability, which is expected as the permeability is directly related to the pressure gradient in the Darcy-Forchheimer model. On the other hand, the absence of correlation between the porosity, the tortuosity and the pressure gradient is quite obvious.

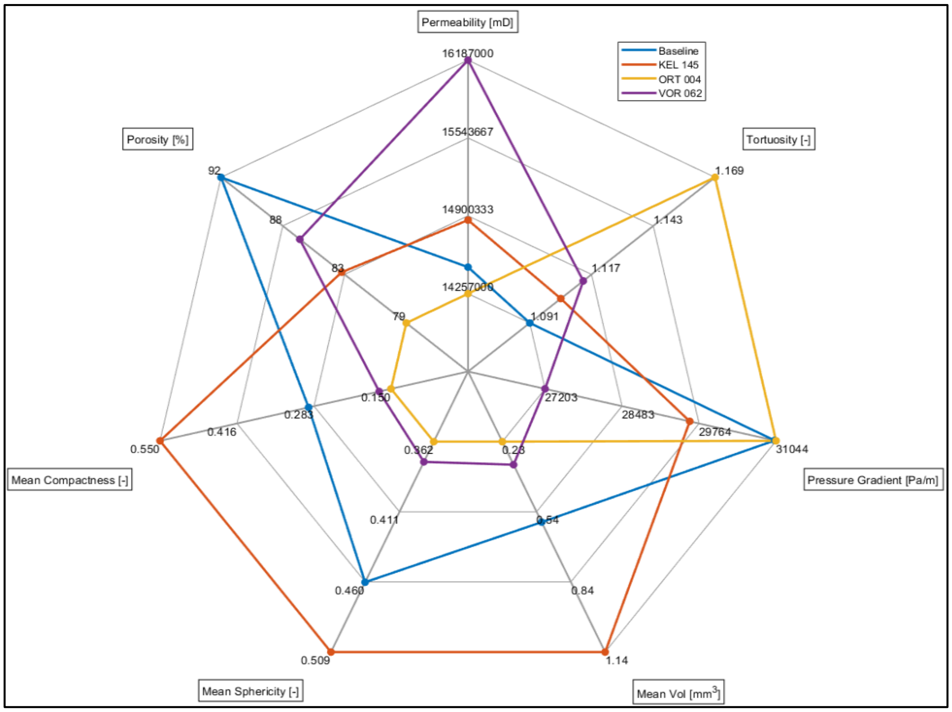

Figure 2-6 Radar plot of the geometrical and flow properties of lattices structures and foam

Pushing the analysis a bit further, the foam analysis was done on the three samples that most closely matched the baseline (KEL145-30, ORT-004, VOR-062) in the hopes of detecting a trend in the pore aspect itself, namely the sphericity and compactness, but the absence of correlation between the potential design variables is again evident. The samples with the smallest and biggest pressure gradient are the ones with the smallest average pores. We can also observe that the two samples inducing the largest pressure gradient are also the least and most tortuous samples, and are the least and most porous. In terms of the mean compactness and mean sphericity, it seems the only correlation is with the average pore size itself.

2.4 Conclusion

This chapter presented the steps taken to characterize the existing foam and generate potential alternatives using various lattice structure geometries. First, foam samples, cut from a virgin block, were CT-scanned and analysed using VG Studio. The raw data from the foam analysis revealed the presence of a significant amount of very small pores within the foam, which turned out to be voids inside the struts themselves. Once these non-wetted pores were removed from the results, the mean pore size and mean strut size were calculated and served as the starting points for the generation of the replacement lattice candidates. The permeability of the foam samples was also measured numerically, using tools from the VG Studio suite, and experimentally, using a custom-built water tunnel.

Next, seven different lattice structures were created and their geometries were iteratively adjusted by analysing the samples in VG studio. Replicating a structure with equivalent flow properties as the foam proved to be significantly more complex than anticipated. One of the biggest challenges with using permeability and tortuosity as design targets is the lack of explicit control over these properties in the design process. This means that every structure must be analysed, which is a tedious and time-consuming process. In addition, the lack of correlation between permeability, tortuosity and pressure gradient indicates these properties should probably not be design targets.

Another avenue is to design the structures around the geometrical properties of the foam, specifically the pore size and shape. However, this proved to be ineffective as well. For one, there is not a good correlation between the pressure gradient and the pore size. For two, minute changes in the pore size can completely change the flow properties of the structures (ORT-01 vs ORT-04).

Based on these results, a change in the approach is needed. Working with seven different structures at once casts a net far too wide to be manageable. One option would be to focus on a single structure, but the issues related to the lack of direct control over the lattice's "key" properties (permeability, tortuosity, pore shape…) would remain, and the work put into creating the "perfect" lattice would likely not transfer well to other conditions. A more pragmatic option would be to change the focus towards a more fundamental understanding of how the basic lattice structure parameters, such as the pore size, porosity and strut diameter influence the flow characteristics of the structures. This approach offers several benefits, namely that the parameters can be directly controlled and the trends that emerge should be widely applicable.

CHAPITRE 3

Vortex-Breakdown Efficiency of Planar Regular Grid Structures—Towards the Development of Design Guidelines

Julien Sirois [1], Marlène Sanjosé [2], Fabian Sanchez [3], Vladimir Brailovski [4]

[1,2,4]. École de Technologie Supérieure, Montréal, Qc, Canada
[1,3]. Siemens Energy Canada Limited, Montréal, Qc, Canada

This paper was published *Fluids*, February 2024, as part of the special issue *Turbulence and Combustion*.

3.1 Avant-propos

This section presents the numerical protocol developed to study the influence of the grid parameters on their vortex-breakdown performance. It begins with a review of the state of the art, followed by a presentation of the numerical model. It then elaborates on the design of experiment and the reasoning behind the key performance indicators. The results are then presented and discussed. The chapter concludes with a case study showing how the results can help guide the design of an ideal grid stack.

3.2 Résumé

Le travail présenté ici vise à fournir des lignes directrices pour la conception de structures d'amortissement des tourbillons. Un plan d'expérience a été mis au point pour étudier les effets individuels et combinés des propriétés géométriques de structures planes à grille régulière, c'est-à-dire le diamètre du fil, la porosité et l'espacement entre les grilles, sur leurs performances en matière d'amortissement des tourbillons. Les simulations ont été effectuées à l'aide d'un solveur RANS instationnaire commercial. Le modèle s'appuie sur l'effet de rue de Von Karman pour générer des tourbillons dans un tuyau qui sont convectés en aval, où ils interagissent avec un réseau de grilles. L'efficacité de la décomposition des tourbillons est

caractérisée par la perte de charge, l'énergie cinétique turbulente résiduelle, l'homogénéité de l'écoulement et la taille des tourbillons transmis. Le diamètre du fil s'avère être un levier de conception important car il affecte le niveau de distorsion des tourbillons transmis. L'augmentation du nombre de grilles accroît la perte de pression, mais leur contribution à la rupture des tourbillons est par ailleurs limitée lorsque le diamètre du fil est faible. L'influence de l'espacement des grilles dépend fortement du diamètre du fil et de l'alignement des grilles. Par exemple, la minimisation de cet écart réduit la perte de charge pour les configurations en ligne, mais augmente la perte de charge pour les configurations décalées.

3.3 Abstract

The work presented here aims to provide design guidelines to create vortex-damping structures. A design of experiment was developed to investigate the individual and combined effects of the geometrical properties of planar regular grid structures, i.e., the wire diameter, the porosity, and the inter-grid spacing, on their vortex-breakdown performance. The simulations were carried out using a commercial unsteady RANS solver. The model relies on the Von Karman street effect to generate vortices in a pipe which are convected downstream, where they interact with an array of grids. The vortex-breakdown efficiency is characterized by the pressure drop, the residual turbulent kinetic energy, the flow homogeneity, and the size of the transmitted vortices. The wire diameter is shown to be an important design lever as it affects the level of distortion of the transmitted vortices. Increasing the number of grids augments the pressure loss, but their contribution to vortex breakdown is otherwise limited when the wire diameter is small. The influence of grid spacing strongly depends on the wire diameter and grid alignment. For instance, minimizing this gap reduces the pressure drop for the inline configurations, but increases the pressure drop for the offset configurations.

3.4 Introduction

Industrial gas turbines are a key component in power generation. To maintain their competitiveness, operators strive to reduce their operating cost and manufacturers continuously work to improve efficiency of their engine. One avenue to improve efficiency is in the optimization of air management in the combustion system by reducing the pressure losses upstream of the combustors.

A particularity of Dry Low Emission (DLE) combustion systems is that the air and fuel are thoroughly mixed upstream of the combustion chamber. This ensures a very clean and uniform combustion, allowing these engines to achieve very low NOx levels. However, it is primordial for the highly turbulent flow field with pronounced non homogeneity from the successive blade cascade wakes coming from the compressor stage to be conditioned before it can enter the combustion system, as large vortices can lead to the formation of lean air pockets which are detrimental to combustion uniformity and can result in excessive NOx levels and harmful combustion dynamics [1]. Stochastic structures like metal foams are highly effective at damping vorticity and homogenizing the flow, and have been used successfully for many years. So why fix it if it's not broken? Because they incur a considerable pressure loss impacting the overall efficiency.

Considering the capabilities of modern additive manufacturing techniques, the idea of developing a substitute lattice structure germinated, with a focus on reducing the pressure loss while retaining the homogenizing power. Confronted with an abundance of lattice types and scarce literature of their interaction with vortices, the focus quickly shifted to understanding how the geometrical properties of a lattice structure influence their vortex breakdown performance by studying grids.

The vortex-porous screen interaction has been studied by a few authors in the past, each typically focusing on a single variable at a time. These studies, experimental for the most part, employed various visualisation techniques for their measurements. All the reported studies relied on a piston to create a vortex ring moving through a stationary fluid inside a large tank (water [14-16], glycerin [17, 18] and air [20, 21]). The Reynolds number, based on the piston diameter and exit velocity, ranges between 1000-6000 in the reported studies in Table 3.1.

Table 3.1 Comparison of the previous studies on the interaction of vortex rings and porous screens

Authors	Method	φ [%]	d_w [mm]	ε [mm]	Re
Hrynuk e*t al.* [14, 15]	PLIF, MTV	64	0.18-2.67	Single	2300-4200
Musta & Kruger [17, 18]	DPIV	50-84	3.18	25, 50	1000-3000
Naaktgeboren [16]	DPIV, PLIF	44-79	0.71	Single	3000, 6000
An *et al.* [20, 21]	Fog, RANS	30-80	1.00	Single	700-3000
Cheng et al. [22]	LBM	0-100	0.015-0.1*	Single	500-5000
Present study	IU-RANS	55-85	0.25-1.00	2.5-7.5	3200

*The wire diameter in Cheng et al. is a function of the vortex diameter.

Both qualitative and quantitative techniques were adopted by the investigators to study behaviour of vortices passing through grids. Planar Laser-Induced Luminescence (PLIF) and fog generators were used to visualize the vortex and study how it deforms and reforms. The use of trackers was also employed by some authors (particle image velocimetry (PIV) and molecular tagging velocimetry (MTV)) to measure the variation of the vortex size and the kinetic energy. Both techniques are complimentary. This has also been investigated numerically by some authors [20-22].

Past studies typically focused on a single parameter at one time. Naaktgeboren *et al.*[16] and An *et al.* [20, 21] focused on the effect of porosity while Hrynuk *et al.*[14, 15] studied the influence of the grid wire diameter. The effect of placing multiple grids in series was studied by Musta and Krueger [17, 18] who also varied the porosity. Finally, Cheng *et al.* [22] used numerical simulations to study the influence of the porosity, wire size and grid thickness.

It was observed that the effect of the porosity primarily impacts the radial expansion of the vortex ring and the intensity of the residual kinetic energy. The restriction caused by the lower porosity grids resulted in an interaction similar to a solid wall, with the radial expansion of the vortex ring as it approached the porous screen [16]. When the porosity was large, this radial distortion of the primary vortex was not observed. The transmitted kinetic energy was strongly dependant on the grid porosity, but even very porous grids reduced the turbulent kinetic energy (TKE) transmission by 40-60% [14, 15, 17, 18, 20, 21]. The size of the transmitted vortical sub-substructures varied substantially with the porosity, larger openings permitting larger sub-structures to form, but were weakly affected by intergrid spacing.

Wire diameter was shown to have the greatest effect on the reformation behavior of the vortex downstream. When the diameter was small (d_w <0.50 mm), the vortex reformed instantly with minimal distortion of the core. In the intermediate range (0.50< d_w <1.60mm), the vortex core distortion increased with the wire diameter, and delayed the reformation of the ring. For larger wires (d_w >1.60 mm), the transmitted vortex core was too disrupted to be reformed downstream. Notably, small vortical sub-structures formed downstream of the larger wires, consistent with the vortex shedding behind a circular bluff body [14, 15].

The effect of placing multiple grids in series was studied by Musta and Krueger [17, 18]. The vortex rings systematically collapsed into multiple vortical sub-structures passed the first grid, with no coherent structures beyond the third grid, although the large wire size of the grids employed likely contributed to the vortex breakdown to some extent. The effect of the intergrid spacing was stronger when porosity was large. Cheng *et al.*[22] observed similar trends when increasing the thickness of the grids.

On the influence on the jet Reynolds number, a transition in the vortex regime, from laminar to turbulent was observed [16] around Re=1000. Beyond that, increasing the Reynolds number essentially scales the kinetic energy and the penetration of the vortex rings. It was also observed that the rate of decay of the transmitted TKE increases with Re [14, 15, 17, 18]

This topic was also investigated numerically by some others, again using a piston to generate a vortex ring. Cheng *et al.* [22] used the Lattice Boltzmann Method (LBM) to measure the effect of porosity, wire diameter and Reynolds number. The results obtained were generally in good agreement with the experimental results obtained by previous authors [14-18].

More recently, An *et al.* [20, 21] reproduced their experimental tests using a classical unsteady Reynolds Averaged Navier-Stokes (RANS) solver for incompressible fluid. The authors used the SIMPLEC algorithm for the pressure-velocity coupling and the PRESTO (PREssure STaggering Option) for the pressure interpolation. The results obtained numerically regarding the trajectory of the vortex core and the influence of the Reynolds number were in good agreement with their experimental results. This indicates that IU-RANS can also be a good option to study vortex breakdown.

The work presented here brings forth three novelties. Firstly, the design of experiment (DoE) developed for this investigation covers all the grid parameters, which is essential to understanding their individual and combined effects on vortex breakdown. The knowledge gained is crucial in the context of developing design rules to guide the conception of more efficient geometries.

Secondly, in addition to the residual turbulent kinetic energy and the transmitted vortex size, two new key performance indicators (KPI) are evaluated: the flow field uniformity and the pressure loss. These KPIs are detailed in section 3.5.6.

Lastly, where previous authors used a piston to generate a vortex ring moving through a stationary fluid inside a large tank, this study generates vortices using the Von Kármán street effect by placing a cylindrical bluff body perpendicular to a moving fluid confined inside a pipe. The use of a bluff body to generate coherent vortex structures allows the grids to be tested in the presence of mean flow. At the same time, vortex sizes and turbulent intensities can be evaluated, as well as the pressure losses and the flow homogenization across the grids. This vortex generation method is a classical approach to flow interaction problems. Cylindrical bluff bodies are frequently used to mimic stage interaction problems in turbomachinery [23, 24]. This approach is preferred because it is more representative of the actual flow in a combustor where coherent vortices are convected with the mean flow. In addition, this investigation is done using an unsteady RANS solver. The low computational cost of this method is essential to simulate all the configurations in the test matrix.

Section 3.5 presents the optimisation criteria, the methodology, the DoE and the KPIs. Section 3.6 presents the results, and a case study is presented in Section 3.7.

3.5 Methodology

3.5.1 Optimisation Criteria

In the context of developing a more efficient alternative to metallic foams, the first step is to establish the key performance indicators (KPI). The first metric is the pressure loss (ΔP), which shall be minimized. A pressure loss leading to the combustor takes away some of the energy which would otherwise be used in the combustion air or for cooling. The second metric is the transmitted turbulent kinetic energy (TKE), i.e., the residual energy downstream of the grids. Depending on the flame type, a turbulent flow may be desirable because it enhances the mixing of the air-fuel mixture leading to a more uniform combustion. The third KPI is the uniformity of the velocity field, which should be as homogenous as possible. The presence of streak within the flow can cause instability. The final metric is the size of the transmitted vortices. Large vortices are never desirable because the fuel cannot penetrate inside the vortex, which can result in lean air-pockets. This is particularly important with premix systems which are more prone to auto-ignition due to the long time required for the air and fuel to mix in the premix chamber upstream of the flame front [1]. This contrasts with conventional aero-style combustors where the fuel is injected into the airstream just a few millimetres before of the flame.

3.5.2 Computational Domain

The computational domain and the important dimensions are represented in Figure 3-1. In its baseline configuration, the model simply consists of a Ø50 mm x 450 mm long pipe with the cylindrical bluff body (d=5 mm), perpendicular to the flow, located 200 mm downstream of the inlet. As the air passes over the bluff body, vortices form and shed periodically, creating a Von Karman alley. The shedded vortices are then convected downstream by the flow. For the DoE, grids are introduced 35mm downstream from the bluff body axis. The domain is reduced by using a symmetry plane along the length of the tube. Eight virtual planes (Figure 3-1: P_{In}, P_{BB}, P_{Grid}, P_{M1}, P_{M2}, P_{M3}, P_{Out} and the XY cross plane) are created to monitor the solution. The blockage ratio caused by the bluff body is 0.1, which is relatively small and should not affect the vortex dynamics [25]. This geometry imitates the passage leading to the combustor where the foam is employed and replicates similar confinement effects.

The effect of the symmetry plane was verified by comparing two complete models (one inline, one offset) with the half-models reported in this paper. The differences in the KPIs between the half and full models are in the order of +/- 5%. It should be noted that the offset configurations are still roughly symmetrical since the grids are regular i.e., the wires are not randomly distributed. Overall, the effect of the symmetry plane is acceptable and represents a good trade-off between accuracy and computational costs.

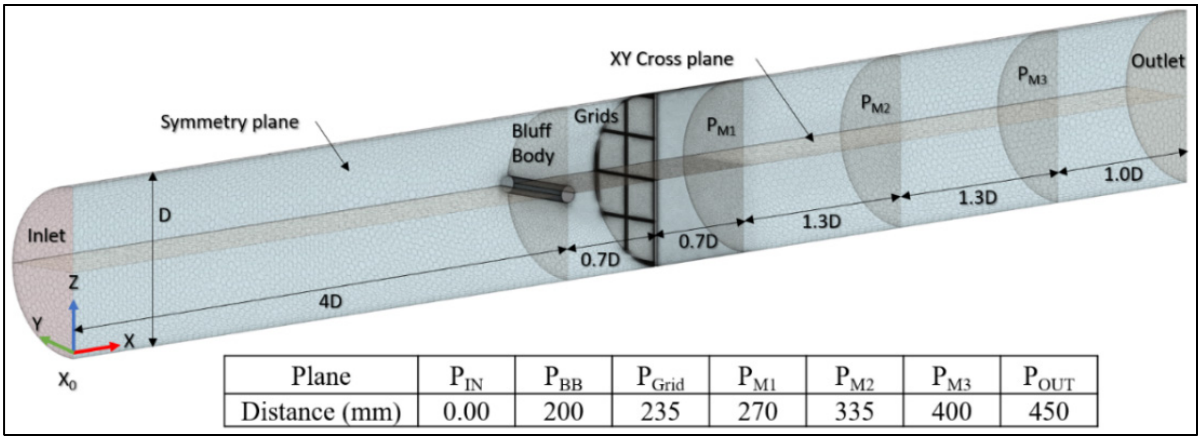

Plane	P_{IN}	P_{BB}	P_{Grid}	P_{M1}	P_{M2}	P_{M3}	P_{OUT}
Distance (mm)	0.00	200	235	270	335	400	450

Figure 3-1 Computational domain

3.5.3 Numerical Parameters

The unsteady RANS simulations in the present study are performed in Star-CCM+ (v2206) using the Realizable 2-layers K-ε turbulence model and the implicit unsteady solver. Pressure-Velocity coupling is achieved using the SIMPLE algorithm to control the overall simulation. The timestep is equal to 10% of the shedding period (f=400 Hz, Ts = 2.5E-4 s) and the second-order scheme is used for temporal discretization. The default coefficients and relaxation factors were kept. The shedding cycle fully develops over the first 0.1s and the stop criterion is 0.2 s, which is sufficient for multiple fully-developed vortices to shed and interact with the grid. The fluid is modeled as constant-density standard air (T=20°C, P=101.3 kPa). Compressibility effects are neglected because the Mach number is far below 0.3. The inlet is modeled as a velocity inlet and the outlet as a pressure outlet. The inlet velocity is fixed to 10 m/s (Re_{BB} = 3 200, Re_{Pipe} = 32 000). The walls (wall, bluff body, and grids) are modeled as no-slip boundary condition. The wall treatment uses the 2-layer all-Y+ method, with a minimum distance of 0.001 mm.

Force sensors are added to the bluff body and the grids to monitor the lift and drag acting on them. In addition, surface-averaging planes and grids of points, located on the virtual planes (Figure 3-1: P_{M1}, P_{M2}, P_{M3}, and XY cross plane), monitor the total pressure, TKE, velocity and vorticity. The surface-averaging planes record the mean intensity, standard deviation, and uniformity.

3.5.4 Mesh Design

The mesh, shown in Figure 3-2, is generated using the polyhedral mesher with three optimization cycles. The global cell size is 5% of tunnel diameter (D) and the core region of interest is refined to $0.02D$ (1.0 mm). The refinement zone starts $4d$ (20.0 mm) upstream of the bluff body and extends to P_{M2}. It spans the entire width of the cylinder and +/- $2d$ radially (+/-10.0 mm). The surface size of the bluff body is $0.05d$ (0.1 mm) with a max cell size of $0.1d$ (0.5 mm) in its wake, defined by a tapered region spanning the width of the cylinder and extending up to the grids. The surface size of the wires is 0.065 mm (ensuring at least 8 points on the circular perimeter of the smallest grid) and a max cell size of $0.1d$ (0.5 mm) in the wake, defined by a tapered region spanning the width of the cylinder and extending up to P_{M2}. The wall mesh merges with the global mesh over six prism layers at a growth rate of 1.3. The Y+ for the bluff body and grids is less than 0.5, and the Y+ for the pipe is less than 1.5 in the region of interest. To resolve the viscous sublayer, a Y+ close to 1 is desirable [26]. The mesh parameters were selected following a convergence study presented in ANNEXE I.

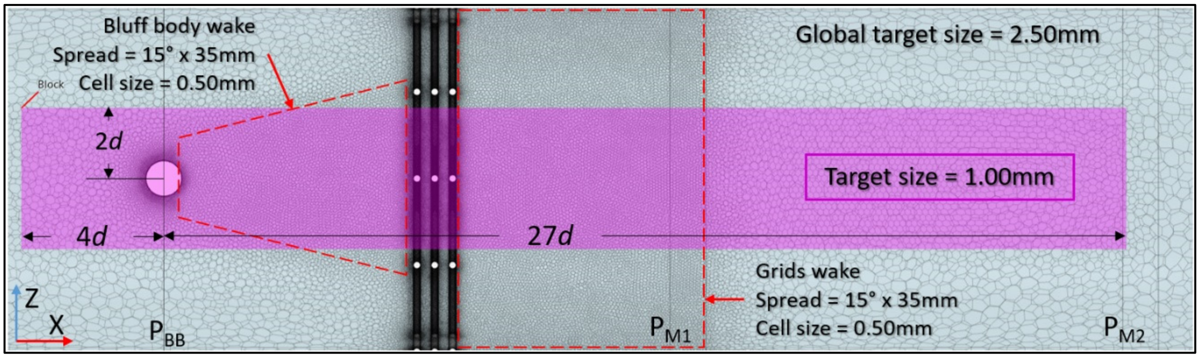

Figure 3-2 Mesh and refinement zones

3.5.5 Design of Experiment

The design of experiment (DoE) is planned to understand how the grid wire diameter (d_w), the grid porosity (φ) and the intergrid spacing (ε) influence vortex breakdown. Porosity describes the void ratio of a structure. When looking at grid from the front, the porosity is given by $\frac{a \cdot b}{A \cdot B}$, where $a \cdot b$ is the open area and $A \cdot B$ is the total cell area. Figure 3-3 presents the grid variables. The grids used in this study have a square opening, hence $A = B$. Note that $A = a + d_w$.

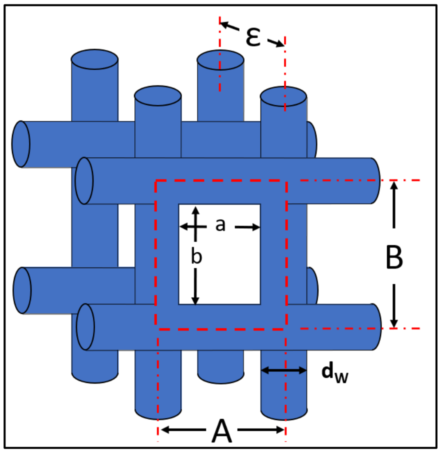

Figure 3-3 Grid Parameters

Three different wire sizes (0.25, 0.50 and 1.00 mm) and three nominal porosities (55, 70 and 85%) are tested. In addition to single grid configurations, stacks composed of three grids are considered with an intergrid spacing (*ε)* equal to 0.5x, 1.0x and 1.5x the bluff body diameter (2.5, 5.0 and 7.5 mm).

The lower limit for the wire diameter (d_w) is 0.25 mm because results from previous authors [14, 15] showed that a finer grid would likely be ineffective. The upper limit for the d_w is 1.00 mm, as it needs to be relatively small compared to the vortex-seeding bluff body diameter, so as to not generate its own large vortices downstream. Since the overarching goal is to develop a solution causing a lower pressure loss than metallic foam, the low end of the porosity range is set to φ=55%. The upper end of the porosity range is set to φ=85%, to ensure the grid opening (dimensions *a* and *b* in Figure 3-3) remains below 2.5*d*. The lower bound of the intergrid spacing (ε) needs to be sufficiently large to avoid creating channels between the grids. The upper bound of the intergrid spacing ensures that the thickness of a stack of 5x 1.00 mm grids will not exceed 25 mm (design-bound).

The nomenclature adopted for the individual setups describes the nominal wire diameter and the nominal grid porosity e.g., D025P55 identifies a single grid with a wire diameter of 0.25 mm and a porosity of 55%. For configurations with multiple grids, a suffix describes the number of grids and the intergrid spacing (ε), hence D100P85-3x2.5 corresponds to a stack of three grids with a wire diameter of 1.00 mm, a porosity of 85% and the intergrid spacing of 2.5 mm. Table 3.2 presents the grids tested, where *a* is the width of a grid opening. Note that the baseline configuration refers to the case without any grids i.e., only the tunnel and the bluff body.

Table 3.2 List of individual grids used in this study

Grid	d_w [mm]	a [mm]	φ [%]
D025P55	0.25	0.71	54
D025P70		1.30	70
D025P85		3.30	86
D050P55	0.50	1.40	53
D050P70		2.59	69
D050P85		5.69	83
D100P55	1.00	3.08	55
D100P70		7.17	74
D100P85		11.25	81

The effect of the grid alignment is also investigated, as shown in Figure 3-4. The intent behind the misaligned arrangements is to increase the blockage area in a similar manner as would a lattice structure. For the offset grid configurations, the second grid is rotated 45° and the third grid is shifted up and right by *a*/2.

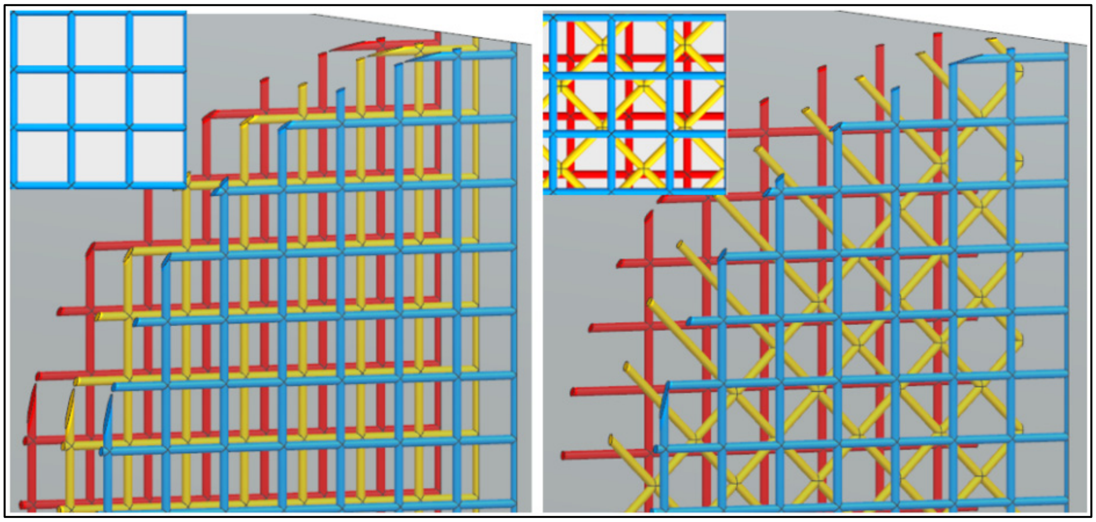

Figure 3-4 Grid alignment. Left: Inline grids, Right: Offset grids. The inset in the top-left corner shows the apparent porosity

3.5.6 Key Performance Indicators

3.5.6.1 Pressure Drop

The pressure drop (ΔP) is an important metric to evaluate the efficiency of the different structures. It corresponds to the difference in pressure between a reference point and a second one located downstream. In an ideal system, the pressure at the inlet and the outlet would be the same. However, the grids create a restriction to the passage of the fluid, which results in a pressure loss. In order to maximise the overall efficiency of the engines, it is desirable to minimize the pressure drop. In this case, the pressure drop is measured between the inlet and outlet of the CFD domain (Figure 3-1) using surface-averaging planes. To isolate the effect of the grids, the baseline ΔP (caused by the tunnel and the bluff body, Eq. (3-1) is subtracted from the total ΔP measured (Eq. (3-2)). The results for the pressure drop are averaged over 40 shedding cycles, from T=0.1 s (when the shedding is fully developed) to T=0.2 s (when the simulation stops).

$$\Delta P_{baseline} = P_{outlet} - P_{inlet}\ (without\ any\ grids) \tag{3-1}$$

$$\Delta P_{grid} = (P_{outlet} - P_{inlet}) - \Delta P_{baseline} \tag{3-2}$$

3.5.6.2 Turbulent Kinetic Energy

In combustions systems, turbulence is generally a good thing because it increases the mixing rate of the fuel with the air, which results in a faster flame speed and more power [1]. A common metric to assess the turbulence level of a flow is the turbulent kinetic energy (TKE) which represents the kinetic energy per unit of mass carried by the fluctuations. The instantaneous TKE from the turbulence model is spatially-averaged using a surface-averaging monitor located on the plane P_{M2}. The results are then time-averaged over 40 shedding cycles, from T=0.1 s to T=0.2 s. For clarity, the results are presented as a reduction of TKE relative to the baseline (configuration without the grids), and are calculated by Eq. (3-3)

$$Relative\ TKE\ Reduction = \frac{TKE_{Grid} - TKE_{Baseline}}{TKE_{Baseline}} \tag{3-3}$$

3.5.6.3 Flow Velocity Uniformity

In the scope of delivering air to the combustor, it is highly desirable for the velocity to be as homogenous as possible to ensure the air-fuel ratio is uniform within the flow. The presence of high/low velocity streaks can result in rich or lean pockets which opens the door to a plethora of combustion issues such as auto-ignition, noise and high NOx emissions [1]. This homogeneity can be quantified by calculating the flow uniformity (θ), which is a ratio of the sum of local velocity deviations relative to the mean velocity. It is calculated by Eq. (3-4), where U_i is the instantaneous local velocity at a given point, $\overline{U}$ is the surface-averaged velocity and n is the number of points sampled [27]. For an ideal flow without any deviation, $\theta = 1$.

$$\theta = 1 - \frac{\sum|U_i - \overline{U}|}{n|\overline{U}|} \tag{3-4}$$

The local velocities are sampled on an array of points located on plane P_{M1} with a resolution of 50x10pts. An exclusion filter is applied to remove the points which lie within 2mm of the tunnel wall to avoid the boundary layer effects. The results for the flow velocity uniformity are averaged over 40 shedding cycles, from T=0.1 s (when the shedding is fully developed) to T=0.2 s (when the simulation stops).

Note that the flow upstream of the grids follows an M-shape profile, due to the blockage created by the bluff body. Since the fluid is incompressible, the fluid must accelerate around the bluff body, resulting in a maximum velocity higher than the nominal speed. This profile is consistent with the results from Ong & Wallace [28]. As a result, the flow field uniformity upstream of the grids is around 90%.

3.5.6.4 Transmitted Vortex Size

The last KPI is the transmitted vortex size (TVS), which is estimated by visualizing the eddies with an isosurface of the Q-criterion (Q=5000 s^{-2}). The vorticity for i (around the x-axis) is overlayed on the isosurface. For clarity, the visible region is bound between the 20 s^{-1} and 300 s^{-1}.

The Q-criterion is commonly used to identify and visualize vortical structures in CFD. By defining an iso-surface as a function of the Q-criterion, one can quickly “adjust” the detection threshold of the vortices. Selecting the correct Q-criterion value comes down to which structure is of interest. In this case, Q=5000 s^{-2} is adequate because it is sufficiently sensitive to identify the TVS up to the second plane of measurement (PM2 in Figure 3-1), without capturing the smaller, secondary vortices. The main caveat of this method is that it does not capture the energy of the vortex. However, the authors believe that using the Q-criterion is a valid method for a comparative study like this one, since the iso-surface is defined with the same threshold, and the mesh cell sizes are the same for all the simulations.

The estimation of the size of vortical structures was simplified by measuring their cross-section at the symmetry plane. By the time the transmitted vortices reach P_{M2}, they are strongly coherent structures and perpendicular to the flow direction, as evidenced in the next figure. Their cross-section is therefore a meaningful characteristic dimension. The size of the vortices is manually measured using an image processing software. The pixel/mm ratio is calculated by measuring the diameter of the tube which is a known dimension. Because the vortices are more ellipsoid than circular, the length of the minor and major axis are measured, and the area is calculated. The diameter of the vortex is then calculated from the ellipse area. This is a simplification to facilitate the comparison between the cases. The vortices are measured at a distance of 2.25*D* (115 mm) downstream of the last grid, under the same meshing conditions, to keep the diffusion length similar between the cases. Figure 3-5 shows the transmitted vortices for the baseline (top) and D100P55-3x5.0 (bottom) configurations. The results are measured for a single timestamp between T=0.19-0.20 s, when the trailing edge of the vortex lines up with $P_{M2'}$.

The shedding is periodic, and the breakdown and reformation patterns of the vortices are very similar over time. The vortex size was initially measured systematically for every timestep where the vortex intersected P_{M2} between t=0.175 s and t=0.200 s, for a total of 11 points per series. It was quickly determined that the variation in the vortex size was negligible (+/-3%). The authors therefore concluded that it is acceptable to measure the vortex size for a single instant.

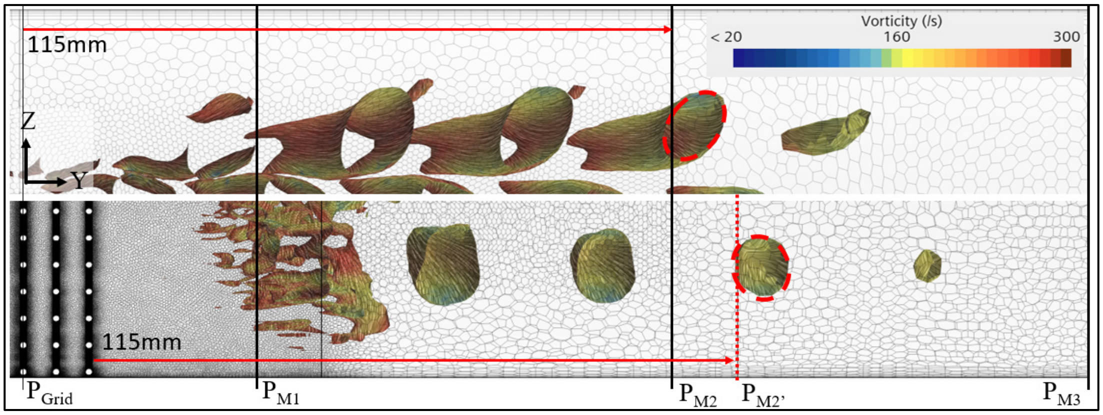

Figure 3-5 Isosurface of the Q-Criterion showing the vorticity. Top: Baseline, Bottom: D100P55-3x5.0

3.6 Results

The simulations described in Table 3.1 are performed and analyzed systematically using the four KPIs described in §3.5.6. The results are presented and interpreted in the next section.

3.6.1 Pressure Drop

The variation of the pressure drop, computed with Eq. (3-2), as a function of the intergrid spacing is presented in Figure 3-6 for two porosities (a = 55% and b = 85%). The solid lines correspond to the cases where the grids are inline, the dashed lines correspond to cases where the grids are misaligned (offset). In addition to the three spacings tested (ε=2.5, 5.0 and 7.5 mm), a fourth column (INF) is added, which extrapolates the results if the three grids were infinitely separated by multiplying the pressure drop from the individual grid cases by three.

Looking at Figure 3-6, three things stand out. First, porosity has a massive effect on the pressure drop. For a given wire size, increasing the porosity from 55% to 85% leads to a 7-10x reduction of the pressure drop. The effect of the porosity is straightforward; a more porous structure creates less blockage, which results in lower losses. Second, for a given porosity, increasing the wire diameter seems to help minimize the pressure losses and this trend is amplified when the intergrid spacing is narrow. When ε=2.5 mm, the pressure drop for the largest grids (D100, green) is about half that of the smallest grids (D025, blue). This is likely because the smaller grids have more wires in the flow, which increases the amount of interaction with the flow. For reference, D025P55 contains 54 struts vs. 16 struts for D100P55. Third, as the space between the grids increases, the interaction between them diminishes until it becomes negligeable, eventually acting as independent grids. At this point, the blockage experienced by the air is solely function of the blockage area of the individual screens. Notice that when the grids are aligned (solid lines), a lower ΔP is achieved by decreasing ε, but the effect of the intergrid spacing reverses with the offset grid alignment such that when the grids are offsetted (dashed lines), a lower ΔP is achieved by increasing ε.

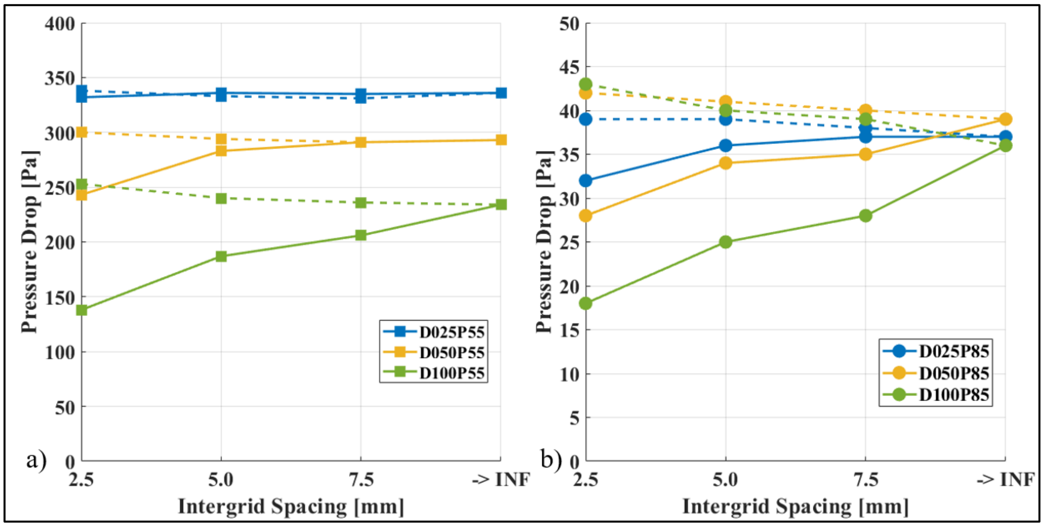

Figure 3-6 ΔP evolution vs. intergrid spacing. a) φ =55%, b) φ =85%. Solid lines = inline, dashed lines = offset configurations

Figure 3-7 to Figure 3-9 show the instantaneous total pressure at the symmetry plane for different grid configurations, exposing the effect of the grid wire diameter and intergrid spacing on the wake generated, which helps explain the results.

The decrease in the total pressure is clearly visible in the wake formed behind each wire. When the screens are aligned, reducing ε allows the wake of the first grid to extend to the next one (Figure 3-7a), maximising the drafting effect which leads to a lower pressure drop. The same principle is often observed in sports such as cycling, where athletes follow each other very closely to benefit from the slipstream. As the gap increases, the strength of wake diminishes (Figure 3-7b) and the pressure field downstream becomes more uniform. When ε

is large, the interaction between the grids is negligible and the effect of each grid is independent from those upstream.

When the grids are misaligned, this slipstream effect does not come into action because the grids downstream do not nest in the wake formed by the ones upstream, no mater how close they are. In addition, randomly arranging the grids increases the visible blockage area as the screens downstream come into view, which effectively reduces the apparent porosity of the stacks. With the offset configuration, reducing ε causes the ΔP to increase because the flow must not only bypass the grids, but is also forced to interact with the wake created by those upstream (Figure 3-7c). On the other hand, increasing ε diminishes the interaction between the grids until they become independent, at which point the grid arrangement becomes irrelevant (Figure 3-7d).

Because the size of the wake varies with the wire diameter, the effect of the spacing is intimately related to the screen size. The porosity also has an effect on the wake. Looking at Figure 3-8, the wires are so close to one another that the low-pressure regions they create coalesce all together before reaching the next grid, even in the most compact configuration. This explains why neither the grid alignment nor the intergrid spacing had a meaningful impact on the pressure loss for the D025P55 cases in Figure 3-6a.

Increasing the porosity creates larger gaps between the wires, which allow the wakes to form independently. The pressure distribution between Figure 3-8 and Figure 3-9 is noticeably different, especially when the grids are misaligned, which explains the results for the D025P85 cases in Figure 3-6b.

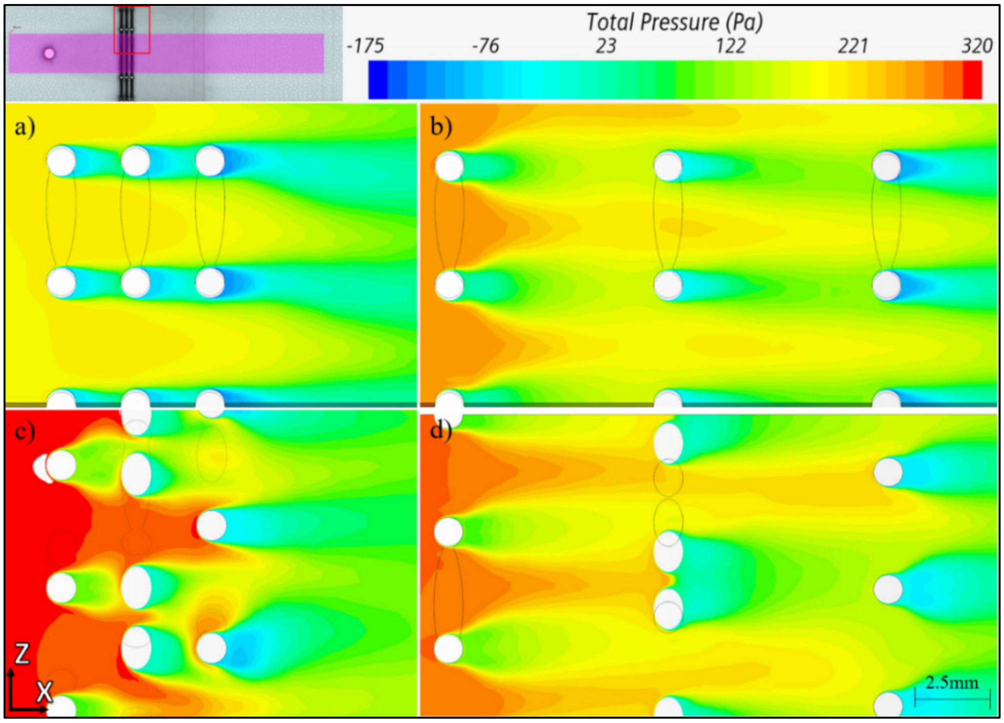

Figure 3-7 Instantaneous total pressure field at the symmetry plane for:
a) D100P55-3x2.5 inline, b) D100P55-3x7.5 inline, c) D100P55-3x2.5 offset, d) D100P55-3x7.5 offset

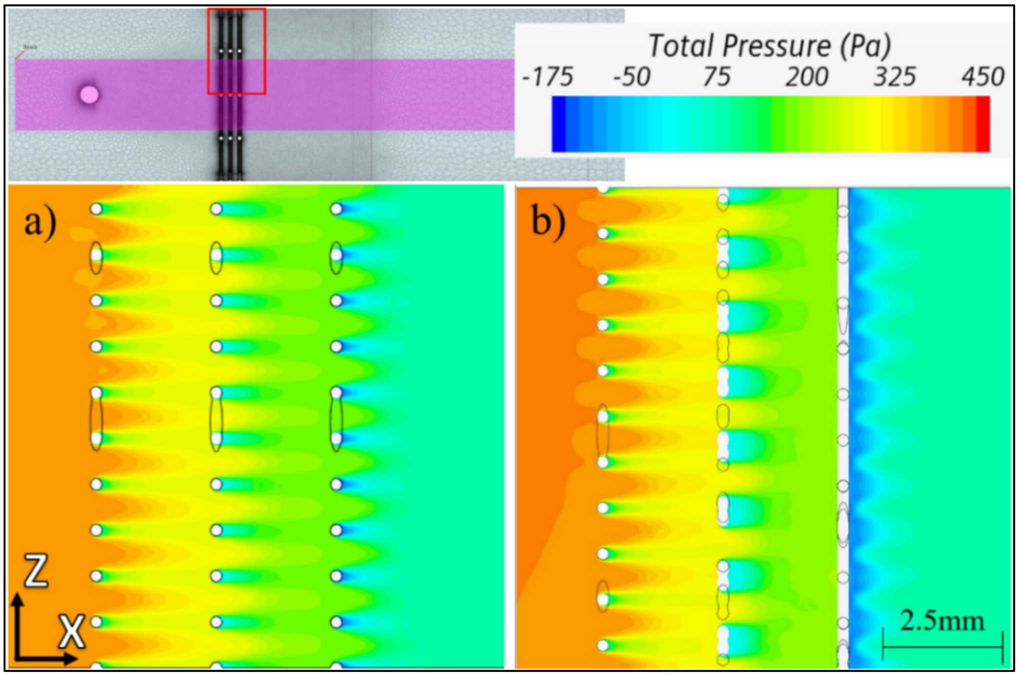

Figure 3-8 Instantaneous total pressure field at the symmetry plane for D025P55-3x2.5. a) aligned grids, b) offset grids

It is worth noting that the offset grid configurations yield a more uniform total pressure field downstream due to the interactions phasing out. This is particularly visible in Figure 3-9, where the regular grid placement (left) causes the wakes to deepen rather than to diffuse. The same observations can be made for the compact configurations in Figure 3-7a & c. However, increasing ε dampens this homogenizing effect since it reduces the interaction level between the grids (Figure 3-7b & d).

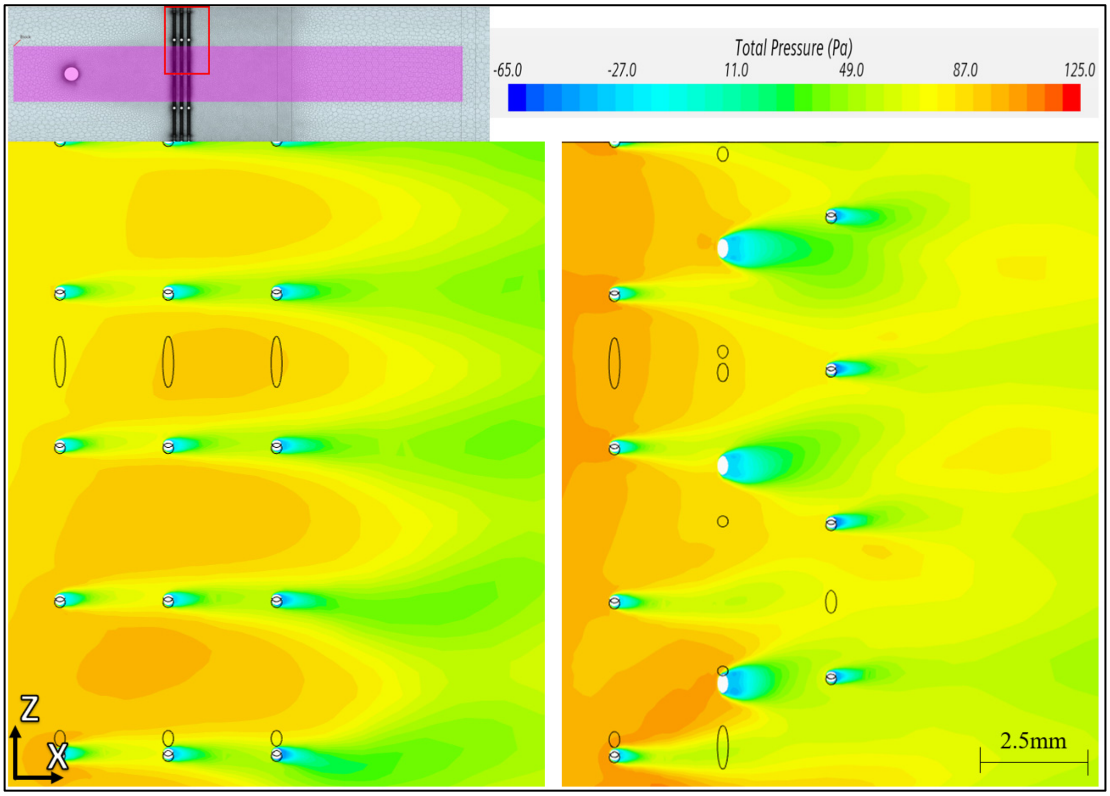

Figure 3-9 Instantaneous total pressure field at the symmetry plane for D025P85-3x2.5. a) aligned grids, b) offset grids

3.6.2 Turbulent Kinetic Energy

Figure 3-10 presents the reduction of TKE relative to the baseline (configuration without the grids), calculated by Eq. (3-3) as a function of the intergrid spacing. Note that the first column presents the results for the individual grid configurations. Again, the results are presented for two porosities (a = 55%, b = 85%), and the solid lines correspond to the inline configurations and the dashed lines correspond to the offset configurations.

Looking at Figure 3-10, the first thing that stands out is that the coarser grid configurations (D100-Green) have systematically higher TKE levels than their finer alternatives (D025-Blue and D050-Yellow). Overall, the configurations with a single grid are remarkably effective at damping the turbulences.

When the porosity is low (Figure 3-10a), the introduction of additional grids initially leads to a dip in the TKE reduction, but the smaller grids eventually recover as ε increases. When the porosity is large (Figure 3-10b), the introduction of the additional grids has a negligible effect at first for the finer grids, but eventually leads to a slight improvement as ε increases. On the other hand, increasing ε for the coarser grids always results in a higher TKE level, regardless of the porosity. Another key trend is that the offset grid configurations systematically improving the TKE reduction over the aligned configurations. When porosity is high, the additional grids significantly improve the TKE reduction if they are in the offset configuration, but have a negligible effect if they are inline. Looking at Figure 3-10, the gap between the aligned and offset configurations (solid vs. dashed lines) is significantly larger on the right graph (φ=85%) compared to the left graph (φ=55%), and this effect is amplified by increasing the wire diameter (D025-Blue vs D100-Green).

The effect of the grids on the TKE is perhaps not as straightforward as it was for the pressure drop because two competing mechanisms are at play. The first one is the disruption of the incident vortex by the grids, which reduces the transmitted TKE. This is mostly function of the grid porosity, because the more porous a grid is, the less interaction it has with the vortex, allowing more energy to pass through. This explains why the TKE reduction levels in Figure 3-10a (φ=55%) are noticeably higher than in Figure 3-10b (φ=85%). The second mechanism responsible for the residual TKE is that the grids themselves create turbulence as the fluid flows around the wires, generating secondary Von Karman vortex alleys which contribute to the residual TKE levels measured. This effect is sensitive to the wire diameter since larger wires create larger eddies and is particularly visible in Figure 3-10b, where the three different wire sizes are clearly separated, especially when the grids are aligned.

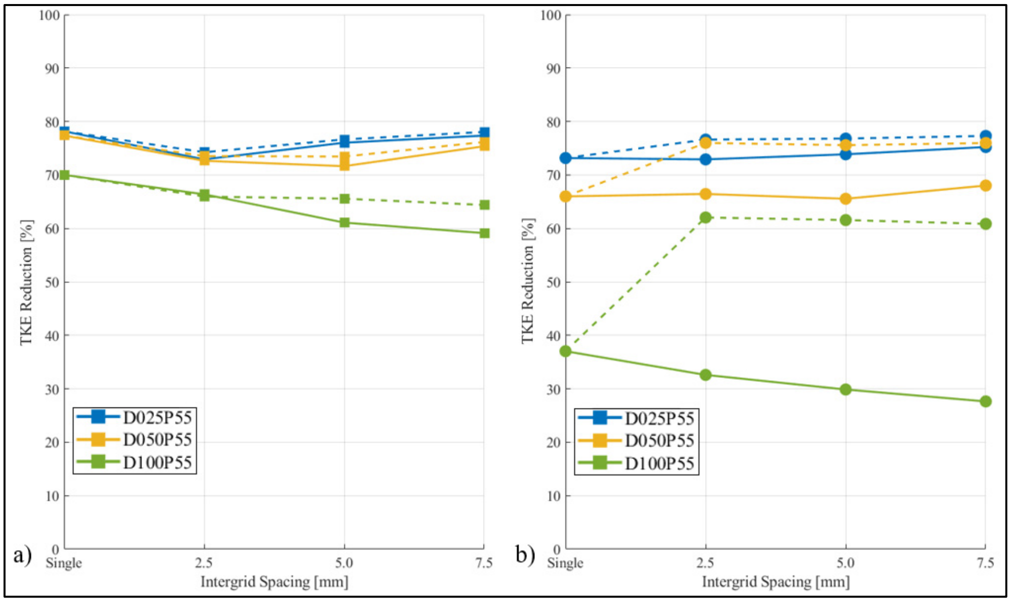

Figure 3-10 TKE reduction vs. intergrid spacing. a) φ =55%, b) φ =85%. Solid lines = inline, dashed lines = offset configurations

Figure 3-11 presents the evolution of the spatially-averaged TKE across the duct section (the symmetry plane) as a function of the axial distance from the inlet for the D025-3x7.5 configurations for two porosities (φ = 55%, purple and 85%, orange). The dashed lines correspond to the offset configurations. The grids introduce a lot of turbulence, especially when the grids are very restrictive, but it quickly decays.

Figure 3-11 highlights three key aspects of the TKE evolution over the axial distance. First, the TKE increases around the 200 mm mark as the air flows around the bluff body, creating the Von Karman street effect. The TKE intensity then plateaus for all the conditions until they reach the grids. Second, as the fluid progresses further downstream, it interacts with the grids. This gives rise to a second increase of turbulent kinetic energy due to the formation of secondary vortices caused by flow around the grids. Because the grids in Figure 3-11 are quite small, the secondary vortices they create are also small and therefore dissipate quickly, which explains the abrupt variations in TKE levels. The more restrictive the grid is, the steeper this effect will be since a less porous grid will have more wires in the flow, which obviously creates more secondary vortices. Since the flow is incompressible, it must accelerate as it passes through the screen openings, which further contributes to the intensity of the secondary vortices. Finally, the incident vortex is distorted as it interacts with the grids. This leads to a dissipation of some of the turbulent energy retained by the transmitted vortex, as evidenced by the progressively lower minima of the TKE past each grid. In contrast, the baseline configuration (without the grids) experiences a slow and steady decay of the TKE.

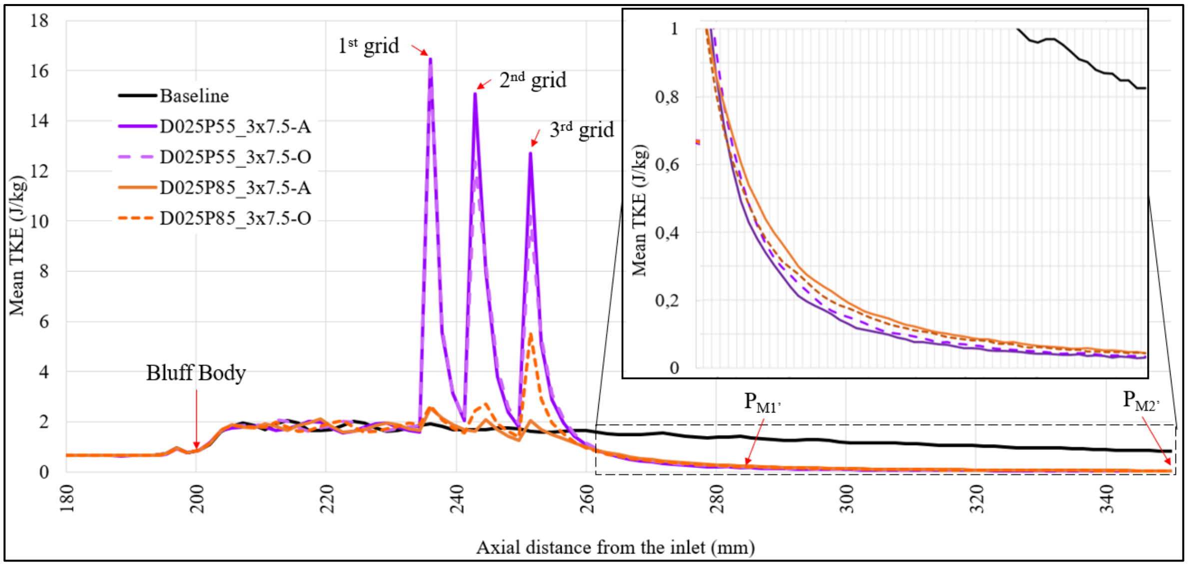

Figure 3-11 Evolution of the average TKE at the symmetry plane as a function of the axial distance for the D025 configurations

Figure 3-12 and Figure 3-13 show the TKE distribution along the tunnel symmetry planes for different grid configurations. On the left side, φ=55% and on the right side, φ=85%. The top row shows the inline configurations while the bottom row shows the offset configurations. The regions where the TKE exceeds 30J/kg are clipped for clarity.

The results for the finest grid (D025, Figure 3-12) are reminiscent of Figure 3-8 and Figure 3-9, with the wakes coalescing together for the low porosity cases, but developing independently when the porosity is large. For the D025P55 cases, the TKE profile is uniform beyond the grids, which indicates the turbulence caused by the incident vortex is completely dissipated and the flow is homogenous. In contrast, the D025P85 cases feature a hump in the middle region, which suggests that at least some of the turbulence from the shedded vortices is transmitted through the most porous stacks. The TKE also extends further downstream.

Overall, the grid alignment appears to have a limited impact on the TKE decay. For the lowest porosity cases (D025P55, Figure 3-12a & c), it is impossible to tell which is inline and which is misaligned, and the difference is marginal for the most porous configurations (D025P85, Figure 3-12b & d). This suggests the first grid does most of the work in terms of breaking down the vortex and dissipating its energy. This is clearly demonstrated in Figure 3-11.

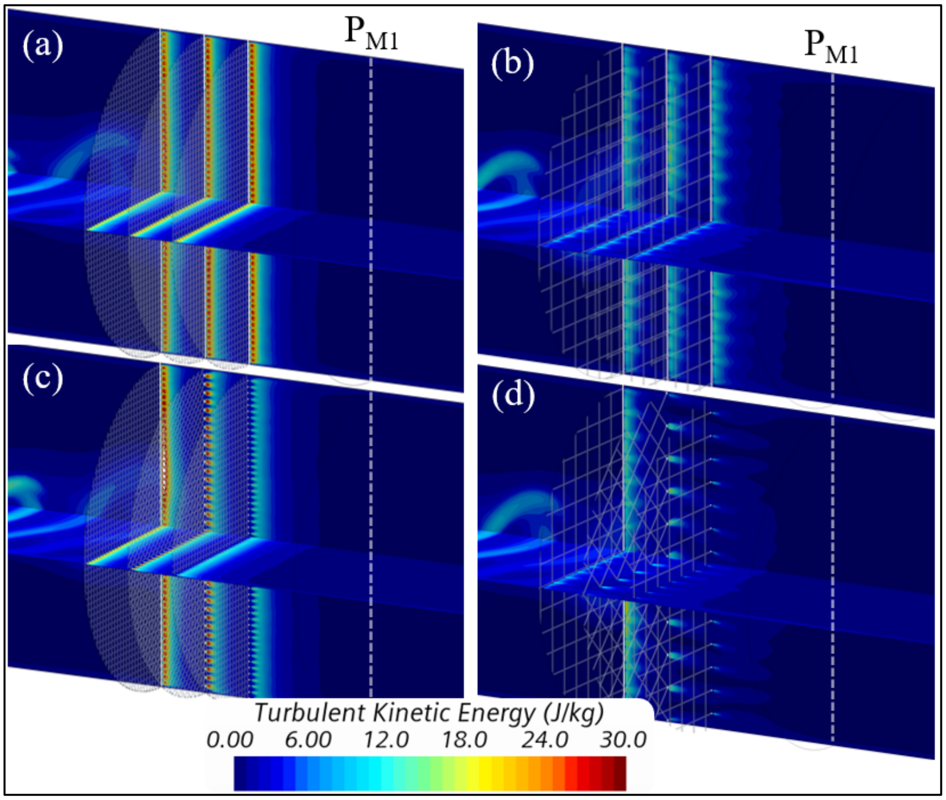

Figure 3-12 TKE Intensity for D025 – 3x7.5 configurations: Top row = Inline, Bottom row = Offset; Left: φ =55%, Right: φ =85% a) D025P55-3x7.5 aligned, b) D025P85-3x7.5 aligned, c) D025P55-3x7.5 offset, d) D025P85-3x7.5 offset

Shifting our attention to the larger mesh wire diameter TKE maps shown in Figure 3-13, two things stand out. First, the TKE level for the D100P55 cases (a/c) is significantly higher near the grids than it is for its more porous counterpart (b/d). This is a consequence of the blockage created by the grids, which forces the flow to accelerate as it passes through the stacks. Second, the TKE decays much faster when the grids are misaligned, especially when the porosity is large. As explained in the last section, the wake created by the larger wires is wider and extends further downstream. When the grids are aligned, this low-pressure zone extends to the next grid, which confines the flow into channel-like structures. When the grids are misaligned, the flow becomes more chaotic and suffers from greater momentum loss, resulting in a faster TKE decay.

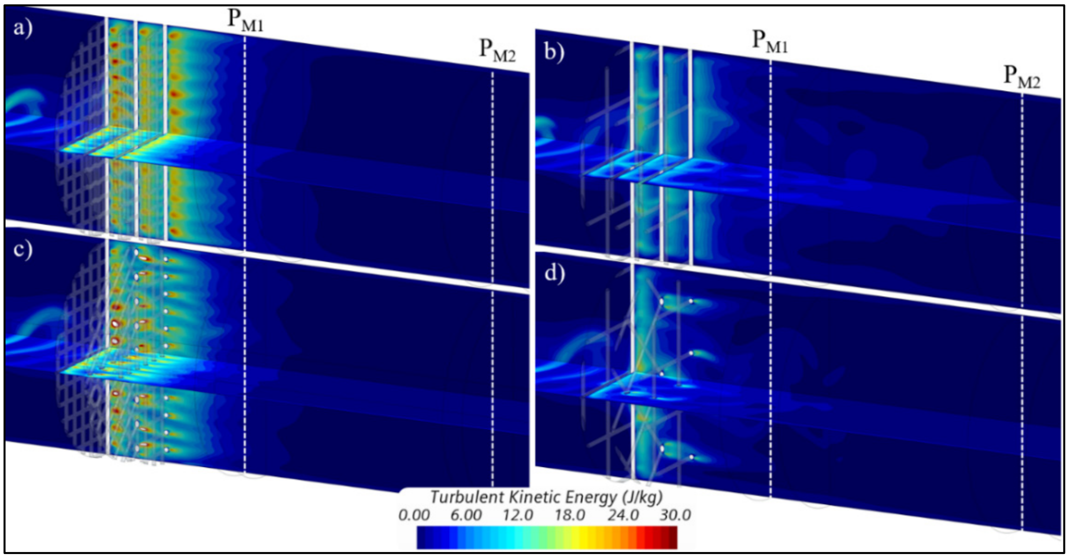

Figure 3-13 TKE Intensity for D100 – 3x7.5 configurations: Top row = Inline, Bottom row = Offset; Left: φ =55%, Right: φ =85% a) D100P55-3x7.5 aligned, b) D100P85-3x7.5 aligned, c) D100P55-3x7.5 offset, d) D100P85-3x7.5 offset

3.6.3 Flow Velocity Uniformity

The evolution of the velocity field uniformity, computed with Eq. (3-4) on P_{M1}, as a function of the intergrid spacing is reported in Figure 3-14. The graphs follow the same convention as Figure 3-10 i.e., figures a) and b) present the results for φ = 55% and 85% respectively, the solid and dashed lines correspond to the inline and offset grid arrangements, and the first column showcases the results for the individual grids. Note that the black horizontal line corresponds to the case without a grid.

Overall, the addition of the grids tends to improve the uniformity of the velocity field, but some trends still emerge. First, the velocity uniformity decreases when multiple grids are installed, compared to the single grid configurations. Increasing the intergrid spacing generally helps recover some of the lost homogeneity when the porosity is low, but does little when the porosity is large, except for the coarsest grids. Next, the misaligned configurations help homogenize the flow. Finally, increasing the wire diameter amplifies the effect of the intergrid spacing.

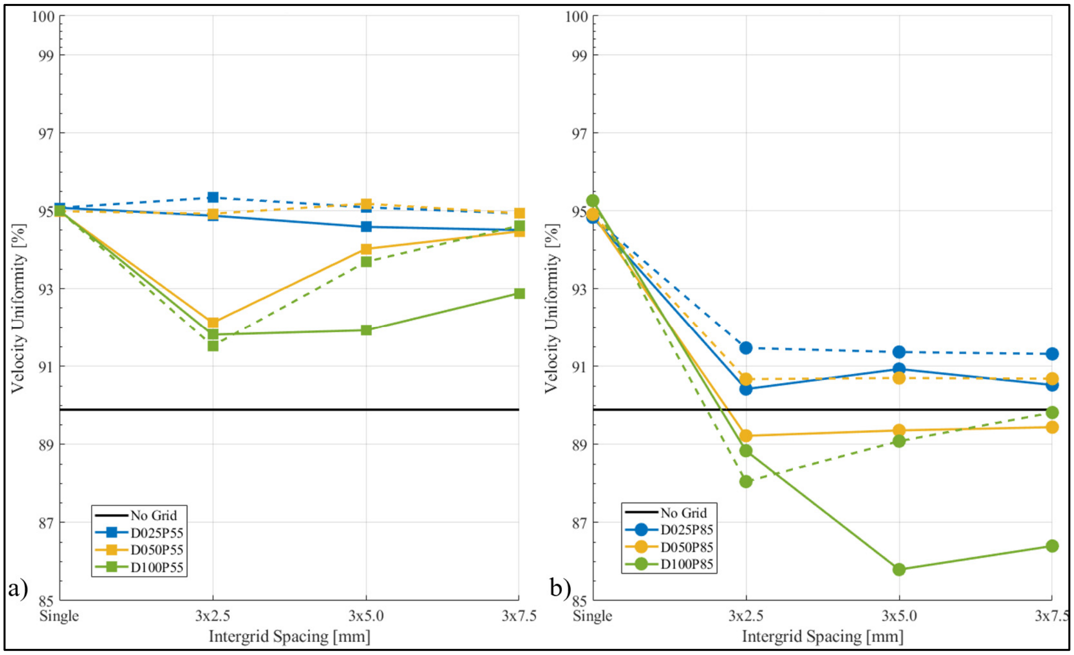

Figure 3-14 Velocity Field Uniformity vs. intergrid spacing. a) φ =55%, b) φ =85%. Solid lines = inline, dashed lines = offset configurations. Horizontal solid line corresponds to baseline (without the grids)

The flow field is more uniform when the porosity of the grids is low and when the wire diameter is small. Increasing the wire diameter leads to stronger wakes, as seen in §3.6.1, which need a longer distance to diffuse.

Figure 3-15 and Figure 3-16 show the velocity magnitude distribution for different grid configurations. The visible range is bounded between 0-16 m/s for clarity.

Looking at Figure 3-15 (D100, *ε*=2.5 mm), the misaligned configurations seem to have a deleterious effect on the flow homogeneity, but increasing the spacing (Figure 3-16, *ε*=7.5 mm) seems to reverse the effect of the grid alignment. When the coarser grids are aligned, they create channels which confine and accelerate the flow, and that effect is amplified by the larger intergrid spacing. On the other hand, arranging the grids randomly increases the tortuosity which promotes mixing. When the intergrid spacing is small, the change in direction can be quite sharp, leading to local pockets of high-velocity intensity. Increasing the gap allows the flow to diffuse, leading to a more uniform distribution. This was also observed in Figure 3-9, where the offsetted configurations resulted in more uniform pressure fields.

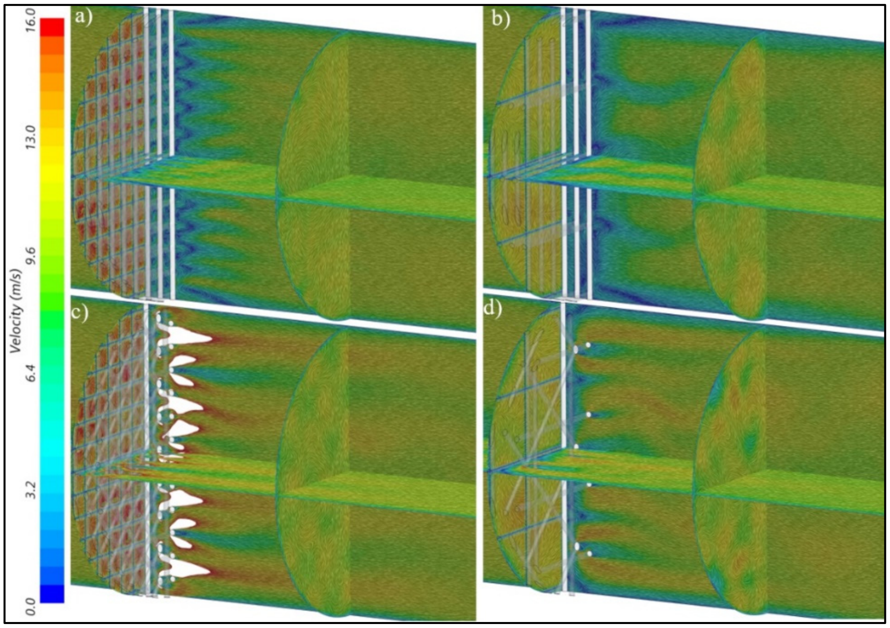

Figure 3-15 Flow field for D100, Left: φ =55%, Right: φ =85%, Top row: Inline, Bottom row: Offset. a) D0100P55-3x2.5 aligned, b) D100P85-3x2.5 aligned, c) D100P55-3x2.5 offset, d) D100P85-3x2.5 offset

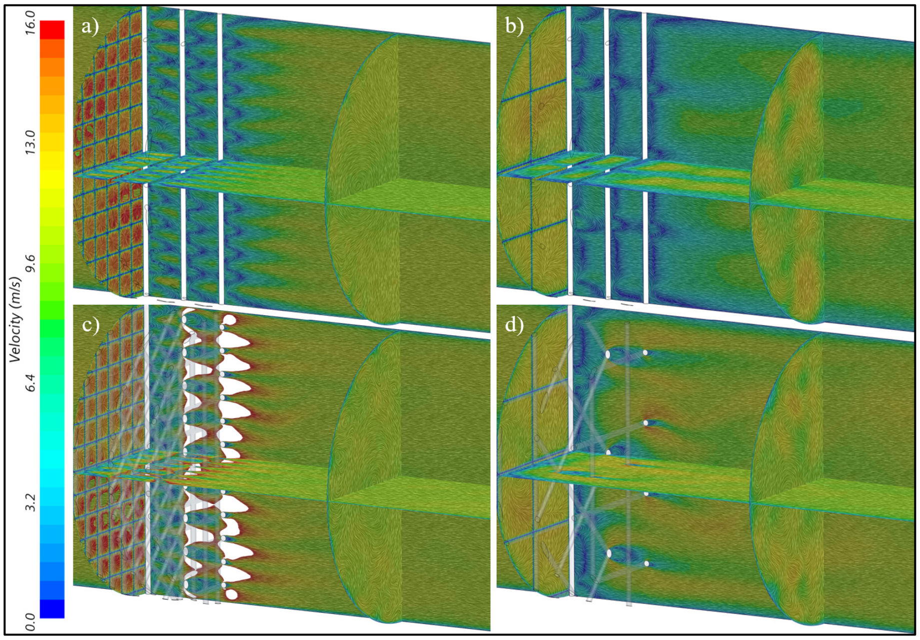

Figure 3-16 Flow field for D100, Left: φ =55%, Right: φ =85%, Top row: Inline, Bottom row: Offset. a) D0100P55-3x7.5 aligned, b) D100P85-3x7.5 aligned, c) D100P55-3x7.5 offset, d) D100P85-3x7.5 offset.

3.6.4 Transmitted Vortex Size

The evolution of the transmitted vortex size (TVS) as a function of the intergrid spacing is reported in Figure 3-17. Again, plots a) and b) present the results for φ = 55% and 85% respectively, the solid and dashed lines correspond to the inline and offset grid arrangements, and the first column showcases the results for the individual grids.

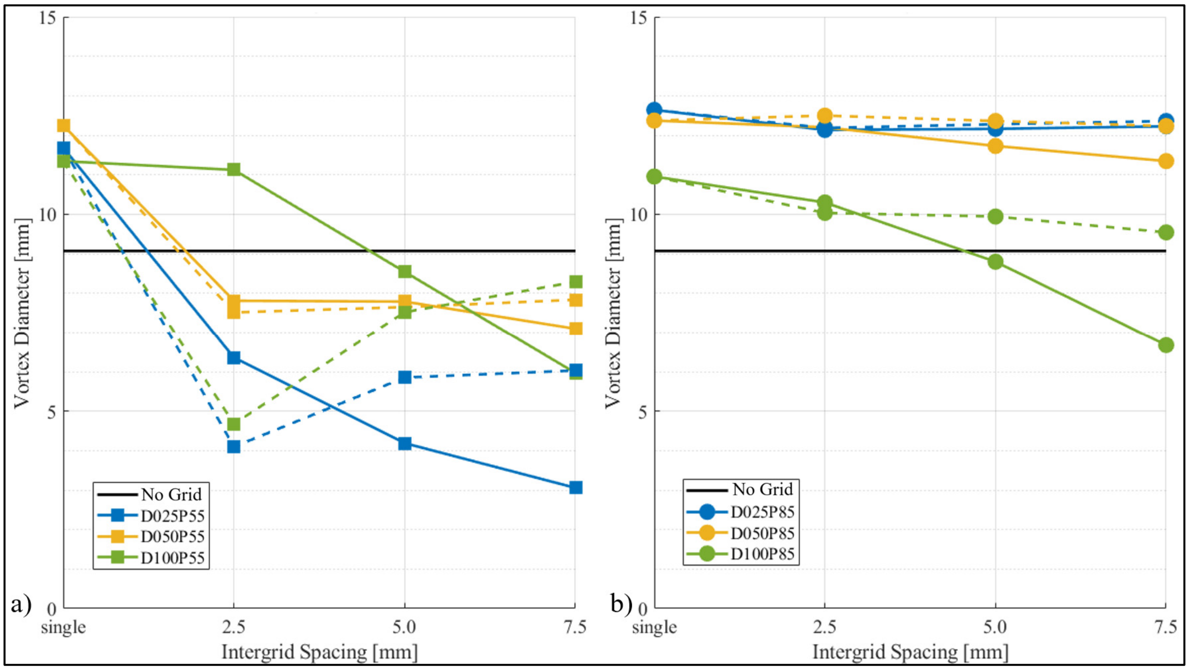

Figure 3-17 Transmitted vortex size vs. intergrid spacing. a) φ =55%, b) φ =85%. Solid lines = inline, dashed lines = offset configurations. Horizontal solid line corresponds to baseline (without the grids)

Placing a single grid in the flow systematically leads to a transmitted vortex larger than the baseline condition, but adding inline grids helps to reduce the TVS. This trend is amplified by increasing the intergrid spacing. When the porosity is large, the additional grids have a minor effect on the transmitted vortex size, especially when the grids are offset. A larger reduction of the vortex size is visible when the grids are inline, and the effect is amplified by increasing the wire diameter and the intergrid spacing. When the porosity is low, placing additional grids leads to a significant reduction of the transmitted vortex size. If the grids are inline, the size of the transmitted vortex decreases as the intergrid spacing increases, but the effect is opposite if the grid are misaligned, with the maximum attenuation happening when the grids are at their closest.

When the incident vortex passes through a grid, it gets chopped into substructures. In the case of a single grid, these vortical substructures do not experience significant distortion and can quickly reform into a coherent structure further downstream. Both Hrynuk *et al.* [14, 15] and Musta & Kruger [17, 18] noted these intermediate vortices tend to diffuse radially outward. When these substructures reform, the resulting vortex is larger than it was initially.

When the incident vortex passes through a stack of grids, the vortical substructures can be exposed to a greater level of distortion, especially when the porosity is low and/or when the wire diameter is large. Partial reformation and annihilation of the transmitted vortex due to severe distortion was observed by Hrynuk *et al.* and Musta & Kruger [14, 15, 17, 18].

3.7 Case Study

To design optimal grid stackings, a design of experiment was developed to understand how the fundamental design parameters affect the vortex-breakdown performance of a regular lattice structure. The investigation was simplified by stacking individual planar regular grids in series and varying their diameter, porosity, spacing and alignment.

Four key performance indicators are monitored to assess the performance of the structures: the pressure drop, the residual TKE, the flow uniformity and the transmitted vortex size. The knowledge gained through this systemic approach presented in section 3.6 will provide clues to guide the design process.

The first step is to rearrange the results in a series of influence maps where the KPIs are plotted against the wire diameter and porosity for the different grid spacing configurations. Figure 3-18 shows an example for the vortex size.

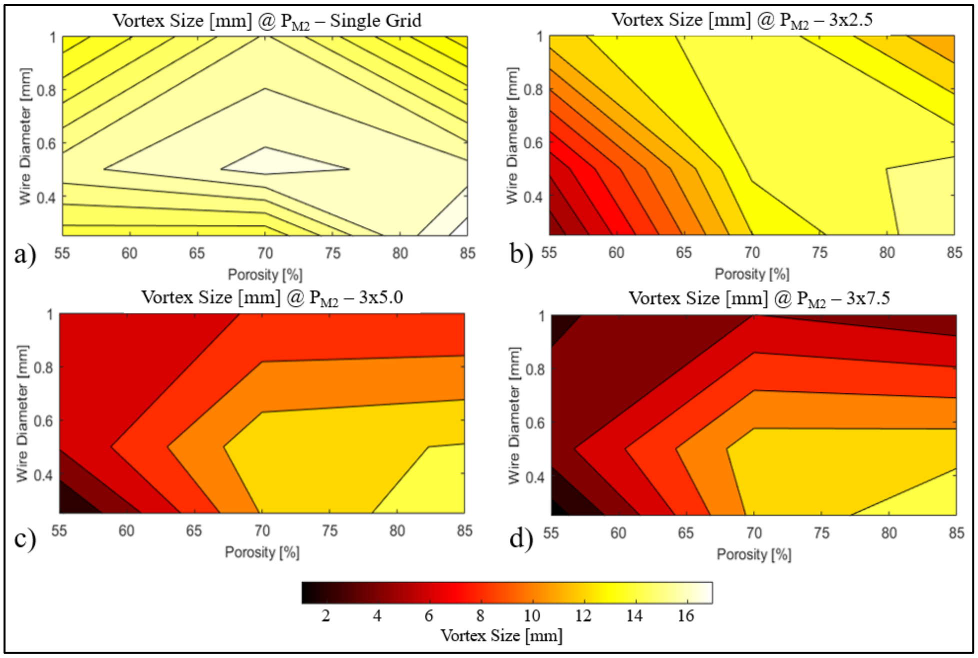

Figure 3-18 Influence maps of the transmitted vortex size for different grid configurations. a) Single Grid, b) ε= 2.5mm, c) ε=5.0mm, d) ε=7.5mm

The next step is to define the target for each KPI. Then, the regions of interest (ROI) are delimited for each KPI, and the resulting polygons are overlayed. The common area of the ROIs defines the confined design space. Figure 3-19 presents an example. The targets for the KPIs were arbitrarily defined as follows: pressure drop shall be below 150 Pa, residual TKE intensity shall be above 0.4 J/kg, velocity uniformity shall be above 90% and transmitted vortex size shall be below 6.0 mm. The resulting design space for optimization, shown in the hatched zone in Figure 3-19, suggests the porosity should be between 62-75% and the wire diameter should be between 0.8-1.0 mm.

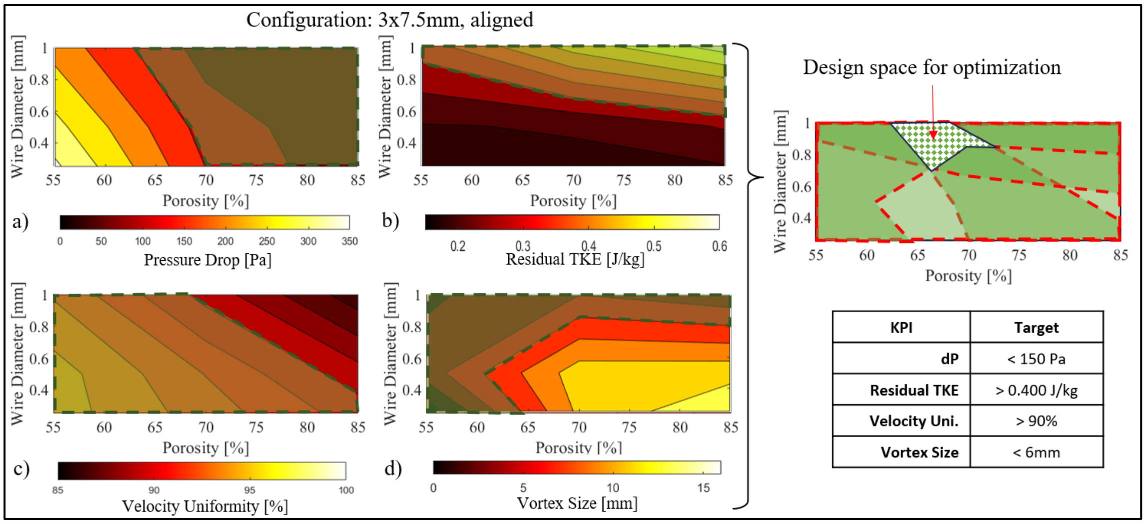

KPI	Target
dP	< 150 Pa
Residual TKE	> 0.400 J/kg
Velocity Uni.	> 90%
Vortex Size	< 6mm

Figure 3-19 Left: Influence maps for a) pressure drop, b) residual TKE, c) velocity uniformity, d) transmitted vortex size. Right: Corresponding design space for optimization

Balancing these requirements (trade-offs) necessitates a good understanding of the objectives of a specific application. In the use-case example presented in Figure 3-19, the main requirement is to limit the size of the transmitted vortex to 6.0 mm. Since this is a functional requirement, any solution that fails this target must be disregarded. Looking only at Figure 3-17, the ideal solution would be D025P55-3x7.5-Inline. This option also maximizes the flow field uniformity and the TKE reduction. However, this configuration is also the most restrictive one, causing the biggest pressure drop. The alternative would be D100P55-3x2.5-Offset, which causes a much lower pressure drop, but allows slightly larger TVS to pass through and is not as effective to homogenize the flow field or reduce the transmitted TKE.

Another limitation is that the maximum thickness of the grid stack may be restricted by the engine design. Such a constrain could limit the number of grids that can be integrated in the stack, or limit the intergrid spacing. In this situation, the preferable solution would likely be to maximise the intergrid spacing even if it means sacrificing a grid, because each additional grid significantly increases the pressure drop, but does not really improve the TKE reduction or flow field uniformity. On the other hand, increasing the intergrid spacing is shown to maximise the vortex-breakdown effect of the individual grids. Ultimately, the multi-criterion optimization process necessitates a weighted function.

3.8 Reformation behavior

Understanding how the vortices reform beyond the grids can also provide some valuable insight. Three different reformation modes are identified and presented in Figure 3-20, again using an isosurface of the Q-criterion (Q=5000 s^{-2}) colored with the vorticity around the x-axis. To enhance the visualisation of the vortex reformation, the visible range is extended between 100 s^{-1} and 2000 s^{-1}, and a different color scale is used.

With the first mode, the incident vortex reforms instantly past the grids (Figure 3-20a). With the second mode, the incident vortex is divided into jet-like structures past the grids before reforming further downstream into a coherent structure (Figure 3-20b). With the third mode, the vortex is split into several chaotic sub-structures (Figure 3-20c). The high level of distortion significantly delays the reformation of the transmitted vortex.

It appears that the reformation mode depends on the size of the openings within the grids i.e., the hydraulic diameter of the grid cell. The first mode (instant reformation) is observed when the grid opening is below 1.5 mm. The second mode (jets) is observed for an opening between 2.0-3.5 mm, while the third mode (chaotic & delayed) happens when the grid opening is larger than 5.0 mm. Note that the behaviour is the same for the grid stacks.

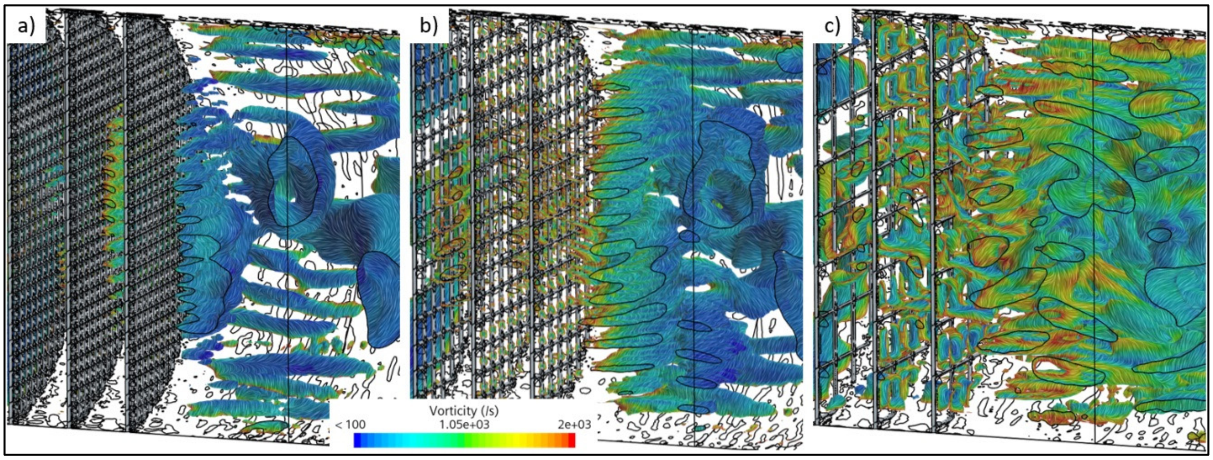

Figure 3-20 Reformation behavior for D050P55-3x7.5 (a), D050P70-3x7.5 (b) and D050P85-3x7.5 (c), using a Q-Criterion = 5000 s^{-2}

Table 3.3 Reformation behaviour of the individual grids

Grid	d_w [mm]	a [mm]	Reformation
D025P55	0.25	0.71	Instantaneous
D025P70		1.30	Instantaneous
D025P85		3.30	Jets
D050P55	0.50	1.40	Instantaneous
D050P70		2.59	Jets
D050P85		5.69	Chaotic, Delayed
D100P55	1.00	3.08	Jets
D100P70		7.17	Chaotic, Delayed
D100P85		11.25	Chaotic, Delayed

The effect of the wire diameter on the vortex transmission and reformation is generally consistent with the results from previous studies [14-16, 20, 21] namely that the smaller grids will chop the vortex but allow it to reform instantly, while the larger grids will significantly distort the vortex, delaying and sometimes preventing its reformation. Additionally, increasing the wire diameter of the grids results in the shedding of secondary vortices.

In their past work, Hrynuk *et al.* [14] also identified different reformation regimes. They initially suggested an “interaction” Reynolds number to explain the regimes, which was based on the wire diameter and factored in the grid porosity to correct the convection velocity. In a subsequent paper [15], they highlighted some issues with this approach and removed the porosity from the equation, suggesting the reformation regimes to be solely function of the wire diameter and convection speed.

While their model appears accurate for a pulsed vortex moving through a stationary fluid, it cannot explain the sensitivity to the grid opening clearly observed in our results. This is likely a consequence of the different approach used to generate the vortices in this experiment, which relies on a moving fluid.

3.9 Conclusions

This paper presented an experimental simulation protocol to systematically study the influence of four core parameters of a grid stack in the optic of developing optimized vortex-breaking porous structures, using a simple incompressible-unsteady RANS model. These parameters are the wire diameter, the porosity, the intergrid spacing and the grid alignment.

Four metrics were identified as key performance indicators to evaluate the effectiveness and efficiency of the structures. These KPIs are the pressure drop, the residual turbulent kinetic energy, the flow field uniformity, and the size of the transmitted vortices. This investigation also proposes an approach to confine the design space in the optic of developing an optimized lattice structure.

The model relies on a Von Karman vortex street created by placing a cylindrical bluff body perpendicular to the flow inside a tunnel. Several grid stack configurations are introduced downstream. The vortex breakdown efficiency of each configuration is systematically evaluated by measuring four KPIs: the pressure drop, the TKE reduction, the velocity uniformity, and the transmitted vortex size.

The size of the grid wires plays a key role. The bigger the wires are, the more distorted the transmitted vortex will be. Larger wires also create bigger wakes which extend further downstream, increasing the effects of subsequent grids. The wire diameter is a key design lever. Increasing the wire size increases the breakdown of the vortical structures, but creates a large wake which results in relatively high TKE levels. Smaller wires are less effective at breaking down vortical structures, but are better at reducing the residual TKE. The influence of placing multiple grids in series varies significantly with the wire diameter of the grids. When the wire diameter is small, the wake produced by the grids is relatively short and does not interact with the grids downstream unless they are extremely close.

For a given TKE reduction target, it is more efficient to reduce the wire diameter of the grids while keeping the porosity high. The same TKE reduction can be achieved for a much lower penalty in terms of pressure drop. Pressure drop increases systematically when additional grids are introduced. However, the effect of the spacing between the grids depends on the grid alignment. When the grids are perfectly aligned, the wake generated by the upstream grids creates a low-pressure zone. The closer the next grids are, the more they can benefit from this drafting effect, resulting in a lower pressure drop. However, if the grids are misaligned, increasing the distance between the grids is favorable to minimize the pressure drop. Finally, decreasing the porosity and the wire size result in higher flow uniformity due to the lower turbulence.

In conclusion, the optimal design should be a graded structure, starting with a very porous grid made from a large wire diameter to breakdown the incoming vortices. Additional grids should be rotated and offset to increase the tortuosity, as it improves the velocity homogeneity. The spacing between the grids should be as large as possible and their numbers must be kept to a minimum to avoid excessive pressure losses. The wire diameter of the final grid depends on the targeted TKE, and should be small if TKE is nefarious, but should remain large if TKE is beneficial to the application. The porosity should only be reduced when the desired velocity uniformity is a concern.

The optimal grid diameter most probably varies with respect to the size of the incident vortices (and by extension the bluff body diameter which controls it). The authors would not want to portray the results as being universal. In future work, varying the size of the bluff body would provide valuable information to better understand how the ratio between the vortex size and wire diameter impacts the grid performance. It would also be valuable to rerun the models at higher Reynolds to extend the results over a more meaningful range of conditions.

CHAPITRE 4

EXPERIMENTAL STUDY

The following presents the different processes and the equipment that will be necessary to measure the efficacy and efficiency of using a stack of grids to dampen vortices. The dimensions of the rig are on the same scale as an industrial aero-derivative combustor.

4.1 Principle

A custom wind tunnel was designed to study vortex breakdown and pressure losses of grid stacks, see Figure 4-1. A high-flow blower motor sucks air into the tunnel. The incoming air first passes through a honeycomb section to homogenize the flow and break down coherent structures at the entrance. The airstream then passes over a cylindrical bluff body, generating a Karman vortex street. As the vortices shed, they encounter the grid stacks and are broken down, smoothing the flow. The air then enters the measuring section and is finally expelled through the blower. The diameter of the tunnel is of similar size to the combustor's region of interest and is sufficiently small for a blower operating on single phase 120V. The 5mm bluff body was selected to create a large vortex without interfering with the walls.

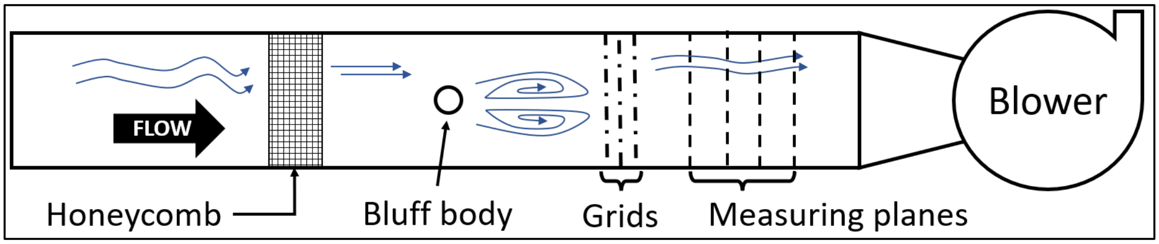

Figure 4-1 Conceptual representation of the wind tunnel

4.2 Test rig

The test rig, shown in Figure 4-2, is composed of a Ø2" x 2' long wind tunnel (1-7) and a motorized gantry (8) for the traverse flow measurements. Both systems are controlled by a LabView program via a single DAQ card (National Instruments SCC-68, not shown).

Air enters the wind tunnel via the inlet bell mouth (1), passes through the inlet tube (2A) and is straightened by a honeycomb section (2B). It then travels through a conditioning section (3) before entering the test section (4) where the air passes over a cylindrical bluff body (4B), creating a Karman vortex street. As the shedded vortices are convected, they encounter the grid stacks (4C). The disturbed air then enters the measuring section (5) where a pitot tube or a hot-wire travelling radially (5C), sealed by a bushing (5B) measures the velocity. The measuring section comprises four equally spaced "stations" to measure the turbulent energy decay as a function of the axial distance. Finally, the air is sucked into the transition section (6) and expelled by the blower motor (7, ATO WB3-1E0-H). The velocity of the blower is controlled by a 1.5-10V input and has a maximum theoretical airflow of 228m^3/h.

Clear 2" I.D. polycarbonate piping was used for the straight ducts (2, 3, 5A). Selective laser sintering (SLS) was used to manufacture the inlet bell mouth (1), the flanges connecting the ducts, the test section elements (4A), the instrumentation ports (5B), and the transition piece (6) using an EOS P110 in PA2200. Additional brackets were made using fused filament fabrication (FFF) on a Markforged X7. The frame is made of aluminum extrusions.

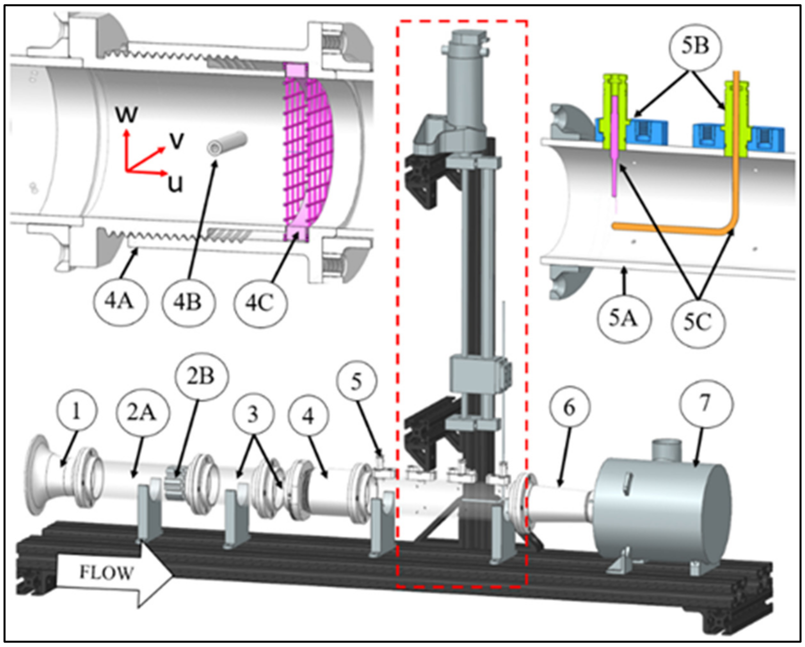

Figure 4-2 Test Rig CAD model

Figure 4-3 presents the position of the different flow elements and measuring planes in the rig. The wind tunnel dimensions are based on the ANSI/AMCA standard 210-16 for laboratory methods of testing fans for certified aerodynamic performance rating, specifically, the setup #16 [29].

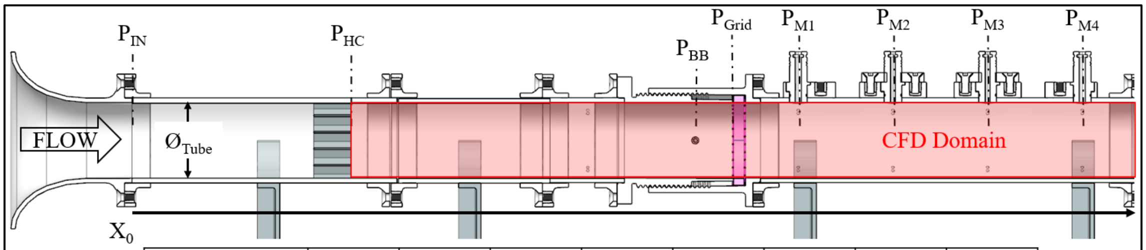

Plane	P_{IN}	P_{HC}	P_{BB}	P_{Grid}	P_{M1}	P_{M2}	P_{M3}	P_{M4}
$X/Ø_{Tube}$	0.00	4.00	8.00	8.50	9.25	10.50	11.75	13.00
Distance (mm)	0.00	203.2	408.4	433.9	469.3	532.8	596.3	660.0

Figure 4-3 Cut-view of the rig, showing the position of the different planes

The motorized traverse system (Figure 4-4) is used to measure vertical velocity profiles with the pitot tube or the HWA. The sensor (6) is clamped to the pillow block (3a) of a linear rail system (3, Thomson Industries 2BB06OTHAAL16) by two 3D-printed parts (5a, 5b). A limit switch (4a) is fixed to the pillow block (3a) by a 3D-printed bracket (4b). The system is actuated by a DC motor (1, Pittman 14207S008 with 500 CPR encoder). All 3D-prined parts on the gantry were printed in Onyx with a Markforged X7. The frame is made of aluminum extrusions. The assembled rig is presented in Figure 4-5.

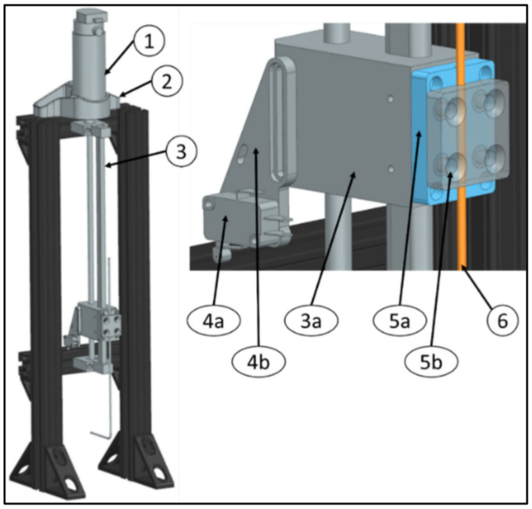

Figure 4-4 Traverse Measurement Gantry

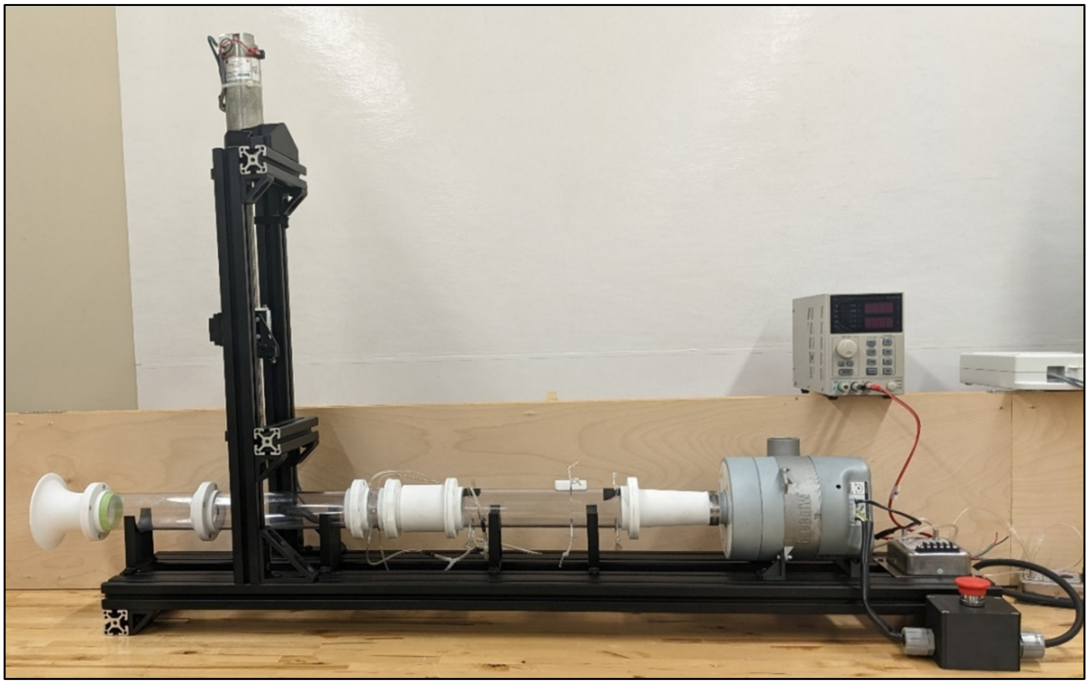

Figure 4-5 Picture of the assembled test rig

A preliminary calibration maps the control voltage (V_c) to the bulk velocity (U) in the duct to establish a reference table. To account for the variation in the pressure drop caused by different grid stacks, the control voltage will be adjusted before each run to ensure the nominal velocity is consistent between tests.

It was decided early on to focus on low Reynolds in order to compare results with the literature and because designing a rig capable of operating at the same conditions as the combustor (Re > 300 000) falls outside the scope of a master's project and is significantly more expensive.

The bluff body will be rotated clockwise when looking downstream (from the right in Figure 4-6) and the angular position will always be positive (0-180°), with 0° being the horizontal bluff body position. The flange of the test section (item 4A in Figure 4-2) has a flat surface parallel to the bluff body, which is used as the reference plane to measure the angular position of the bluff body. It is measured using a digital level. The position of the test section is locked using four spring-loaded clamps. When discussing the radial position, the probe is said to be at 0mm when it intersects the centerline of the tunnel (red dashed line in Figure 4-6). Negative values indicate the probe is located above the tube's axis.

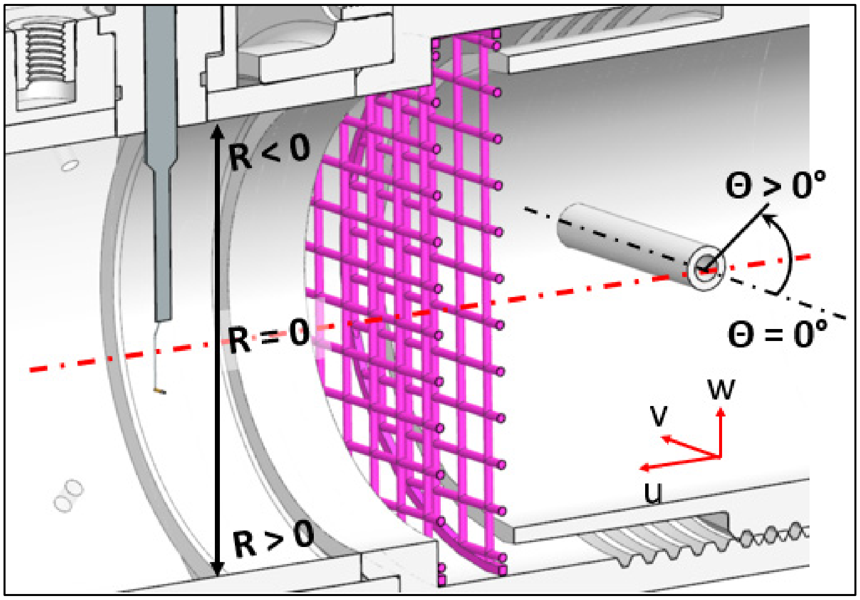

Figure 4-6 Sign convention for the angular position of the bluff body and for the radial position of the probe

4.3 Measurements

The efficiency of different grid stacks at damping the vorticities is assessed by measuring the TKE transmitted downstream of the grids and the pressure drop caused by the stacks. Characterization of the vortices is done using hot-wire anemometry (HWA) and the pressure drop is calculated by monitoring the static pressure at different planes.

The static pressure is measured via a series of pressure taps located on the wall of the cylinder. Four taps (Ø1.00mm), equally spaced by 90°, are connected in a "triple-T" arrangement to average the pressure at a given plane, as shown in Figure 4-7. There are five planes of measurements on the test rig. P_{IN} is located at the front, just past the inlet nozzle and the measuring section is divided in four equidistant plans P_{M1-4} (see Figure 4-3). The pressure drop is measured between P_{IN} and P_{M1} using an Alpha Instruments 161W0R25DB2YA sensor (0-0.25" H_2O +/- 0.25%FS).

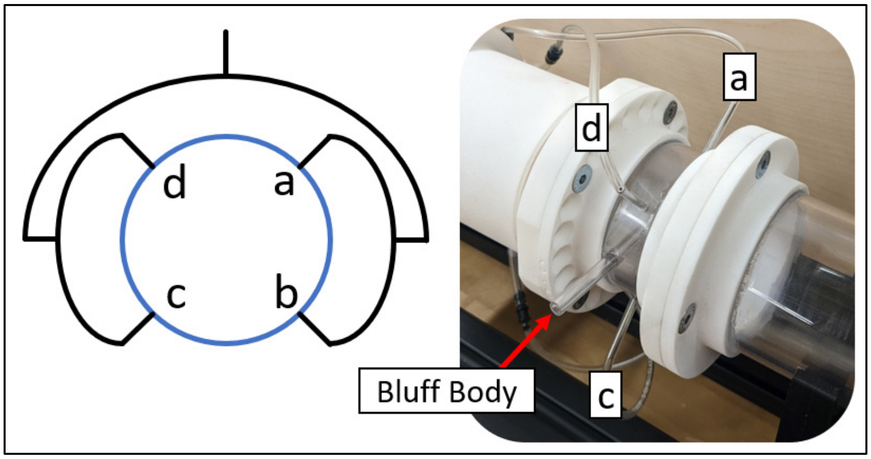

Figure 4-7 Triple-T arrangement

Two methods are used to measure the air velocity in the test tunnel. Commissioning of the rig was done using a pitot-static tube mounted to the motorized arm. Pitot-tubes are easy to use, and the pressure transducers are inherently calibrated, which removes a lot of potential errors during the first steps of getting the rig operational. The pitot tube is connected to an Omega Engineering PX653-01D5V sensor (0-1" H_2O +/- 0.30%FS). The working principle of the pitot tube and the error margin are described in ANNEXE II. Pitot-static tubes have a relatively low frequency response, which is better suited to measure the average speed of the flow. Several velocity profiles were measured with the pitot tube over the velocity range of the blower motor, both with and without the bluff body.

The profiles were then repeated with the HWA and compared to validate the results. All subsequent tests were performed with the HWA, because its high frequency response can detect the instantaneous fluctuations in the flow caused by the vortices, allowing the calculation of the TKE.

This study uses a gold-plated single-wire model (55P11, Dantec Dynamics), which is well suited for the turbulence intensities expected during testing. This type of sensor has a 3mm long wire and the extremities are copper- and gold- plated to thickness of 15-20µm, leaving only an "active" sensing zone of 1.25mm in the middle. The probe is mated to Tao-Systems Model 4-600 constant voltage anemometer (CVA) [30]. Due to time constraints, velocity measurements were only done for the baseline conditions and for the single grid cases. For the multi-grid configurations, only the pressure drop and nominal velocity were measured.

4.3.1 Hot wire measurement and calibration

Single-wire probes are mostly sensitive to air moving perpendicular to the wire (*u, w* in Figure 4-8), but cannot discriminate the direction of the flow. During calibration, the air stream must be as smooth as possible to avoid inducing crossflow error in the measurement. Bi-axial probes, such as the X-probe, have the advantage of measuring two components at once, but are notoriously difficult to calibrate and would be too big for this setup. In this application, the objective is to measure the turbulent kinetic energy and determining the orientation of the flow field is not really a concern.

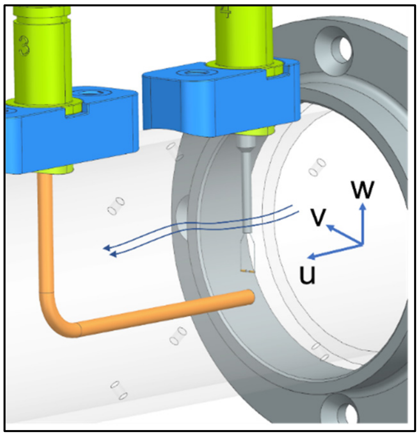

Figure 4-8 Pitot-static tube and HWA probes in the flow

The hot-wire is travelled by a constant input voltage (0.5 V) which is maintained by an anemometer (CVA). The detail of it is given in ANNEXE III. The instantaneous output voltage Vs is related to the local instantaneous flow velocity ($U = sqrt(u^2 + w^2)$). However, this relation is not linear and the CVA must be calibrated by exposing the probe to a series of known velocities. The air temperature and barometric pressure must be recorded to calculate the air density. By running a velocity sweep, one can obtain a calibration curve similar to Figure 4-9. A power law can then be fitted and is used to calculate the velocity during testing [30]. This calibration step is typically done using a dedicated laboratory-grade probe calibrator or by placing the probe in a wind-tunnel alongside a pitot-static tube. The probe must be recalibrated every time the anemometer is switched off.

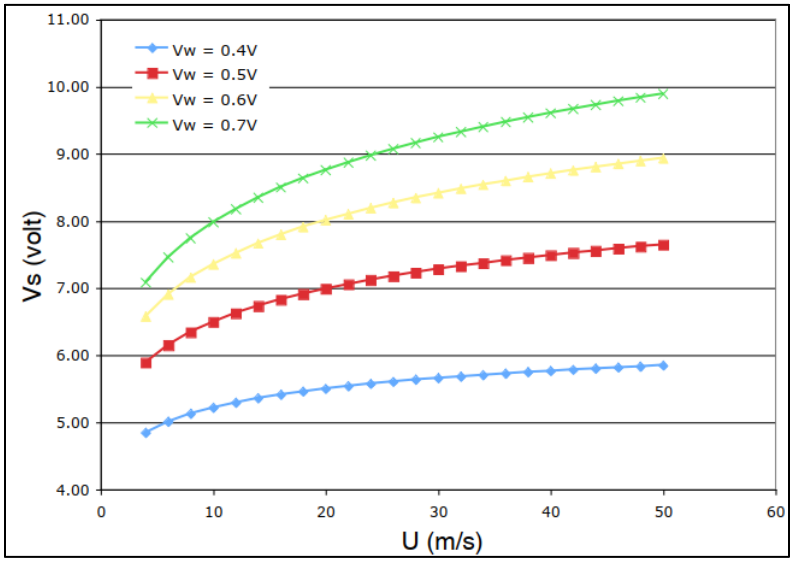

Figure 4-9 Calibration curve, Vs - U, reprinted from [31], p. 2. © 2005 by Tao of Systems Integration Inc

One drawback of this method is that it is only as precise as the calibration equipment used. For low velocity (<5m/s), the relative error of the pressure transducer can be significant, as explained in ANNEXE II.

Another caveat of this approach is that it involves a lot of delicate manipulations when the calibration is done ex-situ, which is the case for this study. The test section is too small to accommodate the reference pitot-tube and the hot-wire next to each other. For this reason, the probe was initially calibrated using the TFT wind tunnel. The HWA then had to be carefully transferred into the test section with all the wires connected. This process was time-consuming and resulted in one broken probe.

Alternatively, the probe can be calibrated in-situ by measuring the vortex-shedding frequency of a bluff body placed upstream. The probe must still be exposed to a series of velocities, but rather than relying on the pitot-tube to calculate the flow speed, the velocity is calculated from the measured vortex-shedding frequency, which is associated to a velocity through the known Strouhal number (see Eq. (1-9)). To do so, the temporal signal recorded is converted to the spectral domain by applying a fast Fourier transformation (FFT), as shown in Figure 4-10. The spectral signal is then filtered to isolate the peak shedding frequency and the velocity is calculated using Eq. (1-9).The post-processing steps and algorithms are presented in ANNEXE IV.

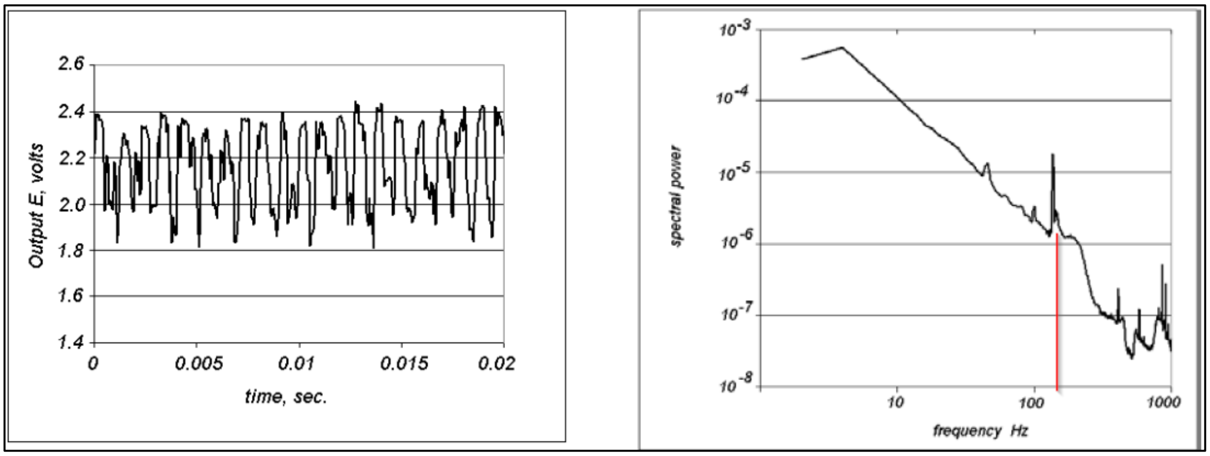

Figure 4-10 Time- and Spectral- domain signal traces of the velocity behind a bluff body.
Reprinted from [32], p. 35. © 2005 by Dantec Dynamics

This approach was used with success by various investigators, including Sattarzadeh *et al.* [33] and El-Gabry *et al.* [34]. This technique works best when the probe is located in the strong wake region, because the fluctuations are stronger, and the peak energy is more pronounced. The evolution of the peak PSD as a function of the radial position of the HWA relative to the bluff body's centerline is presented in Figure 4-11. The highest amplitude is detected $2D_{bb}$ (-10, +10 mm) above or below the bluff body centerline, which is consistent with the results from [33].

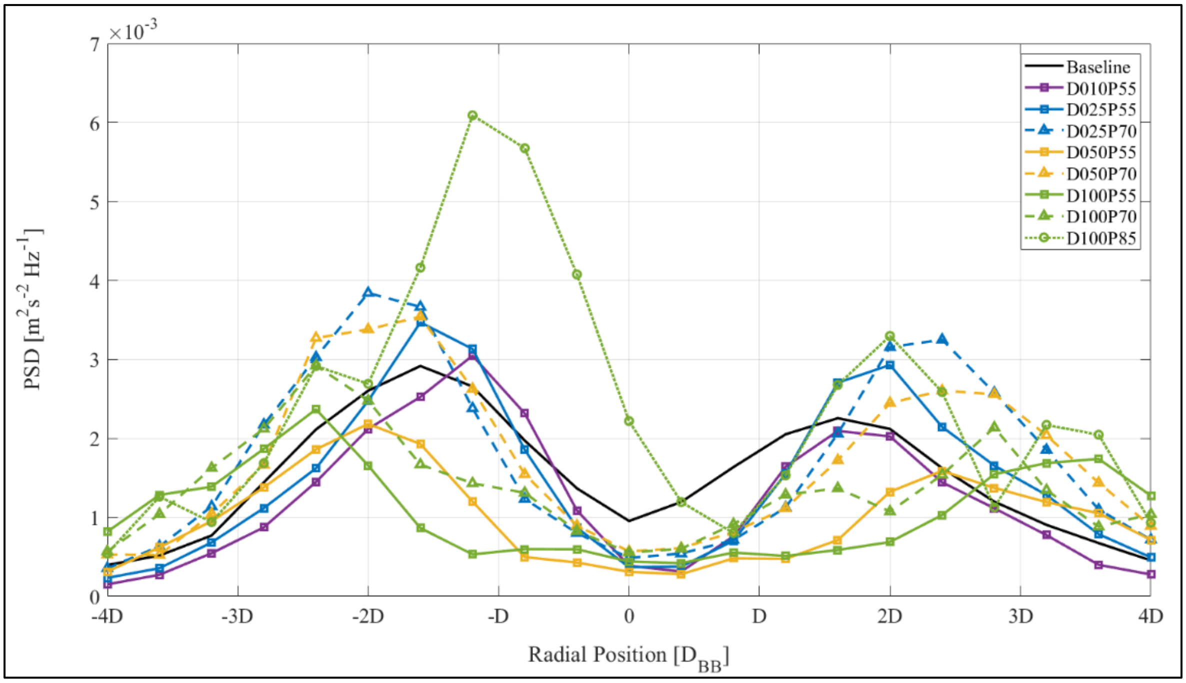

Figure 4-11 Evolution of the peak PSD (~400Hz) vs. radial position of the probe, U=10 m/s

4.4 Velocity maps

Mapping the velocity profile of the wind tunnel is achieved by doing a series of traverse and clocking the angular position of the test section. The HWA was installed in the second measuring port, equivalent to P_{M2} in the simulation. Each traverse begins with the sensor at the minimum position and moves up gradually in steps up to the maximum position. The motorized arm pauses at each step for the duration of the recording (20s @ 8 kHz).

For the baseline mapping, the hot-wire traveled from -20mm to +20mm in steps of 1mm and the test section with the bluff body was clocked from 0° to 180° in increments of 15°. This mapping was extremely fine to verify the symmetry of the rig.

When testing with the grids, the hot-wire traveled from -20mm to +20mm in steps of 2mm and the test section was clocked from 0° to 90° in steps of 30°. The range of mapping was significantly truncated to reduce the testing time per sample and because the rig is symmetrical.

4.4.1 Baseline conditions

The following subsections present the velocity profiles and TKE distribution for the test rig in its baseline configuration, i.e., without any grids. The baseline conditions were measured both with and without the bluff body in place to quantify the effects of the wind tunnel itself. Mapping the baseline conditions, i.e., the flow field without the grids, is a crucial first step. The results of the grids will be compared against these values to assess their effectiveness.

4.4.2 Velocity profile

The flow field inside a tube is not uniform because of the boundary layer developing along to the duct wall. In the case of an unobstructed, fully turbulent flow in a cylindrical pipe, the velocity profile can be approximated with a power law (Eq. (4-1)), where *u* is the velocity, *r* is the radial distance from the axis, *R* is the radius of the cylinder and *n* is a coefficient [9]. While *n* is dependant of Re, a value between 7-9 fits most cases of turbulent flows inside a smooth wall cylinder [10]. The velocity sweeps for different blower motor control voltages are presented in Figure 4-12 and Figure 4-13.

$$\frac{u}{u_{max}} = (1-\frac{r}{R})^{\frac{1}{n}} \tag{4-1}$$

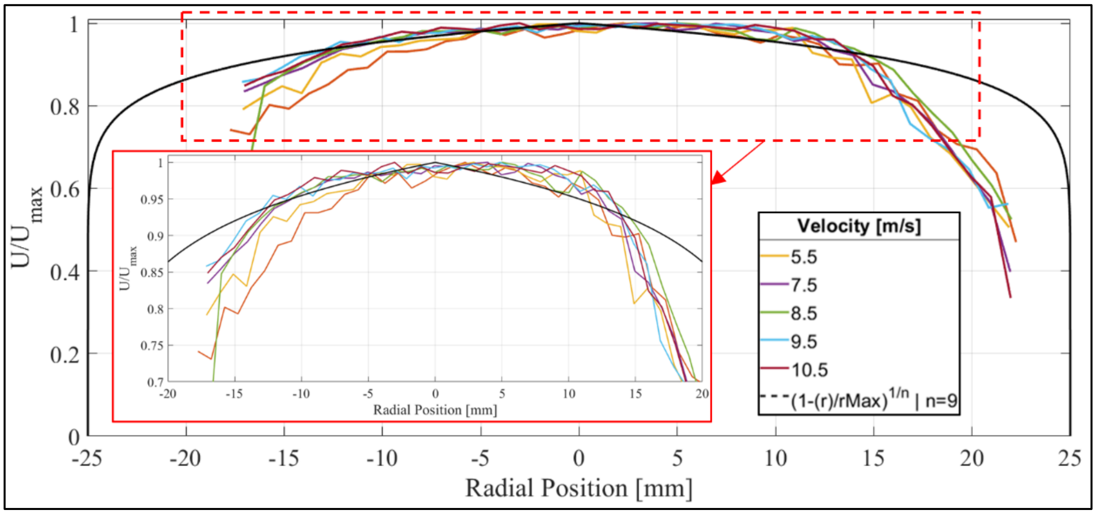

Figure 4-12 Baseline velocity profile without the bluff body. Inset shows the region bound between r = [-20, 20] and U = [0.7, 1.0]. The black curve corresponds to the power law fitted with n=9

Looking at Figure 4-12, the velocity begins to fall sharply when the probe reaches the 15mm mark. This is likely due to the blockage created by the probe and the interference with the wall.

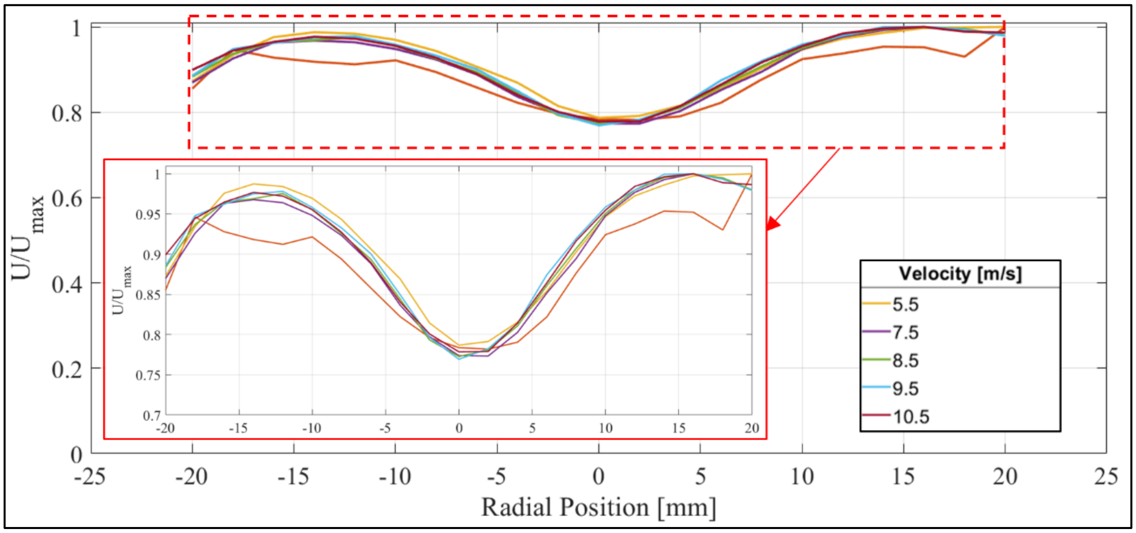

Figure 4-13 Baseline velocity profile with the bluff body. Inset shows the region bound between r = [-20, 20] and U = [0.7, 1.0]

When the cylinder is introduced in the test rig (4B, Figure 4-2), it creates a blockage which forces the fluid to move around it. This results in an M-shape velocity profile with a dip in the wake of the bluff body and higher velocities above and below as the fluid accelerates, see Figure 4-13. No known analytical model exists to predict this profile. The velocity profiles measured downstream of the bluff body are consistent with results from Berlinski *et al.* [35]. The slight asymmetry in the velocity profiles (left vs. right) is a result of the blockage created by the hot-wire anemometer as it descends further inside the tube.

4.4.3 Turbulent Kinetic Energy

The turbulent kinetic energy (TKE) represents the kinetic energy per unit of mass carried by the fluctuating flow. It is measured using HWA and calculated using the sum of the root mean square (RMS) of the velocity fluctuations, see Eq. (4-2).

$$TKE = \frac{1}{2}\left(\overline{u'^2} + \overline{w'^2}\right) \approx u'^2_{HW} \tag{4-2}$$

A single-wire probe cannot discriminate between the velocity components, hence the variance detected is the sum of all three components. In practice, the effect of the lateral fluctuations (v) is negligeable because the main vorticity generated by the bluff body is parallel to the flow (rotates around the y-axis). For this reason, the equation is simplified.

In the tube-only condition i.e., without the bluff body, the TKE intensity evolves in opposite direction of the velocity and rises as the flow gets closer to the cylinder wall. It appears fairly uniform. When the bluff body is introduced, the shedding vortices cause the TKE to surge in the center of the cylinder. The effect of the bluff body is flagrant when looking at the spatial distribution of the averaged velocity and TKE (Figure 4-14), measured at P_{M1}.

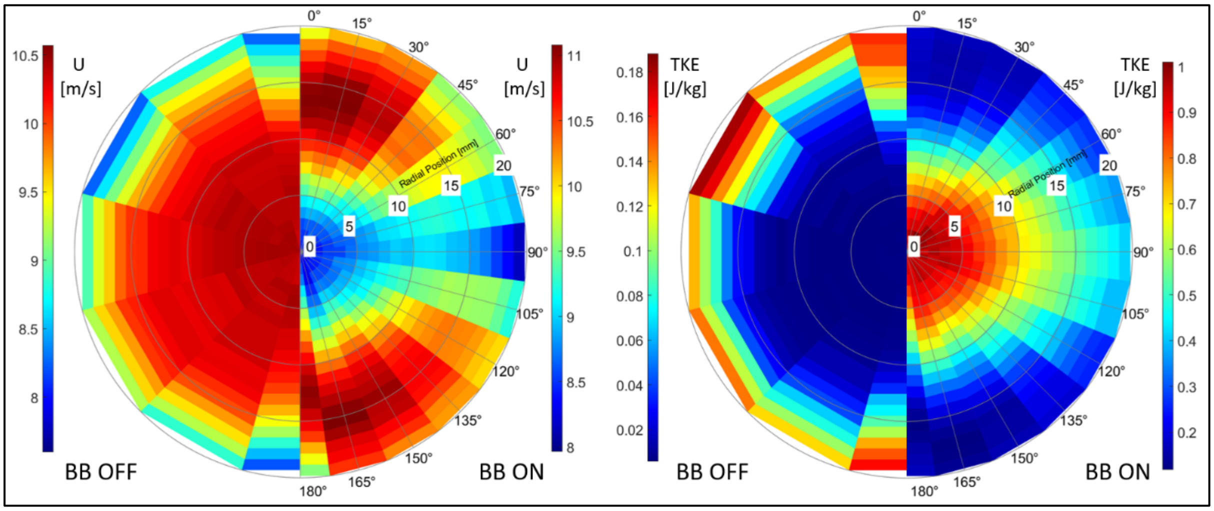

Figure 4-14 Surface maps of the baseline local velocity (Left graph) and TKE (Right graph). Left hemisphere = without the bluff body, Right hemisphere = with bluff body

4.4.4 Turbulence Intensity

Turbulence intensity (T_u) characterises the level of turbulence in a flow field and is a typical metric for wind tunnel quality. It is calculated by Eq. (4-3) as the ratio between the RMS of the velocity fluctuations over a period of time and the mean velocity recorded over the same period. For a perfectly laminar flow, T_u would therefore be 0%.

$$T_u = u'/\bar{U} \tag{4-3}$$

The acceptable level of turbulence intensity depends on the application. The average T_u in the pipe is 2.80% without the bluff body, and 11.0% with the bluff body.

4.5 Experimental results for the grid stacks

The following chapter presents the experimental results obtained with the rig. Great care was taken to arrange the grids as close to perfectly inline as possible, but the grids were often shifted slightly. This was particularly tricky for the 55% porosity grids. The pressure drop was measured for all the experimental configurations (single grids and triple stacks), but the velocity measurements were limited to the single grid cases due to time constraints. The HWA was installed in the second measuring port, equivalent to P_{M2} in the simulation.

4.5.1 Pressure drop

The variation of the pressure drop, calculated with Eq. (3-2), as a function of the intergrid spacing is presented in Figure 4-15 for the experimental configurations. In addition to the three spacings tested (ε=2.5, 5.0 and 7.5 mm), a fourth column (INF) is added, which extrapolates the results if the three grids were infinitely separated by multiplying the pressure drop from the individual grid cases by three. Note that the actual porosity of the grids differs from the nominal value. To account for these deviations, the pressure drop results were corrected by the ratio of the actual porosity divided by the nominal porosity. Note that the results for Retimet are omitted because the thickness is constant and the dP measured far exceeds the results of the grids (dP Retimet = 1120 Pa).

Table 4.1 Actual porosity of the different grids tested

Grid	Experimental Øw [mm]	Actual Porosity [%]
D025P55	0.25	52
D025P70		73
D025P85		-
D050P55	0.51	57
D050P70		78
D050P85		-
D100P55	1.04	57
D100P70		70
D100P85		84
Retimet	N/A	92

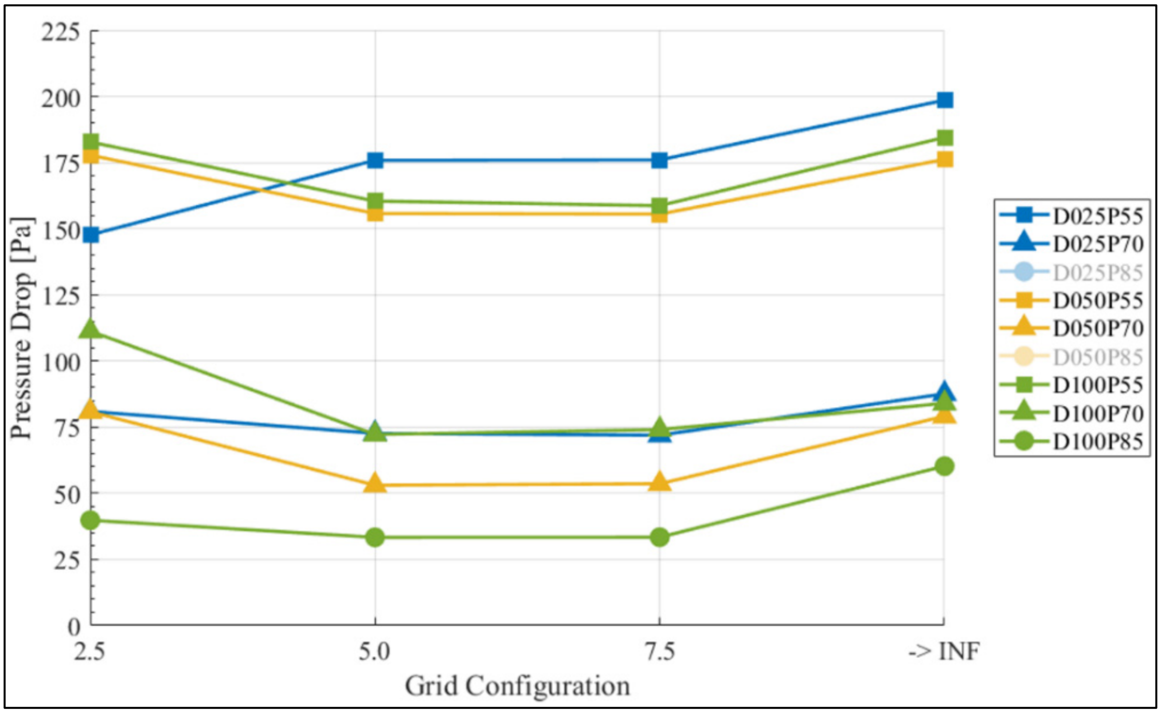

Figure 4-15 ΔP evolution vs. intergrid spacing for experimental configurations. The greyed configurations are not available.

Looking at Figure 4-15, nearly all the conditions tested have the same U-shape profile, where the pressure drop is maximal when the grids are closely packed (ε = 2.5 mm) or spaced far away (ε = INF), with a minima plateau in the middle. The net reduction in dP when the intergrid spacing increases from 2.5 mm to 5.0 mm could be a consequence of the imperfect grid alignment. When the grids are offset, packing them closely results in a lower apparent porosity, which translates in greater pressure losses since the air has to navigate sharper turns between the grids. By increasing the spacing, the wakes formed by the grids upstream have more room to diffuse and navigate around the grids downstream. Further increasing the gap from 5.0mm to 7.5mm has no effect on the pressure drop. The “rebound” noted when ε = INF suggests that the interaction with the first grid is responsible for a larger proportion of the pressure loss than the subsequent grids. Unfortunately, the test section is too short to test larger spacings between the grids. It is therefore not possible to confirm if the rebound is an overestimation or if there is a distance such that the grids act like three independent ones.

The second main takeaway from Figure 4-15 is the influence of the porosity. As one would expect, increasing the porosity leads to a reduction of the pressure drop.

4.5.2 TKE Reduction

Figure 4-16 presents the reduction of TKE relative to the baseline (configuration without the grids), calculated by Eq. (3-3), for the different experimental configurations. The results obtained were corrected by the ratio of the nominal porosity divided by the actual porosity.

Of all the configurations tested, the foam was the most effective at reducing the transmitted TKE. In comparison, the results for the single grids are impressive and suggest that a well-designed stack of grids could be just as effective.

For a given grid wire diameter, increasing the porosity leads to a reduction of the grid’s ability to dampen the turbulence. This is expected because an increase in the grid’s porosity results in fewer wires in the flow breaking down the incident vortex. There is no clear evidence of the grid wire diameter affecting the residual TKE with the results available.

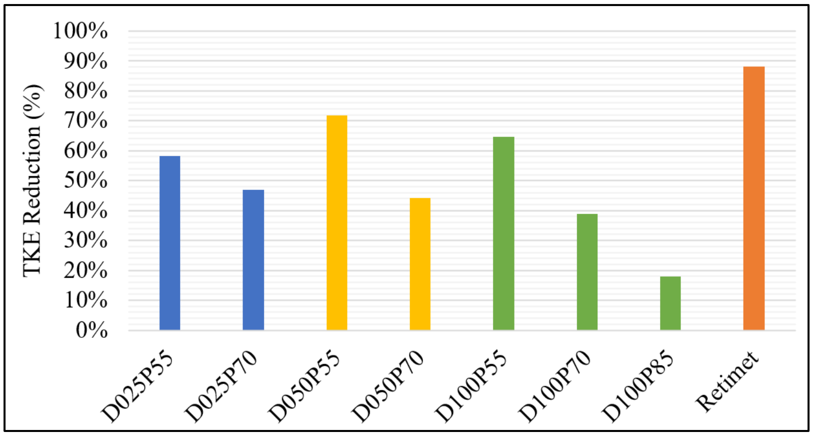

Figure 4-16 TKE Reduction relative to baseline for the experimental configurations

4.5.3 Flow field uniformity

The results for the post-interaction flow field uniformity are presented in Figure 4-17. Overall, the flow field uniformity measured is quite high; even the baseline configuration, i.e., just the bluff body, scored over 90%. Introducing the grids does help increase the uniformity to around 96% on average. For a given wire diameter, increasing the porosity leads to reduction of the flow field uniformity. For a given porosity, it appears that increasing the wire diameter results in a slightly better uniformity.

Considering that the uniformity achieved by the Retimet hovers around 98%, it is safe to assume that this likely represents the upper limit in uniformity. Interestingly, a single D100P55 grid was just as effective at the foam to homogenize the velocity field.

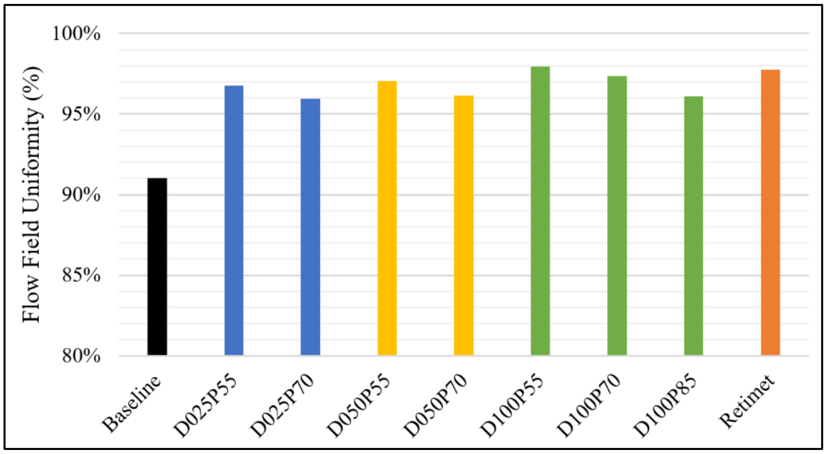

Figure 4-17 Flow field uniformity for the experimental configurations

4.6 Conclusion

This chapter described the experimental wind tunnel designed to study the vortex breakdown performance of different porous structures. Two different methods were used to measure the velocity inside the tunnel. The pitot-tube was used mainly to commission the rig. A hot-wire anemometer was then used to measure the flow field, as it can detect the high frequency fluctuations from which the TKE is calculated.

The baseline flow characteristics of the rig i.e., without the grids, were first measured to establish a reference against which the grid configurations were compared.

The grid porosity has a major influence on the vortex breakdown performance. Reducing the porosity is linked to an increase of the pressure drop, an increase of the transmitted TKE attenuation and an increase in the flow field uniformity. Increasing the wire diameter tends to improve the flow field uniformity, but otherwise does not influence the pressure drop or the transmitted TKE level in a meaningful way.

Due to time constraints, the results for the flow field are limited to the individual grid configurations, which limits the extent of the conclusions. In comparison to the foam sample, some the grid stacks performed well. While more work is needed to complete the design of experiments, it is likely that an optimized grid stack will be able to match or even outperform the current foam.

CHAPITRE 5

DISCUSSION ON THE EXPERIMENTAL AND NUMERICAL RESULTS

In this final chapter, the experimental and numerical results are compared and criticized. The plausible cause for the discrepancies are identified and their influence is discussed. This analysis draws the steps towards further research.

5.1 Pressure drop

The evolution of the pressure drop as a function of the intergrid spacing is presented for three grid configurations (D_w = 0.25, 0.50 and 1.00mm) in Figure 5-1 (φ =55%) and in Figure 5-2 (φ =70%). The dark solid columns correspond to the CFD inline configurations, the dotted columns correspond to the CFD offset configurations and the solid pale configurations correspond to the experimental results. Note that the column for the Retimet foam sample (orange, far left) is truncated since the pressure drop measured far exceeds that of the other configurations.

When comparing the experimental and numerical results, two things stand out in particular. First, the simulations overestimate the pressure drop. Second, the magnitude of the overestimation shrinks as the wire diameter increases. This suggests that the model could be improved by either increasing the mesh resolution or by fine-tuning the turbulence model dissipation parameters, or a combination of both. It could also be a result of the limited accuracy of the turbulence model when 3D mixing is at play around the nodes between the horizontal and vertical grid members. This would disproportionally affect the finer grids since they are composed of a greater number of wires than the coarser grids for a given porosity. This likely explains why the numerical results suggest that increasing the wire diameter leads to a decrease of the pressure drop, and why that trend is not observed experimentally. For this reason, the focus will be on the trends.

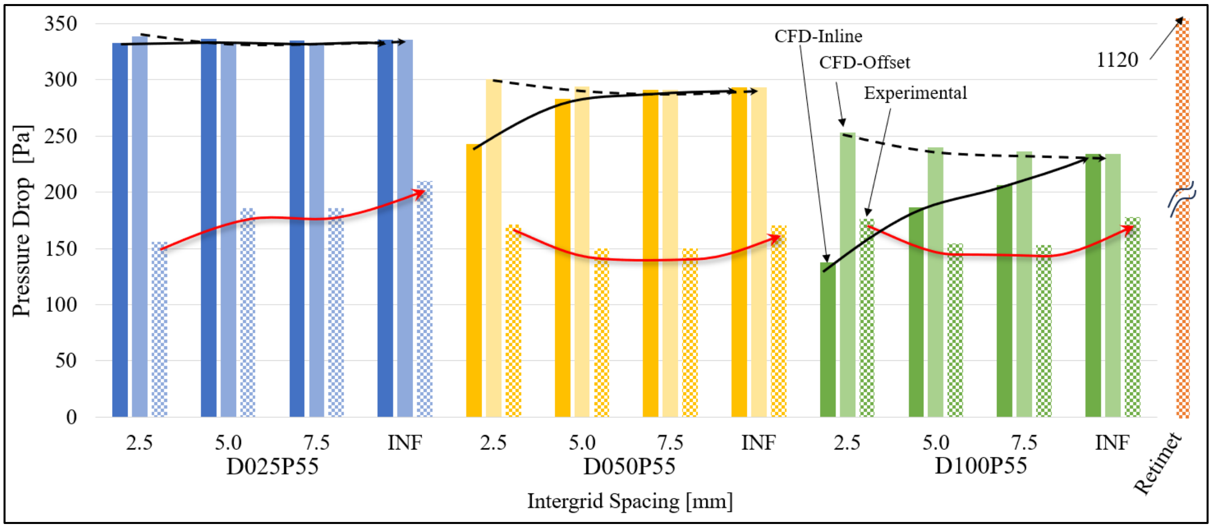

Figure 5-1 ΔP evolution vs. intergrid spacing for φ =55%
Dark solid = CFD inline, Pale solid = CFD Offset, Dotted = Experimental

Looking at Figure 5-1 (φ =55%), the experimental grid stacks (dotted columns) exhibit a trend similar to the offset grid configurations at first, with the pressure drop decreasing as the intergrid spacing increases. The trends for the D050 and D100 CFD offset cases are reasonably similar to the experimental results, which suggests some level of misalignment of the grids during the experiments. The pressure drop measured experimentally for the different configurations are generally about half that of the numerical results.

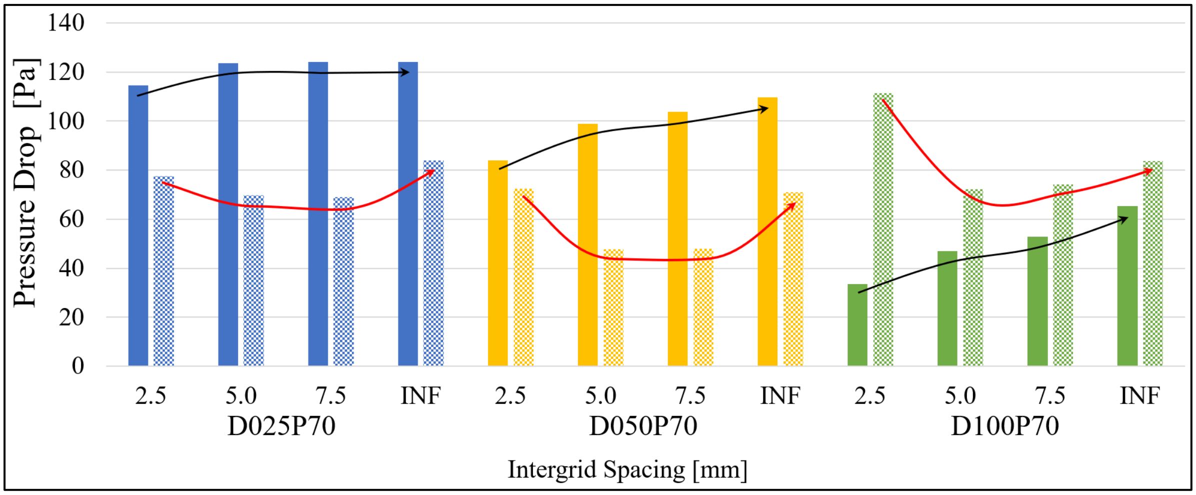

Figure 5-2 ΔP evolution vs. intergrid spacing for φ =70%
Dark solid = CFD inline, Pale solid = CFD Offset, Dotted = Experimental

Looking at Figure 5-2 (φ =70%), the experimental grid stacks (dotted columns) again exhibit a downward trend as the intergrid spacing increases from 2.5mm to 5.0mm, followed by a minima plateau. The offset configurations were not simulated for the φ=70% cases. In general, the experimental and numerical results are closer for these more porous configurations. The pressure drop measured for the D100P70 cases is actually greater for experimental results. As the porosity increases, there are fewer grid wires in the flow, which minimizes the overestimation of the model.

5.2 TKE

Figure 5-3 presents the TKE reduction for the individual grids. The solid columns represent the numerical results and the dotted columns represent the experimental results.

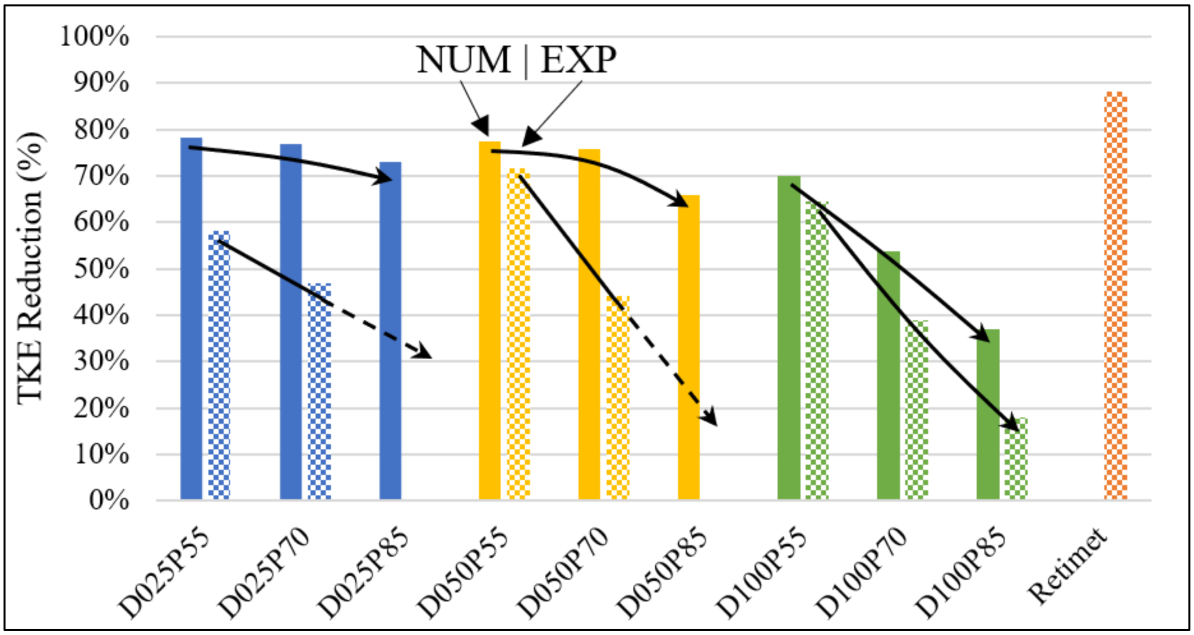

Figure 5-3 TKE reduction for the single grid configurations
Left (solid) = Numerical, Right (dotted) = Experimental

The general trends in the TKE evolution are somewhat consistent between the numerical and experimental results. For instance, the TKE reduction is markedly inferior for the D100 grids, and increasing the porosity of the grids results in a lower TKE reduction potential. However, the experimental results suggest that the residual TKE level downstream of the grids is more porosity-dependant than the numerical results would suggest. This is evidenced by the much steeper trendlines of the experimental results vs. the numerical results. It also appears that the magnitude of the difference between the experimental and numerical results shrinks as the wire diameter increases. When comparing the results for D025 and D100 cases, the absolute difference between the configurations is significantly smaller and the slopes of the trendlines are more similar. The better agreement between the numerical and experimental results for the larger wire diameter again suggests the model does not fully capture the wall flow on the grid struts and could benefit from a finer mesh resolution and/or adjustments to the turbulence model.

It should be noted that the TKE values measured in CFD are modelled, while the TKE measured experimentally is time-resolved. In future campaigns, it would be important to also evaluate the fluctuations that contribute to the TKE in CFD.

5.3 Uniformity

Figure 5-4 presents the flow field uniformity for the individual grids. The solid columns represent the numerical results and the dotted columns represent the experimental results. The obvious difference between the numerical and experimental results is that the former are almost indistinguishable from one another, whereas the numerical results have a clear decreasing trend in the flow field uniformity as the porosity increases.

Based on the numerical results, it would seem that placing any grid in the flow is sufficient to improve the flow field uniformity by 5%, and that neither the wire diameter nor the grid porosity have a noteworthy effect. However, the experimental results tell a different story. For one, reducing the porosity tends to improve the uniformity, which would be expected since the more restrictive grids generate more mixing. In addition, increasing the wire diameter also helps improve the homogeneity of the velocity field, although the available data does not provide enough information to explain this observation.

The higher uniformity measured experimentally may be a consequence of where the flow field is measured. For the experimental results, the probe was located at P_{M2}, but for the numerical results, the flow field uniformity was measured at P_{M1}, in an attempt to detect some differences between the grids. The lack of differentiation in the numerical results would warrant a deeper investigation to understand the cause.

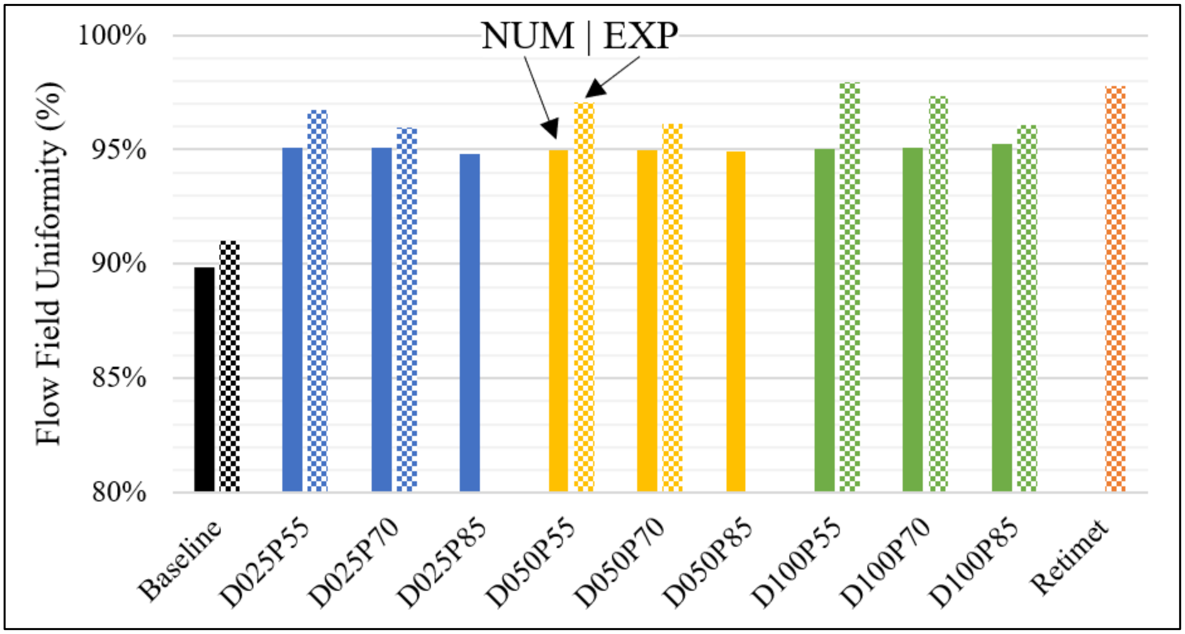

Figure 5-4 Flow field uniformity for the single grid configurations
Left (solid) = Numerical, Right (dotted) = Experimental

5.4 Conclusion

In conclusion, the experimental and numerical results tend to be in agreement for the general trends, but some of the discrepancies cannot be fully explained with the data available. The limited set of experimental results is insufficient to fully validate the numerical models. Moving forward, il would be important to complete the velocity profiles for the grid stacks.

The wire diameter sensitivity is the main issue, and more work is needed to pin-point the source of the discrepancies between the numerical and experimental results. It could stem from the mesh not being sufficiently refined, but could also be due to the turbulence model employed in the study. It is also important to consider potential issues with the test rig itself, such as the effect of the probe and its placement within the rig or leaks. This serves as a good reminder of the importance of a thorough validation protocol.

CONCLUSION

The original objective of this study was to develop a 3D-printable lattice structure capable of replacing a conventionally-made foam. The intent was to design an alternative that would be as effective as the foam at breaking down incoming vortices inside a gas turbine combustor, while being more permeable to minimize the pressure losses.

To this end, foam samples were CT-scanned and analysed using VG Studio to determine the mean geometrical dimensions of the foam, which served as a baseline to design alternative lattice structures. The permeability of the foam samples was also measured numerically, using tools from the VG Studio suite, and experimentally, using a custom-built water tunnel. At the time, it was hypothesized that a geometry of comparable permeability and tortuosity as the foam would incur a similar pressure gradient.

Next, seven different lattice structures were created and their geometries were iteratively adjusted. One of the main challenges was the lack of explicit control over the permeability and tortuosity of the structures in the design process. This meant that every design candidate had to be analysed in VG Studio. This approach proved to be tedious and very time-consuming. As the different candidates were trialed and refined, the lack of correlation between permeability, tortuosity and pressure gradient became evident. Alternatively, the relationship between the pore's shape and size, and the pressure gradient was also investigated. However, a clear correlation could not be established.

These setbacks prompted a different approach to the problem, as it became clear that any optimization work done for a single lattice structure would still have to contend with the CAD limitations. In addition, there were serious doubts about the exportability of the results to a different set of conditions or objectives.

A more pragmatic approach emerged, in the form of a design of experiment using stacks of independent grids. This approach presents various benefits, such as a direct control over the design parameters and the potential for more widely applicable results. Furthermore, it would provide a more fundamental understanding of how the basic lattice structure parameters, such as the pore size, porosity and strut diameter influence the flow characteristics of the structures.

The intent behind this project remains the same, but the objective pivoted towards the development of design guidelines for vortex-breaking grid stacks. It is expected that the conclusions from this second study would also apply to lattice structures.

For this second investigation, an experimental simulation protocol was created to systematically study the influence of four core parameters of a grid stack using a simple incompressible-unsteady RANS model. These parameters are the wire diameter, the porosity, the intergrid spacing and the grid alignment. The vortex-breakdown performance of the grids is evaluated with four KPIs, which are the pressure drop, the residual turbulent kinetic energy, the flow field uniformity, and the size of the transmitted vortices. To mimic the conditions within the combustor, the model relies on a Von Karman vortex street created by placing a cylindrical bluff body perpendicular to the flow inside a narrow tunnel.

The investigation revealed many important elements. The wire diameter of the grid is a powerful design lever. For one, larger wires create stronger wakes which extend further downstream, which amplifies the effect of subsequent grids. For two, the larger wake increases the breakdown of the vortical structures, but also contribute to the overall TKE level. On the other hand, smaller wires are less effective at breaking down vortical structures, but are better at reducing the residual TKE.

The pressure losses can be minimized by increasing the grid porosity and minimizing their numbers in a stack. The effect of the spacing between the grids depends on the grid alignment. When the grids are perfectly aligned, the wake generated by the upstream grids creates a low-pressure zone. The closer the next grids are, the more they can benefit from this drafting effect, resulting in fewer losses. However, if the grids are misaligned, increasing the distance between the grids is favorable to minimize the pressure drop. Finally, decreasing the porosity and the wire size result in higher flow uniformity due to the lower turbulence.

For a given TKE reduction target, it is preferable to reduce the wire diameter of the grids while keeping the porosity high, as this arrangement results in a lower pressure drop.

To validate the numerical study, a custom-designed wind tunnel was built. The velocity was measured using a hot-wire anemometer coupled to a motorized linear arm to conduct traverse measurements over the diameter of the tunnel. The angular position of the bluff body was clocked between each traverse to obtain the full image of the flow conditions downstream of the grids. In addition, a series of pressure taps were used to measure the pressure losses. Due to time constraints, the velocity flow field was only captured for the single grids, but the pressure losses were measured for all of the configurations.

While the experimental and numerical results are generally in agreement when it comes to global trends, such as the effect of the grid porosity on the residual TKE, some discrepancies would require further work to pin-point their sources and improve the numerical model.

In conclusion, the optimal design should be a graded structure, starting with a very porous grid made from a large wire diameter to breakdown the incoming vortices. Additional grids should be rotated and offset to increase the tortuosity, as it improves the velocity homogeneity. The wire diameter of the subsequent grids should be progressively smaller to reduce the TKE. The spacing between the grids should be as large as possible and their numbers must be kept to a minimum to avoid excessive pressure losses. The porosity should only be reduced when the desired velocity uniformity cannot be obtained by other means.

RECOMMANDATIONS

In future work, varying the size of the bluff body would provide valuable information to better understand how the ratio between the vortex size and wire diameter impacts the grid performance. It would also be valuable to rerun the models at higher Reynolds and greater compression ratios to extend the results over a more meaningful range of conditions. In addition, the intergrid spacing should be calculated as a function of the wire diameter of the grids, such that the spacing is proportional to the grids rather than the incident vortex. It would also be interesting to redo some of the simulations without the bluff body to isolate the effect of the grids.

In future work, it would be beneficial to increase the size of the rig to minimize the influence of the HWA. Automating the clocking of the bluff body section would significantly improve the measuring process. Having to remain next to the rig the whole time and clocking the rig every 10-15 minutes is hugely time-consuming and is prone to human errors.

ANNEXE I

MESH SENSITIVITY

The shedding frequency of the vortices is function of the bluff body diameter and the flow velocity. It is calculated by measuring the period of the lift force fluctuations acting on the bluff body. The shedding frequency (*f*) is often expressed in terms of Strouhal number (St). Based on empirical evidence in the literature, the Strouhal number for a cylindrical bluff body in the 49>Re>5000 range is around 0.20 +/- 0.01 [13]. The global target size and global refinement zone are kept constant at 2.5 and 1.0mm, respectively. The mesh was first refined for the baseline condition i.e., just the bluff body without the grids. The bluff body and its wake were refined successively until the drag coefficient stabilized to less than 1% relative to the ultra-fine case. The intermediate mesh (#3) was selected because the drag coefficient (C_D) and *St* are within the typical literature range [36, 37]. The drag coefficient is calculated by Eq. (A I-1), where F_D is the drag force acting on the bluff body. Note that the bluff body diameter (*d*) and the tunnel diameter (*D*) are in meters.

$$C_D = \frac{F_D}{\frac{1}{2} d \cdot D \cdot \rho \cdot U^2} \tag{A I-1}$$

Once the mesh for the baseline condition was satisfactory, a grid was introduced in the model. Again, the surface mesh and the wake of the grid were successively refined until the drag, on the grid this time, leveled to around 1% of the ultra-fine mesh. The configuration with the smallest wire and highest porosity (D025P85) was selected. The mesh size was kept constant for the other grids, regardless of the wire size.

Table-A I-1 Mesh Sensitivity

#	Cell count	Cd	St	Cell size [mm]	
				Surface	Wake
1	287 666	1.236	0.207	0.500	0.5
2	639 365	1.108	0.208	0.100	0.5
3	1 682 121	1.059	0.215	0.050	0.5
4	5 256 270	1.100	0.216	0.025	0.5

ANNEXE II

PITOT PRINCIPLE AND ERROR

A pitot-static tube, also known as a Prandtl tube, will be used to measure the nominal air velocity and to calibrate the hot wire anemometer. The working principle of the pitot tube is based on the Bernoulli equation and allows to convert the kinetic energy of the fluid in a potential energy. P_x is the static pressure, $\frac{1}{2}\rho v_x^2$ is the dynamic pressure and $\rho g h_x$ is the hydrostatic pressure [38].

$$P_1 + \frac{1}{2}\rho u_1^2 + \rho g h_1 = P_2 + \frac{1}{2}\rho u_2^2 + \rho g h_2 \qquad \text{(A II-1)}$$

The central inlet of the pitot records the total pressure (P_t) i.e., the static pressure and the dynamic pressure, while the ports on the periphery, perpendicular to the flow, record the static pressure (P_s). The schematic of a pitot-tube is represented in Figure A II-1.

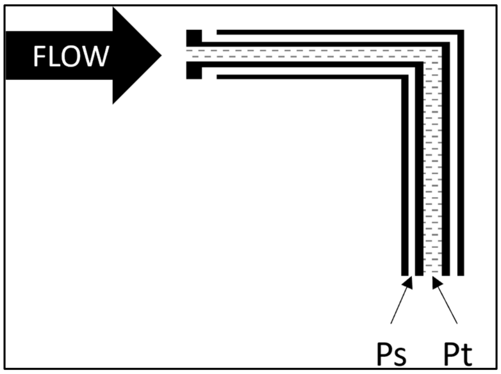

Figure A II-1 Pitot-Static Tube

In this case, there is no head difference, hence the hydrostatic pressure term can be eliminated from the equation. By measuring the pressure differential, one can calculate the velocity of the fluid using the following equation:

$$P_1 + \frac{1}{2}\rho u_1^2 = P_2 \rightarrow u_1 = \sqrt{\frac{2(P_2 - P_1)}{\rho}} \qquad \text{(A II-2)}$$

The differential pressure sensors measure this ΔP in inches of water, which must be converted to air to calculate the air speed. ρ is in kg/m^3, g is in m/s^2, h is in meter and u is in m/s.

$$\Delta P = \rho_{water} g h \rightarrow u = \sqrt{\frac{2\rho_{water} g h}{\rho_{air}}} \qquad \text{(A II-3)}$$

The pressure sensors coupled to the pitot-static tube have a full-scale accuracy of 0.25-0.30% meaning the maximum error is not proportional to the input, but relative to the maximum range. For instance, the PX653-01D5V (Omega Engineering) has a range of 0-1 in. of water and an accuracy of 0.30% FS, meaning the maximum error is 0.003'' (0.076mm) of water. Converting these values to air speed, we find the maximum velocity is 20.34 m/s and the accuracy is 1.11 m/s, which is over 5%.

$$u_{max} = \sqrt{\frac{2(1000 \times 9.81 \times 0.0254)}{1.205}} = 20.34\, m/s \qquad \text{(A II-4)}$$

$$u_{err} = \sqrt{\frac{2(1000 \times 9.81 \times 7.62E - 5)}{1.205}} = 1.11\, m/s \qquad \text{(A II-5)}$$

The following table presents the pressure differential sensors that will be used:

Table-A II-1 Differential pressure sensor specifications

Make	Model	Range (in. H2O)		Accuracy	Error		
		in. H_2O	m/s		mm H_2O	Pa	m/s
Omega Engineering	PX653-05D5V	5.00	45.5	0.30%	0.381	3.74	2.49
Omega Engineering	PX653-01D5V	1.00	20.3	0.30%	0.076	0.75	1.11
Alpha Instruments	161W0R25DB2YA	0.25	10.2	0.25%	0.016	0.16	0.51
Alpha Instruments	161W00R1DB2YA	0.10	6.4	0.25%	0.006	0.06	0.32

ANNEXE III

CVA PRINCIPLE AND CIRCUITRY

Hot wire anemometry is fundamentally simple and relies on convective heat transfer. The probe consists of a very thin wire (Ø=5µm), held between two needle-like prongs. The anemometer injects a very faint current through the probe, heating up the wire. Convective heat transfer between the wire and the air changes the resistance of the wire. When coupled to a constant voltage anemometer (CVA), this variation is converted to an output voltage which is then converted to a velocity. The calibration procedure are explained in the next sections.

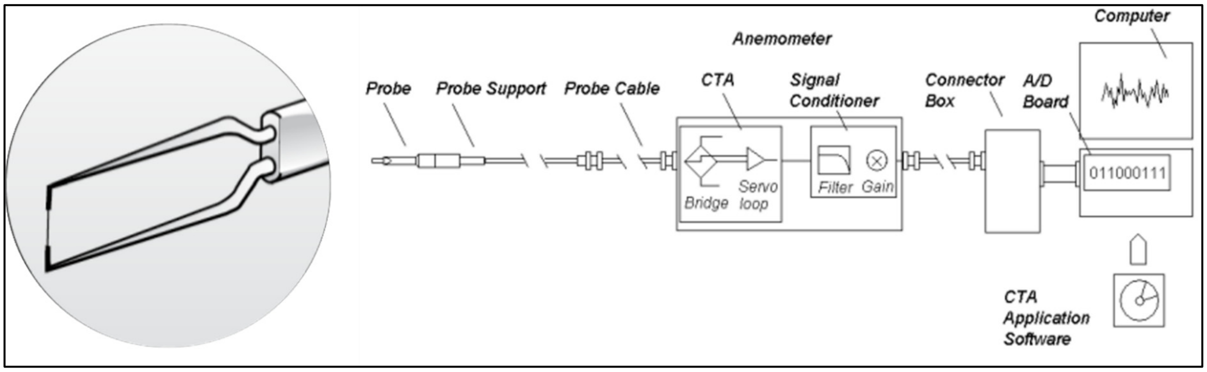

Figure A III-1 CVA Probe and Setup. Reprinted from [32] p. 6. © 2005 by Dantec Dynamics.

The CVA circuit (Figure A III-2) is essentially a feedback-loop amplifier to which the hot-wire (R_W) is connected.

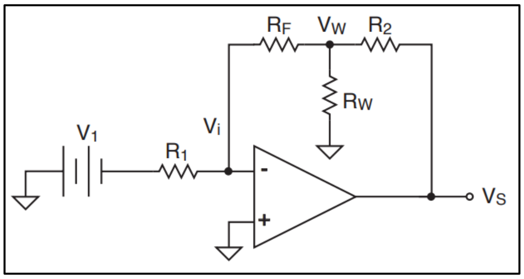

Figure A III-2 CVA Circuit, reprinted from [31], © 2005 by Tao of Systems Integration Inc.

The voltage passing through the wire (V_w) is function of two fixed resistors (R_1 & R_f) and V_1, a variable voltage source. V_1 is variable in the sense it can be manually adjusted to obtain the desired V_w, but remains fixed during operation, hence V_w remains constant.

$$V_w = \frac{R_f}{R_1} V_1 \tag{A III-1}$$

V_w affects the response of the wire, and the appropriate voltage depends on the type of measurements to be performed. The higher V_w is, the hotter the wire will operate, which leads to a greater overheat ratio (a_w). The overheat ratio is simply the relative difference in resistance of the unheated wire (at ambient temperature, R_a) and heated wire (in operation, R_w).

$$a_w = \frac{R_w - R_a}{R_a} \tag{A III-2}$$

A high overheat ratio ($0.3 < a_w < 1.0$) is more sensitive to velocity fluctuations, while a low a_w is more sensitive to temperature variations in the fluid.

Because V_w is kept constant while the CVA is recording, any change in R_w will affect the current passing through R_2. The resulting equation for V_s follows.

$$V_s = \left(1 + \frac{R_2}{R_f} + \frac{R_2}{R_w}\right) V_w \tag{A III-3}$$

Increasing the velocity of the fluid will intensify the convective heat transfer, resulting in a lower wire temperature (T_w) and a lower R_w through the Joules effect, which in turn leads to a higher V_s.

ANNEXE IV

HWA SIGNAL POST-PROCESSING

1. Import the raw data (Vs) for a given control voltage of the motor.
2. Convert the data from time-domain to spectral-domain using an FFT.
3. The spectral data is then smoothed using *sgolayfilt* to facilitate the detection of the peak.
4. The peak frequency is identified using *findpeaks*, and the velocity is calculated using the Strouhal relation, see Figure A IV-1.
5. The raw signal (Vs) is averaged.
6. A Vs-U pair is obtained.
7. The process is repeated for all the other control voltages.
8. The Vs-U relation is plotted and curve-fitted.
9. The equation is stored in memory and used to convert the Vs signal to velocity for the actual runs, see Figure A IV-2.

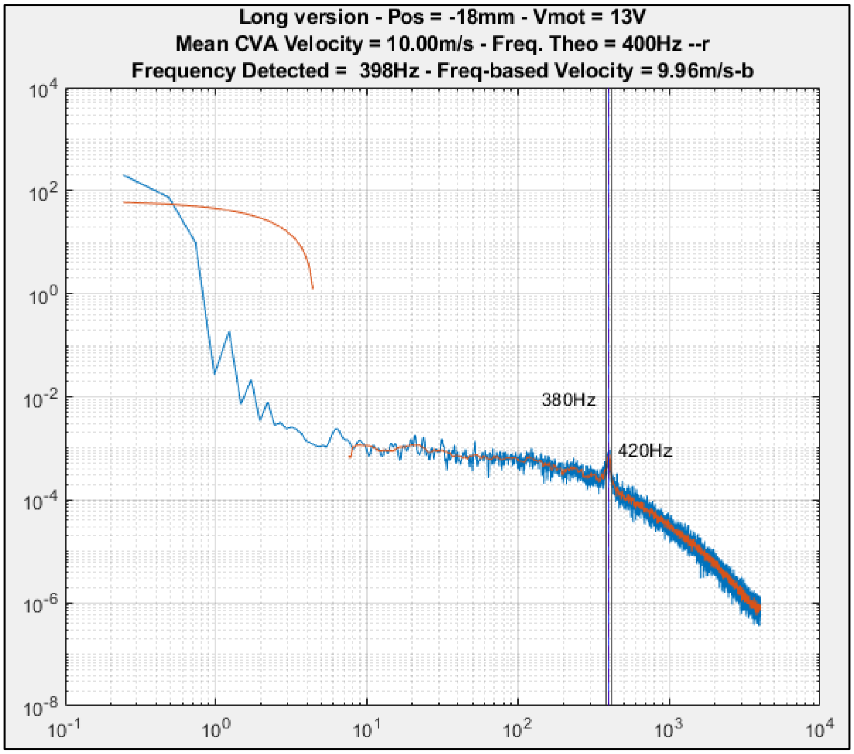

Figure A IV-1 Smoothed PSD of the CVA signal with the peak frequency identified

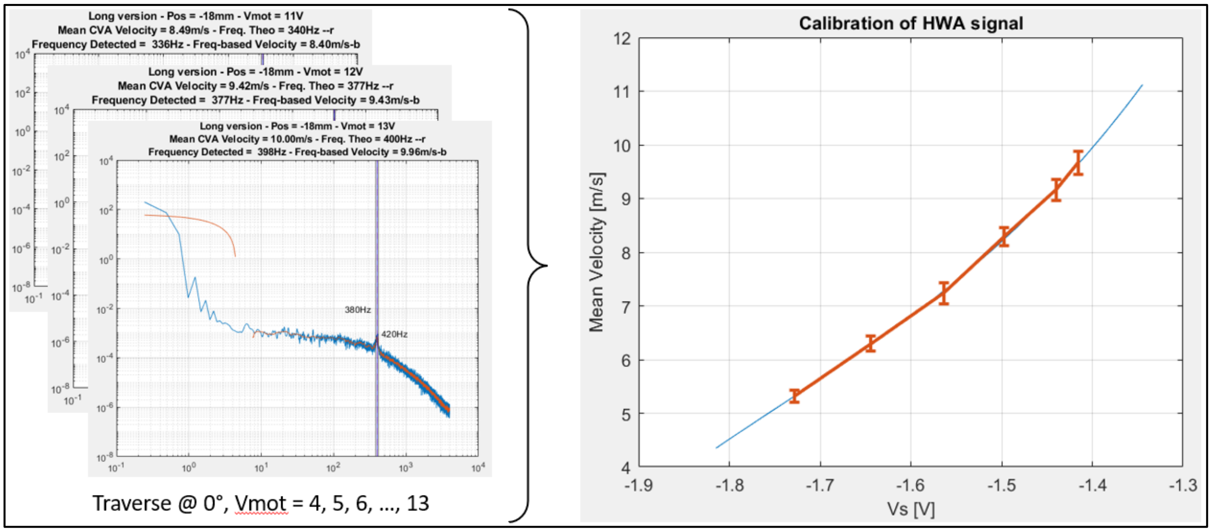

Figure A IV-2 The calibration curve is obtained from the peaks measured at the different velocities

BIBLIOGRAPHY

1. Lefebvre, A.H. and Ballal, D.R., *Gas Turbine Combustion*. 2010. 560.
2. Banhart, J., *Manufacture, characterisation and application ofcellular metals and metal foams.* Progress in Materials Science, 2001. **46**(6): p. 559-632.
3. Torrents, A.*, et al.*, *Characterization of nickel-based microlattice materials with structural hierarchy from the nanometer to the millimeter scale.* Acta Materialia, 2012. **60**(8): p. 3511-3523.
4. Xiong, J.*, et al.*, *Advanced Micro-Lattice Materials.* Advanced Engineering Materials, 2015. **17**(9): p. 1253-1264.
5. Nield, A.D. and Bejan, *Convection in Porous Media*. 2013: Springer.
6. Skjetne, E. and Auriault, J.-L., *High-velocity laminar and turbulent flow in porous media.* Transport in Porous Media, 1999. **36**: p. 131-147.
7. Guo, P., *Dependency of Tortuosity and Permeability of Porous Media on Directional Distribution of Pore Voids.* Transport in Porous Media, 2012. **95**(2): p. 285-303.
8. Bazarin, R.L.M.*, et al.*, *Boundary Effects on the Tortuosity and Permeability of Idealized Porous Media.* Transport in Porous Media, 2021. **136**(3): p. 743-764.
9. Bonnet, J.-P., Topin, F., and Tadrist, L., *Flow Laws in Metal Foams: Compressibility and Pore Size Effects.* Transport in Porous Media, 2008. **73**: p. 233-254.
10. Azzi, W., Roberts, W.L., and Rabiei, A., *A study on pressure drop and heat transfer in open cell metal foams for jet engine applications.* Materials and Design, 2005. **28**: p. 569-574.
11. Lucca-Negro, O. and O'Doherty, T., *Vortex breakdown: a review.* Progress in Energy and Combustion Science, 2001. **27**(4): p. 431-481.
12. Bearman, P.W., *Circular cylinder wakes and vortex-induced vibrations.* Journal of Fluids and Structures, 2011. **27**(5): p. 648-658.
13. Oliveira, M.A.D.*, et al.*, *Control and Suppression of Vortex Shedding from a Slightly Rough Circular Cylinder by a Discrete Vortex Method.* Energies, 2020. **13**(17): p. 4481.
14. Hrynuk, J.T., Van Luipen, J., and Bohl, D., *Flow visualization of a vortex ring interaction with porous surfaces.* Physics of Fluids, 2012. **24**(3): p. 037103.
15. Hrynuk, J.T., Stutz, C.M., and Bohl, D.G., *Experimental Measurement of Vortex Ring Screen Interaction Using Flow Visualization and Molecular Tagging Velocimetry.* Journal of Fluids Engineering, 2018. **140**(11): p. 111401.
16. Naaktgeboren, C., Krueger, P.S., and Lage, J.L., *Interaction of a laminar vortex ring with a thin permeable screen.* Journal of Fluid Mechanics, 2012. **707**: p. 260-286.
17. Musta, M.N. and Krueger, P.S., *Interaction of vortex rings with multiple permeable screens.* Physics of Fluids, 2014. **26**(11): p. 113101.
18. Musta, M.N. and Krueger, P.S., *Interaction of steady jets with an array of permeable screens.* Experiments in Fluids, 2015. **56**(3): p. 61.
19. Timercan, A., Sheremetyev, V., and Brailovski, V., *Mechanical properties and fluid permeability of gyroid and diamond lattice structures for intervertebral devices: functional requirements and comparative analysis.* Sci Technol Adv Mater, 2021. **22**(1): p. 285-300.

20. An, X., Fultz, H., and Hassanipour, F., *Experimental Study of Air Vortex Interaction with Porous Screens.* Special Topics Reviews in Porous Media: An International Journal, 2014. **5**(4): p. 297-309.
21. An, X., Jiang, L., and Hassanipour, F., *Numerical Analysis of Air Vortex Interaction with Porous Screen.* Fluids, 2021. **6**(2): p. 70.
22. Cheng, M., Lou, J., and Lim, T.T., *A numerical study of a vortex ring impacting a permeable wall.* Physics of Fluids, 2014. **26**(10): p. 103602.
23. Teruna, C.*, et al.*, *A rod-linear cascade model for emulating rotor-stator interaction noise in turbofans: A numerical study.* Aerospace Science and Technology, 2019. **90**: p. 275-288.
24. Jacob, M.C.*, et al.*, *A rod-airfoil experiment as a benchmark for broadband noise modeling.* Theoretical and Computational Fluid Dynamics, 2005. **19**(3): p. 171-196.
25. Nguyen, Q.D.*, et al.*, *A state-of-the-art review of flows past confined circular cylinders.* Physics of Fluids, 2023. **35**(7).
26. Siemens_Industries_Digital_Software. *Simceter STAR-CCM+ 2306 User Guide, in Simulating Physics/Turbulence/Wall Treatment*. Available from: https://docs.sw.siemens.com/documentation/external/PL20200805113346338/en-US/userManual/userguide/html//STARCCMP/GUID-478651F1-9901-41B6-8193-3052E3CCE9DB.html.
27. Weltens, H.*, et al.*, *Optimisation of Catalytic Converter Gas Flow Distribution by CFD Prediction*. 1993, SAE International.
28. Ong, L. and Wallace, J., *The velocity field of the turbulent very near wake of a circular cylinder.* Experiments in Fluids, 1996. **20**(6): p. 441-453.
29. ANSI/AMCA, *Standard 210-16, ASHRAE Standard 51-16, Laboratory Methods of Testing Fans for CertifiedAerodynamic Performance Rating*. 2016: USA.
30. Mohammed-Taifour, A.*, et al.*, *A detailed procedure for measuring turbulent velocity fluctuations using constant-voltage anemometry.* Experiments in Fluids, 2015. **56**(9).
31. Tao of Systems Integration, I., *Constant Voltage Anemometer - Technical Note*. 2005.
32. Jørgensen, F., E., *How to Measure Turbulence with Hot-Wire Anemometers - A Practical Guide.* 2005.
33. Sattarzadeh, S.S., Kalpakli, A., and Örlü, R., *Hot-Wire Calibration at Low Velocities: Revisiting the Vortex Shedding Method.* Advances in Mechanical Engineering, 2013. **5**: p. 241726.
34. El-Gabry, L.A., Thurman, D.R., and Poinsatte, P.E., *Procedure for Determining Turbulence Length Scales Using Hotwire Anemometry.* 2014.
35. Berlinski, J., Chmielewski, R., and Pankanin, G.L. *Vortex Flow Field Investigations with Application of Hot-Wire Anemometer.* in *IMEKO TC9 - 10th Conference on Flow Measurement*. 2000. Salvador, Bahia, BRAZIL.
36. Norberg, C., *Fluctuating lift on a circular cylinder: review and new measurements.* Journal of Fluids and Structures, 2003. **17**(1): p. 57-96.
37. Heddleson, C.F., Brown, D.L., and Cliffe, R.T. *Summary of Drag Coefficients of Various Shaped Cylinders.* 1957.
38. Tavoularis, S., *Measurement in Fluid Mechanics*. 2005: Cambridge University Press.